Mechanical Fatigue Modeling of Reinforced Membranes in Fuel Cells

by

Mohsen Mazrouei Sebdani

M.Sc., University of Tehran, 2015

B.Sc., Isfahan University of Technology, 2012

Thesis Submitted in Partial Fulfillment of the
Requirements for the Degree of
Doctor of Philosophy

in the
School of Sustainable Energy Engineering
Faculty of Applied Sciences

SIMON FRASER UNIVERSITY

Spring 2024

Declaration of Committee

Name:	**Mohsen Mazrouei Sebdani**
Degree:	**Doctor of Philosophy**
Title:	**Mechanical Fatigue Modeling of Reinforced Membranes in Fuel Cells**
Committee:	**Chair:** **Manpreet Kaur** Lecturer, Sustainable Energy Engineering
	Erik Kjeang Supervisor Professor, Mechatronic Systems Engineering
	Colin Copeland Committee Member Associate Professor, Sustainable Energy Engineering
	Nimal Rajapakse Committee Member Professor, Engineering Science
	Vahid Hosseini Examiner Associate Professor, Sustainable Energy Engineering
	Zuomin Dong External Examiner Professor, Mechanical Engineering University of Victoria

Abstract

A fuel cell system is an electrochemical device that converts chemical energy from a fuel, such as hydrogen, into electricity, water, and heat. In Polymer electrolyte fuel cells (PEFC), the membrane acts as an ion-conducting component between the anode and cathode, plays a predominant role in the fuel cell's performance and lifetime. Humidity and temperature cycling during fuel cell operation cause the membrane to expand and contract, leading to mechanical fatigue over time.

In this study, by developing a constitutive model, the mechanical fatigue responses of a reinforced membrane in varied environmental conditions have been investigated in both ex-situ and in-situ. Both ex-situ fatigue tests by dynamic mechanical analysis (DMA) and in-situ fatigue test through pressure-differential accelerated mechanical stress tests (∆P-AMST) in a fuel cell setup, have been implemented and modeled for the fatigue evaluation of the reinforced membrane. Based on the critical accumulated plastic dissipation energy (CAPDE) criterion, the membrane's fatigue lifetime estimation model for a complete fuel cell condition has been built. Projecting of fatigue lifetime from ∆P-AMST to a full fuel cell model presented a novel approach: this evaluation could be completed in less than one week as opposed to the 2-3 months required for accelerated mechanical stress tests (AMST) based on U.S. Department of Energy (DOE) protocol. This method considered all significant factors that affect the fatigue lifetime of a reinforced membrane as a viscoelastic material, such as temperature, humidity, and strain rate due to different humidity cycles. The impacts of dry phase durations in every RH cycle, the level of dryness, the types of clamping pressure, the properties of the catalyst layer (CL) and gas diffusion layer (GDL), and the ratio of the membrane's width under the channel to under the land on the membrane's fatigue lifetime have been investigated. It was learned that having shorter dry phase durations and lower levels during relative humidity (RH) cycles, using pneumatic or hydraulic pressure for clamping, and minimizing the membrane's width under the channel to below the land can increase the membrane's fatigue lifetime. Having a stronger CL or GDL does not play an effective role in the mechanical failure of the membrane. Finally, chemical degradation effects on membrane fatigue lifetime were investigated and incorporated into the fatigue lifetime estimation algorithm, considering influences on membrane thinning and plastic dissipation energy.

Keywords: Polymer Electrolyte Fuel Cell; Reinforced Membrane; Mechanical Fatigue Lifetime; Finite Element Method; Plastic Dissipation Energy; Chemical Degradation

Acknowledgements

I want to start by expressing my gratitude to my supervisor, Prof. Erik Kjeang, for providing me with this wonderful chance to undertake a doctoral degree in his research group, the Fuel Cell Research Laboratory (FCReL). I'm appreciative of his genuine support, guidance, and motivation during my PhD study.

Prof. Colin Copeland and Prof. Nimal Rajapakse, the committee advisers, deserve special thanks for the excellent advice and assistance they gave to my thesis project. I would also like to express my gratitude to AVL Fuel Cell Canada, and my industrial partners at AVL, Dr. Heather Baroody, Mr. Roger Penn, and Ms. Amy Nelson, for their financial and infrastructural support of my doctoral program, along with their precious comments that prompted me to expand the scope of my project to include more industrial considerations. It is acknowledged that funding is provided by Mitacs and AVL as well as Canada Foundation for Innovation (CFI), British Columbia Knowledge Development Fund (BCKDF) and Pacific Economic Development Canada (PacifiCan). Thank you to my colleagues at the Fuel Cell Research Lab (FCReL). To Powertech lab managers Dr. Paran Sarma and Dr. Sandeep Bhattacharya for ordering materials, providing troubleshooting help, and keeping us on schedule. Also, thank you to undergraduate co-op students Mr. Michael Chen and Mr. Jisung Jeong for keeping my experiments running smoothly.

Table of Contents

List of Tables

List of Figures

List of Acronyms

2D/3D	Two/three dimensional
AMST	Accelerated mechanical stress test
BOL	Beginning of life
CAPDE	Critical accumulated plastic dissipation energy
CCM	Catalyst coated membrane
CL	Catalyst layer
COCV	Cyclic open circuit voltage
DMA	Dynamic mechanical analyzer
DOE	United States Department of Energy
ePTFE	Expanded polytetrafluoroethylene
EW	Equivalent weight
FCEV	Fuel cell electric vehicle
FCReL	Fuel Cell Research Laboratory
FEM	Finite element method
FRR	Fluoride release rate
GDL	Gas diffusion layer
HFR	High frequency resistance
MD	Machine direction
MEA	Membrane electrode assembly
OCV	Open circuit voltage
PEM	Proton exchange membrane
PEFC	Polymer electrolyte fuel cell
PFSA	Perfluorosulfonic acid
ΔP-AMST	Pressure-differential accelerated mechanical stress test
PTFE	Polytetrafluoroethylene
RH	Relative humidity
SFU	Simon Fraser University
SOCV	Steady-state open circuit voltage (SOCV)
SOFC	Solid oxide fuel cell
TD	Transverse direction
XCT	X-ray computed tomography

1 Introduction

In this section, an overall view of fuel cell systems, different degradation mechanisms of membranes, previous studies on fatigue degradation on non-reinforced and reinforced membranes, and finally, the objectives of this study are clarified.

1.1 Polymer electrolyte fuel cell

The significant concerns related to the fast growth of global energy demand and the environmental impact of fossil fuels require prompt action. The use of fossil fuels has led to an increase in greenhouse gas emissions, causing global warming and natural disasters. The transportation sector, largely dependent on gasoline and diesel internal combustion engines, is a major contributor to this issue. In 2021, carbon dioxide emissions from the transportation industry represented 38 percent of all energy-related emissions in the US (Figure 1), the highest proportion of any economic sector [1]. Therefore, developing sustainable and eco-friendly solutions for energy use is imperative to address these problems. Efforts are currently underway to explore innovative solutions in the clean energy transportation sector, including the use of electric and hybrid vehicles, alternative fuels like hydrogen fuel cells and biofuels, and the development of more efficient engines. Additionally, attempts are being made to enhance public transportation systems and encourage active modes of transportation, such as walking and cycling.

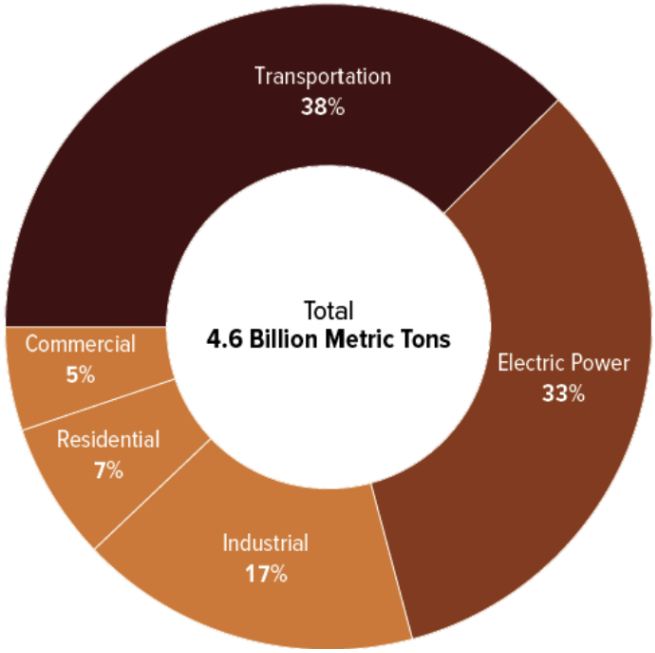

Figure 1 Carbon dioxide emissions in the USA by economic sector, 2021 [1]

Governments, industries, and individuals should work together to make the transition to cleaner means of transportation. Governments can enact laws and regulations that promote the use of renewable energy vehicles while discouraging the use of fossil fuels. Organizations can support sustainable business practices by promoting renewable energy technology research and development. People can make informed decisions, such as choosing hydrogen, electric, or hybrid vehicles or taking public transportation, especially those that are more environmentally friendly, such as hydrogen fuel cell buses.

When it comes to alternative energy for transportation, fuel cells have the potential to replace conventional engines that run on fossil fuels. They function quietly, cleanly, and efficiently, which makes them ideal for addressing the environmental issues the automotive sector faces. Since the introduction of fuel cell electric vehicle (FCEV) projects in the 1990s [2], research has advanced the technology to the point where major automakers, such as Mercedes-Benz, Honda, Toyota, Hyundai, BMW, General Motors, Ford, and Nissan are pursuing comprehensive fuel cell programs to make zero-emission vehicles accessible to the general public [3]. For heavy vehicles primarily used in freight, both battery electric vehicles (BEV) and FCEVs offer advantages over traditional diesel vehicles. BEVs have higher energy efficiency and power reversibility with Li-Ion batteries,

recovering braking energy. However, for long distances and intensive use, high-energy storage increases battery mass, reduces cargo space, and raises costs, making them more suitable for passengers and light-duty applications. FCEVs are better suited for heavy-duty vehicles due to their high specific energy density, resulting in faster refueling times and greater autonomy compared to BEVs. A hydrogen fuel cell bus takes 3-5 minutes to refuel, while an electric bus in its fast charge mode takes 3-4 hours to fully charge. Hydrogen tanks in FCEVs are lighter and take up less space than batteries, allowing for increased load transportation in trailers. Efficient, safe, and cost-effective hydrogen storage solutions remain a challenge, requiring advancements in materials' development, to optimize vehicle space and thermal management. Green, blue, and gray hydrogen are terms used to describe different methods of hydrogen production, each with varying levels of environmental impact and carbon emissions [4].

Green hydrogen is produced through a process called water electrolysis, using electricity generated from renewable energy sources such as solar, wind, or hydroelectric power. During electrolysis, water (H_2O) is split into hydrogen (H_2) and oxygen (O_2) using an electrolyzer. Since the electricity comes from clean, renewable sources, the production of green hydrogen does not release carbon dioxide (CO_2) or other greenhouse gases. Green hydrogen is considered the most environmentally friendly and sustainable method of hydrogen production, as it contributes to decarbonization efforts and reduces overall carbon emissions. Blue hydrogen is produced through the steam methane reforming (SMR) process, where natural gas (methane, CH_4) reacts with steam to produce hydrogen and carbon monoxide (CO). The CO is then reacted with water to produce additional hydrogen and carbon dioxide (CO_2). The key difference between blue and gray hydrogen is that blue hydrogen production includes a carbon capture and storage (CCS) step. Carbon capture technology is used to capture the CO_2 emissions generated during the SMR process, and this captured CO_2 is then transported and stored underground, preventing it from being released into the atmosphere. As a result, blue hydrogen production reduces the net carbon emissions associated with the process compared to gray hydrogen. Gray hydrogen is also produced through the steam methane reforming (SMR) process, similar to blue hydrogen. However, in gray hydrogen production, the CO_2 emissions generated during SMR are released into the atmosphere, making it the most carbon-intensive and environmentally unfriendly method of hydrogen production. It is called “gray” because it lacks any carbon capture or emissions reduction steps [5].

Green hydrogen production is a growing trend in the global energy sector, as more countries and companies are investing in this clean and versatile fuel. According to some estimates, green hydrogen could supply up to 25% of the world's energy needs by 2050 [6]. Governments are also supporting this technology and realizing its advantageous environmental effects by developing infrastructure and providing subsidies [7, 8].

An electrochemical device known as a fuel cell converts chemical energy into electrical energy by using participating reactants. A number of reactants and materials can be used to create fuel cells, giving them a flexible technology that can be used in a variety of applications [9]. PEFC is the leading option for use in transportation systems such as small automobiles, heavy vehicles, ships, trains, and aircrafts because of the following reasons [10]:

- High Power Density: Compared to other fuel cell types, PEFC have a higher power density, which allows them to produce more power per unit of volume and weight. They are therefore perfect for transportation applications where weight and space are important considerations.
- Rapid Start-up Time: PEFC can start up rapidly, usually in only a few seconds. This is crucial for transportation applications, including those in automobiles, where short start-up and shutdown times are required.
- High Efficiency: PEFCs are capable of converting a significant amount of the energy in the fuel into electrical energy, making them highly efficient (50-60%). As a result, fuel efficiency improves and emissions decrease.
- Low Operational Temperature: Because PEFCs operate at a low temperature (usually around 80 °C), it is possible to create fuel cell systems that are simpler and more compact than all other fuel cells in Figure 3. As a result, the warm-up period is shortened, and less energy is used.
- PEFCs are more durable than other types of fuel cells such as solid oxide fuel cells (SOFC).

PEFCs also have an advantage over batteries in terms of energy density and refueling/recharging time [10, 11]. In Figure 2, a comparison between battery electric vehicles (EV) and hydrogen fuel cell electric vehicles (FCEV) by DOE has been done that demonstrates hydrogen for heavier vehicles and more mileage outweighs battery options. For instance, in the 200-mile range, an EV has around 1.5 times the weight of an FCEV, and for 300 miles, this ratio increases to 1.9. From a volume perspective, for 200 miles, EV gets 2.8 times more volume than FCEV, and for 300 miles, it grows to 3.8. Therefore, FCEV will be more attractive for vehicles with higher mileage, like heavy vehicles.

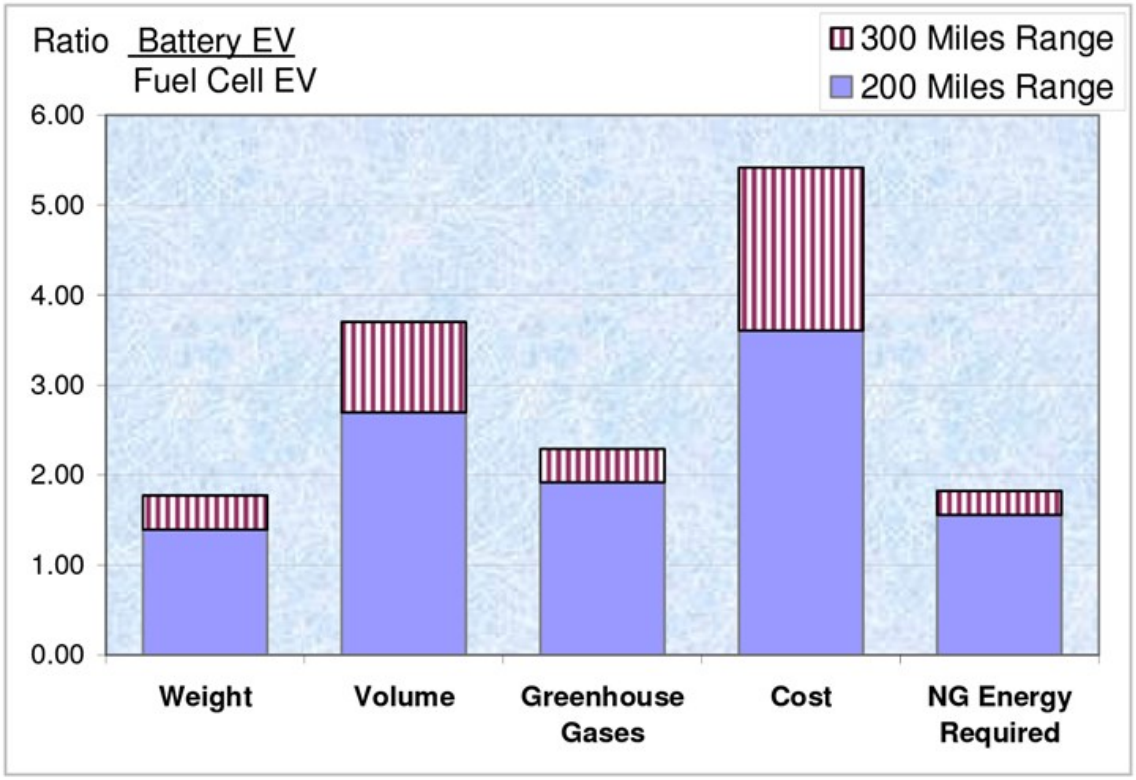

Figure 2 A comparison between Battery EV and Fuel Cell EV [11]

A comparison between several types of fuel cell systems has been displayed in Table 1 that shows the advantages and disadvantages of each type.

Table 1 A comparison between diverse types of fuel cells [9]

Fuel Cell Type	Alkaline fuel cell	Phosphoric acid fuel cell	Solid oxide fuel cell	Molten carbonate fuel cell	Polymer electrolyte fuel cell
Electrolyte Material	Solution of potassium hydroxide in water	Solution of phosphoric acid in porous silicon carbide matrix	Yttria (Y2O2) stabilized zirconia (ZrO2)	Molten alkali metal (Li/K or Li/Na) carbonates in porous matrix	Flexible solid Perfluorosulfoni-c acid polymer
Operating Temperature (C)	60–250	160–220	600–1000	600-800	30-100
Major Poison	CO_2	Sulfur, high levels of CO	Sulfur	Sulfur	CO, Sulfur, metal ions, peroxide

Advantages	High efficiency, low oxygen reduction reaction losses	1–2% CO tolerant, good-quality waste heat, demonstrated durability	CO tolerant, fuel flexible, high-quality waste heat, inexpensive catalyst	CO tolerant, fuel flexible, high-quality waste heat, inexpensive catalyst	Low temperature operation, high efficiency, high H_2 power density, relatively rapid start-up
Disadvantages	Must run on pure oxygen without CO_2 contaminant	Low power density, expensive, platinum, catalyst used, slow start-up, loss of electrolyte	Long start-up time, durability under thermal cycling, inactivity of electrolyte below ~600◦C	Electrolyte dissolves cathode catalyst, extremely long start-up time, carbon dioxide must be injected to cathode, electrolyte maintenance	Expensive catalyst, durability of components not yet sufficient, poor-quality waste heat, Intolerance to CO, thermal and water management
Most Promising Applications	Space applications with pure O_2/H_2 available	Premium stationary power	Stationary power with cogeneration, continuous-power applications	Stationary power with cogeneration, continuous power applications	Portable, automotive, and stationary applications

The hydrogen molecule splits into its proton and electron components on the anode side of PEFCs as a result of an electrochemical reaction. The protons travel to the cathode after passing through the polymer membrane electrolyte, and the electrons travel to the cathode through an external circuit. Finally, oxygen on the cathode side interacts with electrons and protons to create water [9]. In Figure 3, the fuel cell operational mechanism and stack configuration have been displayed.

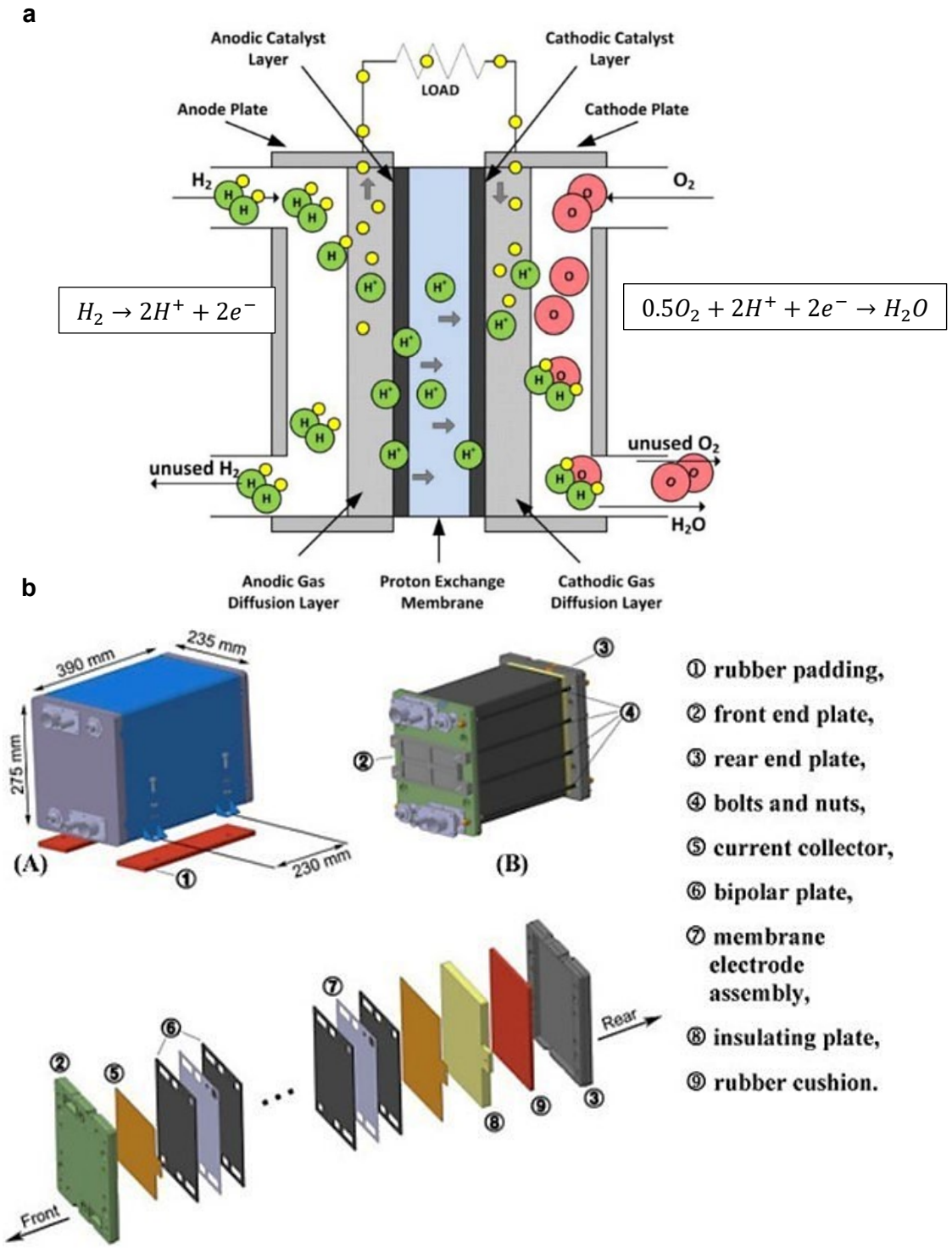

Figure 3 **a) Hydrogen oxidation reaction (HOR) and oxygen reduction reaction (ORR), the two half-cell reactions, are shown in a schematic of a proton exchange membrane fuel cell. b) PEFC stack configuration, Reprinted from Chapter 1 Proton exchange membrane fuel cells: fundamentals, advanced technologies, and practical applications with permission from Elsevier [12]**

In Figure 5-b, is a general configuration of a PEFC stack with one cell, membrane electrode assemblies (MEA) include electrodes, electrolyte, catalyst, and gas diffusion layers. Graphite plates are feeding fuels, gaskets are for sealing, current collectors are for collecting electrons from the anode side and transferring them to the cathode side, and end plates serve as integral components that facilitate gas distribution, provide sealing, offer structural support, and its bolts are for applying the clamping pressure.

In a PEFC, there are several types of clamping pressure that are used to hold the components of the cell together and ensure proper sealing and electrical contact. These include:

Mechanical compression: This is the most common type of clamping pressure used in PEFCs, and it refers to the physical force applied to the cell components by tightening the bolts or screws that hold them in place. The compression force can affect the cell's performance by altering contact resistance, cell resistance, and water management. Inadequate compression may lead to leakage and reduced performance, while excessive compression may damage the membrane or other components and cause degradation. Hydraulic pressure: Hydraulic pressure is used in some PEFC designs to apply even and controlled compression across the cell components. This is achieved by using a hydraulic press to apply pressure uniformly to the cell stack. The hydraulic pressure ensures an even and consistent clamping force across the entire stack, which can improve cell performance and reduce the likelihood of leaks or damage.

Pneumatic pressure: Pneumatic pressure, also known as air pressure, is another type of pressure used to compress the cell components. This method uses compressed air to apply a force on the stack. Pneumatic pressure is preferred in applications where hydraulic pressure is not available or feasible. The pressure is evenly applied to the stack, and a suitable torque is developed on the bolts. The disadvantage of this method is that the pressure may not be evenly distributed if the gaskets are not uniform in thickness.

In our study, the effects of clamping pressure on the membrane’s fatigue lifetime were also investigated, and for this reason, an introduction to different clamping mechanisms in fuel cell stacks was presented.

1.2 Proton exchange membrane

The proton exchange membrane (PEM) serves as both an ionic conductor and an electron isolator. Any time hydrogen leaks from the anode to the cathode side, fuel cell performance suffers, and there may be safety implications due to potentially combustive gas mixtures. Membrane degradation can therefore result in lifetime limiting failure. Consequently, new membrane generations, like reinforced membranes with more durability, are developing [13]. Even though PEFC technology has undergone major advancements recently, the longevity of PEFCs makes it difficult to guarantee the large-scale commercial viability of these systems for both transportation and stationary power applications [14] especially for heavy vehicles and therefore, more durability improvements are required. According to the U.S. Department of Energy, the ultimate life target for PEFCs in heavy-duty trucks is 30,000 hours (about 3 and a half years), equivalent to 1.2 million miles of vehicle life. This is based on the assumption that the fuel cell system will operate at temperatures above 100 °C, which can reduce the cooling requirements and improve efficiency [15]. According to the US Department of Energy (DOE) [16], the two main factors behind catalytic degradation are carbon support corrosion and Pt sintering, and for membrane degradation, mechanical fatigue and chemical degradation, which when combined can greatly decrease the operating longevity of fuel cells, especially for automotive applications that are particularly susceptible to these issues due to their regularly varying duty cycles, frequent starts and stops, and operation at various temperatures [17].

As previously mentioned, the membrane plays a crucial role in the PEFC by facilitating essential functions such as protonic conduction, electronic insulation, and gas separation between the electrodes. It also serves as support for the catalyst layers (CL). To remain functional, a proton conductivity of around 0.1 $S.cm^{-1}$ is desired, which is typically expressed in Siemens per centimeter. This level of conductivity ensures efficient proton transport within the fuel cell, enabling the desired power output. Regarding gas permeability, it refers to the ability of gases to pass through the PEM. In fuel cell applications, it is crucial to minimize the crossover of reactant gases (hydrogen and oxygen) across the membrane. This prevents fuel loss and ensures efficient cell operation that therefore, the gas permeability should be less than 10^{-12} mol H_2 $cm^{-1}s^{-1}kPa^{-1}$ and less than 10^{-11} mol O_2 $cm^{-1}s\text{-}^{1}kPa^{-1}$ [18]. In PEFCs, the membranes used are typically

polymeric-based materials. These membranes are often referred to as ionomers due to the presence of hydrophilic ionic groups within their molecular structure [19]. These ion-containing groups play a crucial role in the functionality of the material and facilitate the transport of protons (H+) across the membrane. The ionomers used in PEFC membranes are designed to have a balance of properties that are essential for efficient proton transport. They possess a hydrophilic nature, which allows them to readily absorb and retain water molecules. This water retention is important because it helps to maintain the necessary hydration level within the membrane, promoting proton conduction. The ionic groups within the membrane can be sulfonic acid ($-SO_3H$) or carboxylic acid (-COOH) moieties, which are hydrophilic and contribute to the ion conductivity of the material. These functional groups are responsible for attracting and conducting protons when the membrane is in contact with a water-based electrolyte [20]. The cross-linked molecular chains in the membrane provide mechanical stability and help maintain the membrane's structural integrity. The cross-linking prevents excessive swelling or dissolution of the membrane when exposed to water or the fuel cell environment [19].

The Perfluorosulfonic acid (PFSA) membrane with a typical thickness of 10-100 μm, such as Nafion developed by DuPont, is a copolymer composed of tetrafluoroethylene and sulfonyl fluoride vinyl ether. This membrane possesses a semi-crystalline structure [19]. One of the key factors contributing to the chemical stability of PFSA membranes is the presence of carbon-fluorine bonds, which are highly resilient and chemically inert [21]. In a fuel cell, the performance of the PFSA membrane is closely tied to its proton conductivity, which, in turn, is directly influenced by the water content [22, 23]. When Nafion is hydrated to a critical level, the ionic domains within the membrane undergo swelling, creating pathways for the conduction of protons [19]. As the water content increases, the proton conductivity of the membrane also rises until it reaches a maximum point. Beyond this optimum hydration level, further humidification leads to a decrease in conductivity due to a reduction in proton concentration [19, 23]. It is important to note that excessive humidification can potentially result in flooding of the membrane and cathode. This flooding slows down the cathode reactions and negatively impacts the overall performance of the fuel cell by blocking the pores responsible for reactant transport [22, 23]. PFSA ionomer membranes, such as Nafion, exhibit proton conductivity by dissociating $-SO_3H$ groups in the presence of water or polar solvents. This conductivity is crucial for the functioning of fuel cells. Two proton transport mechanisms are observed in

these membranes: the "proton hopping" or "Grotthus mechanism" and the "diffusion mechanism" or "vehicular mechanism" as shown in Figure 4. In the proton hopping mechanism, protons jump between hydrolyzed ionic sites across the membrane using water molecules as pathways. The diffusion mechanism involves the movement of hydrated protons through the aqueous medium due to electrochemical differences. Both mechanisms contribute to proton conductivity by allowing the transfer of protons through the membrane's polymeric chains. Controlling the water content within the membrane is essential for optimizing proton conductivity. Excessive humidification can lead to membrane flooding and reduced proton concentration, negatively affecting conductivity. Balancing the water content is crucial for achieving efficient proton conduction in PFSA ionomer membranes [24, 25].

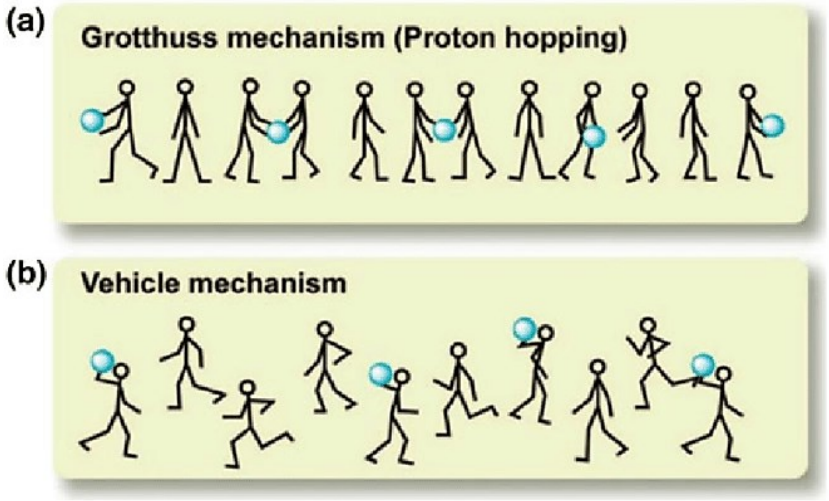

Figure 4 **Schematic representation of proton transports in membranes. a) Grotthus mechanism; the protons are passed along hydrogen bonds. b) Vehicle mechanism; the proton movement occurs with the aid of a moving "vehicle," e.g., H_2O, Reprinted with permission from [26]. Copyright 2008 American Chemical Society**

The dynamic duty cycles in potential, hydration, and temperature, as encountered in automotive applications such as acceleration, deceleration, start-up, and shutdown, can gradually damage the membrane, leading to issues such as cracks, tears, pinholes, thinning, and interfacial delamination. This damage can compromise the membrane's critical functions and even cause the fuel cell to fail [27, 28].

The degradation of the membrane in fuel cells is a multifaceted process that involves the combined action of various chemical, mechanical, and thermal factors during operation [29, 30]. The rate at which degradation occurs is typically linked to the strength of chemical, mechanical, and/or thermal stresses that act on the membrane, as well as its inherent resistance to these stresses. The presence of multiple stressors can amplify their individual impacts due to strong interactions [31].

1.2.1 Membrane degradation mechanisms

1.2.1.1 Chemical degradation

Radical chemical species that are produced within the MEA during normal fuel cell reactions are often what lead to the chemical deterioration of the membrane [27, 32-34]. As an illustration, the oxygen reduction reaction (ORR) and reactant gas crossover both have the potential to produce hydrogen peroxide (H_2O_2) as a byproduct [29]. These H_2O_2 molecules can permeate the membrane's thickness, where they can break down into dangerous radicals such as hydroxyl (HO•), hydroperoxyl (HOO•), and hydrogen (H•) radicals. The molecular structure of the PFSA ionomer is attacked and weakened by these radicals, which causes a gradual loss of membrane substance and diminished toughness [32, 35, 36]. The use of cationic transition-metal oxide scavengers, crosslinking treatment, and fluorination of susceptible spots are a few techniques used to increase the membrane's chemical stability against radical attack. Cationic transition-metal oxide scavengers, like manganese and cerium oxide, are added to fuel cell membranes to mitigate chemical degradation by neutralizing harmful radicals generated during operation. These scavengers work by capturing and deactivating hydroxyl, hydroperoxyl, and hydrogen radicals that attack and weaken the membrane's molecular structure, leading to material loss and reduced toughness. However, these scavengers may migrate and diffuse during operations, resulting in local areas that are still vulnerable to radical attack [37, 38]. Crosslinking treatment is another strategy that can reduce chemical

degradation and improve the chemical stability of fuel cell membranes. This treatment uses chemical agents to link the molecular chains of the polymer electrolyte membrane together, forming a more stable network structure. Crosslinking treatment can also decrease the permeability of the membrane to fuel and oxidant gases, which helps prevent the formation of harmful radicals within the membrane. Fluorination of vulnerable spots, such as carbon-hydrogen (C-H) end-groups, in the PFSA ionomer that makes up the membrane is another technique used to improve the chemical stability of fuel cell membranes. This process involves adding fluorine atoms to the ionomer, which strengthens the chemical bonds and makes it more resistant to attack by harmful radicals like hydroxyl, hydroperoxyl, and hydrogen radicals. This approach can reduce the loss of membrane material and increase susceptibility to fracture, leading to a longer service life for the membrane [39-41].

Open-circuit voltage (OCV) tests in fuel cells are conducted to evaluate the chemical degradation of the cell components. The OCV test involves measuring the voltage across the fuel cell terminals when they are not connected to any external load or circuit. It provides insight into the electrochemical behavior and overall health of the cell. When the fuel cell is in the OCV state, the reactant gases reach their maximum partial pressures, leading to an increased rate of crossover and membrane deterioration [42, 43]. Since no fuel and oxidant are being consumed electrochemically during the OCV test, there is a higher potential for crossover, resulting in elevated levels of peroxide formation and radical attack [44]. Hydrogen peroxide can be generated either through incomplete reduction of oxygen at the cathode under normal operating conditions or by the reduction of hydrogen and oxygen when significant gas crossover occurs at the anode catalyst/membrane interface [45]. During the OCV degradation, specific changes are typically observed, including substantial ionomer loss, significant release of fluoride ions, and a uniform reduction in the membrane thickness [45]. Typically, a solid-state polymeric membrane is used as an electrolyte to separate the electrodes, with perfluorosulfonic acid (PFSA) ionomer membranes being the most popular due to their desirable properties [46]. In the case of PFSA membranes, the release of fluoride ions serves as an indicator of membrane degradation, signifying a decline in membrane lifespan [44].

Fenton’s reagent test offers an ex-situ approach to investigate chemical degradation stressors in fuel cells. The test has been shown to yield similar reaction products compared to in-situ degradation analyses and can provide insights into the

decomposition of ionomers and potential surface damage to the membrane. This test involves the use of Fenton's reagent, which can generate hydroxyl and hydroperoxyl radicals through the decomposition of hydrogen peroxide in the presence of Fe^{2+} ions, resulting in the oxidation of Fe^{2+} to Fe^{3+} [19, 45]. Even trace amounts of transition metal ion contaminants, particularly iron cations, present in the MEA, are sufficient to activate the Fenton reactions [47]. The effectiveness of Fenton's reagent tests in simulating fuel cell chemical degradation has been demonstrated by Healy et al. [48]. They conducted in-situ and ex-situ degradation analyses and found similar reaction products using nuclear magnetic resonance (NMR) and mass spectrometry techniques [48]. Kinumoto et al. [49] also revealed that the decomposition rates of the main and side chains of the ionomer by Fe^{2+} and Cu^{2+} ions are equal in the presence of H_2O_2. Tang et al. [50], through Fourier transform infrared spectroscopy (FTIR) and NMR analysis, observed the initiation of ionomer decomposition from the end of the main chain when Nafion was subjected to a solution of H_2O_2 and metallic cations (Fe, Ni, and Cr). Additionally, SEM micrographs of Fenton-treated membranes showed the formation of small bubbles on the membrane surface, which could potentially lead to the formation of pinholes in later stages of degradation [50].

Several qualitative and quantitative characterization methods are employed to assess the rate of chemical degradation in PEFCs. Here are some of the commonly used methods [18, 31]:

Hydrogen crossover rate: This method measures the rate at which hydrogen crosses over from the anode to the cathode. By applying an external voltage to the cell while exposing the cathode to nitrogen, the crossover hydrogen oxidizes, generating a current that is directly proportional to the hydrogen crossover rate. Factors such as the hydrogen partial pressure, temperature, membrane thickness, and permeability affect the crossover rate. The membrane's permeability for oxygen can also be quantified using a similar approach.

Fluoride release rate (FRR): For fluorinated membranes, the rate of chemical degradation can be determined by analyzing the release rate of fluoride ions into the product water. FRR can be continuously monitored using fluoride ion selective electrodes.

Open circuit voltage: OCV measurement can provide information on reactant crossover, but it is not as quantitative as the hydrogen crossover method. However, OCV results can be correlated with FRR measurements. A stable OCV and minimal FRR indicate a sound membrane, while a membrane nearing failure will exhibit a reduction in OCV from 1 V to around 0.7 V.

High frequency resistance (HFR): HFR characterizes deviations in the membrane's resistance due to degradation using in-situ impedance spectroscopy. Chemical degradation causes membrane thinning, resulting in lower resistance. However, the decline in proton conductivity may counterbalance this effect. Hence, the reliability of HFR as a diagnostic tool for membrane failure is limited.

Microstructural analysis: Ex-situ microscopic analysis, particularly scanning electron microscopy (SEM), is commonly used to detect microscopic damage such as cracks, pinholes, delamination, and membrane thinning that occur during operation. Modern SEMs equipped with energy-dispersive X-ray spectroscopy (EDS) enable chemical analysis, providing information on the presence of contaminants in the membrane. For in-situ microscopic analysis, 3D X-ray Computed Tomography (XCT) can be used to monitor the membrane’s changes due to chemical degradation, like thinning and pinholes. XCT is utilized to study how the membrane structure changes over time when subjected to both chemical and mechanical stressors, enabling investigation into the combined effects of degradation on the membrane [51]. These characterization methods provide valuable insights into the chemical degradation processes occurring within PEFC membranes, helping to evaluate their overall performance and degradation rates. In the following paragraph, the chemical degradation results from OCV and FRR tests on the membrane have been elaborated on more.

As a summary of the chemical degradation process that was previously mentioned, the production of radical chemical species in MEA during normal fuel cell reactions is a common cause of chemical deterioration of the membrane. The oxygen reduction reaction and reactant gas crossover can both produce hydrogen peroxide as a byproduct, which can permeate the membrane and break down into harmful radicals. These radicals attack and weaken the molecular structure of the PFSA ionomer, causing a gradual loss of membrane substance and reduced toughness [32, 35, 36]. Kundu et al. found empirical correlations between the FRR and the production of hydrogen peroxide [52]. In a fuel cell,

the FRR is the total amount of fluoride ions that move outward from the cell and into the gas channels. This measurement is used to quantify the extent of chemical degradation, as it indicates the cumulative amount of fluoride that has been released from the polymer during the operation of the fuel cell. To account for the combined effects of chemical and mechanical degradation on a membrane, the membrane's modulus and thickness are determined as a function of the FRR. Empirical correlations between FRR and the degraded membrane's Young's modulus (E) were established through ex-situ measurements based on experimental data [53] but based on [34], the changes in Young's modulus due to chemical degradation can be negligible because the slope of the stress-strain graph remains roughly constant. Ref [54] established an empirical correlation between the total FRR and membrane thickness based on experimental data in OCV tests. As the chemical degradation level increases, the material shifts from a ductile to a brittle state during fracture. They discovered that the reduction in crack propagation resistance was due to a decrease in the size of the plastic zone ahead of the crack tip, which led to a decline in plastic energy dissipation [54].

1.2.1.2 Thermal degradation

The PFSA membranes are susceptible to thermal degradation mechanisms such as H_2O loss, sulfonate degradation, side chain oxidation, and main chain decomposition, but these mechanisms become effective only at temperatures greater than 100 °C [46]. Since low-temperature PEFCs that use these membranes are typically operated at lower temperatures, direct thermal degradation mechanisms are usually absent except for localized hot spots [55, 56]. However, thermal effects indirectly contribute to membrane degradation due to the strong thermal dependency of in situ chemical and mechanical stressors as well as membrane properties. Thermal degradation may also occur due to temperature and freeze/thaw cycling, which can be prevented by incorporating air/liquid cooling accessories for better temperature control and post-operation inert gas purging to avoid ice formation [28, 55, 57, 58].

1.2.1.3 Mechanical degradation

Mechanical degradation of fuel cell membranes can occur due to mechanical stresses and deformations induced during fuel cell assembly and operation, as well as interactions with other components. The PFSA membrane is particularly susceptible to dimensional changes due to its high-water uptake, which can result in cyclic mechanical

stresses (hydration/dehydration) within the membrane because it is constrained within the assembled cell [59, 60]. These stresses can lead to the initiation and propagation of microcracks, which can ultimately result in membrane failure [50, 60-62]. Other mechanical damage, such as buckling or tearing, can also occur due to irregular morphologies of adjoining components or non-uniform mechanical stresses [63-65]. Through-thickness defects can create new pathways for reactant gas crossover, leading to accelerated membrane degradation. Increasing membrane thickness or equivalent weight can improve mechanical durability, but at the cost of decreased fuel cell performance [66]. The use of composite membranes containing a reinforcement layer, such as expanded Polytetrafluoroethylene (ePTFE), is an effective strategy for mitigating mechanical degradation and increasing membrane durability and lifetime [46]. Mechanical stress and deformation of the membrane is due to the following conditions [67]:

Chemical Membrane Degradation: When the membrane undergoes chemical degradation, its mechanical properties are altered. This makes it more susceptible to variations in temperature, humidity, and pressure. If the molecular weight of the high molecular weight glassy regions of the membrane is significantly lowered due to chemical degradation, the material becomes brittle and less tough. Small deformations can lead to local ruptures, while large-scale deformations cause chain slippage.

Localized Physical Stress: Stress caused by particles, non-uniform conditions within the cell, and clamping stress can lead to the formation and enlargement of cracks in the membrane. These cracks can increase gas crossover rates, contributing to chemical membrane degradation. The reaction and non-reaction zones of the membrane may expand to different extents.

Swelling and Shrinking: During membrane operation, swelling and shrinking can cause permanent plastic deformation, especially at high humidity levels. Under OCV conditions, stresses are large but uniformly distributed through the membrane. Under current load, due to electroosmotic drag, the water content at the anode side of the membrane is lower, resulting in more localized plastic strains and stresses at the cathode side.

Humidity Level: The humidity level of the membrane significantly affects the modulus and yield stress of the ionomer. Reduction in the modulus and failure strain can

lead to cracks, perforation, and membrane rupture. Hygrothermal cycling, which involves periodic changes in humidity and temperature, particularly during start-up procedures, can influence the membrane's strain-to-failure. Cycling at higher humidification levels, higher humidification cycle amplitude, and additional mechanical load caused by vibrations can accelerate membrane degradation.

High Operating Temperatures: High operating temperatures and thermal cycling of a humidified membrane without freezing are not expected to cause significant membrane damage. However, it is worth noting that the lower glass transition temperature of the perfluorosulfonic acid (PFSA) ionomer, caused by the mobility of the main chain in the polymer matrix, is in the range of 120-140 °C and therefore beyond the application limits. The actual operating temperature of a PEFC with a PFSA membrane is 30-100 °C. Some of the common forms of mechanical degradation in the membrane include [68, 69]:

Material fatigue: The repeated expansion and contraction of the membrane due to changes in temperature and humidity can cause cracks and tears in the membrane over time.

Creep: The permanent deformation of the membrane due to prolonged exposure to high temperature and pressure can cause thinning and weakening of the membrane.

Wrinkles: The uneven shrinkage or expansion of the membrane due to thermal cycling or gas crossover can cause wrinkles or folds in the membrane, which can reduce the effective contact area with the electrodes and increase the electrical resistance.

Delamination: The separation of the membrane from the CL or the gas diffusion layer due to mechanical stress or chemical attack can cause gas leakage and performance loss.

Pinholes or cracks: The formation of small holes or cracks in the membrane due to mechanical stress, chemical attack, or catalyst degradation can cause gas crossover, short circuit, and flooding.

Mechanical degradation can be mitigated by using various strategies, such as [68, 69]:

Improving the membrane material: The use of more durable and resistant materials, such as reinforced membranes, composite membranes, or alternative polymers, can enhance the mechanical stability and longevity of the membrane.

Optimizing the operating conditions: The control of temperature, humidity, pressure, and gas flow can reduce the mechanical stress and thermal cycling on the membrane and prevent extreme conditions that can damage the membrane.

Designing the fuel cell system: The use of appropriate components, such as gaskets, seals, clamps, and flow channels, can ensure uniform distribution of stress and temperature on the membrane and prevent local hot spots or deformation.

To increase the membrane's durability, reinforced membranes with three layers have been introduced. Most reinforced membranes are comprised of two PFSA layers and one microporous ePTFE core layer as shown in Figure 5, while non-reinforced membranes just have PFSA [70].

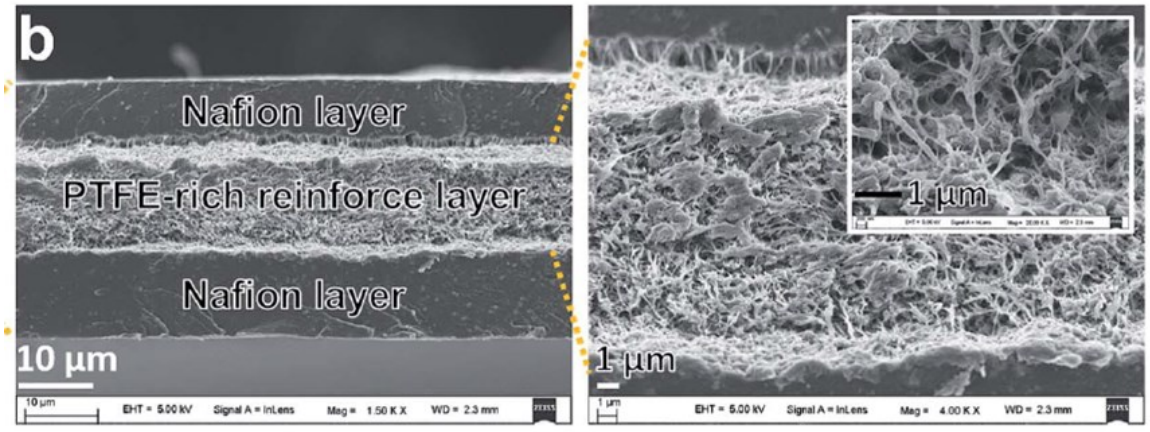

Figure 5 The microstructure of a reinforced membrane, Reprinted from [70] with permission from Elsevier

In addition to the longer lifetime provided by adding ePTFE to the membrane, reinforced membranes are thinner and, as a result, more conductive [70]. In Figure 6, The mechanical properties of Nafion 212 as a common non-reinforced membrane and Nafion XL as a commercialized reinforced membrane in a PEFC at a strain rate of 0.001 s^{-1} have been compared. Nafion XL membranes outperform Nafion 212 membranes, irrespective of their orientation. The Nafion XL membrane in the machine direction exhibits the highest Young's modulus, yield stress, and strain-hardening modulus, nearly twice as large as

Nafion 212. The anisotropic nature of Nafion XL membranes, induced by the orientation of the ePTFE reinforcement layer, explains the differences in their stress-strain behaviors. These findings make Nafion XL membranes, especially in the machine direction, more attractive for applications that demand higher mechanical strength and stiffness in PEFCs. From fatigue behavior, as stress intensity increases, the fatigue crack growth rate follows a complex pattern. Reinforced Nafion XL membrane shows a stable fatigue crack growth rate, dependent on initial crack length and orientation. Microstructure analysis reveals crack advancement and delamination at the ionomer-reinforcement layer interface. Fibers in the reinforcement layer act as bridges, transferring stress, and reducing fatigue crack propagation rate, improving membrane durability *[66]*. Most non-reinforced membranes and reinforced membranes have around 40% difference in their mechanical properties in the machine and transverse directions (MD, TD) [71] as shown in Figure 6 while in this research, the reinforced membrane shows in-plane isotropic behaviors in tensile stress tests.

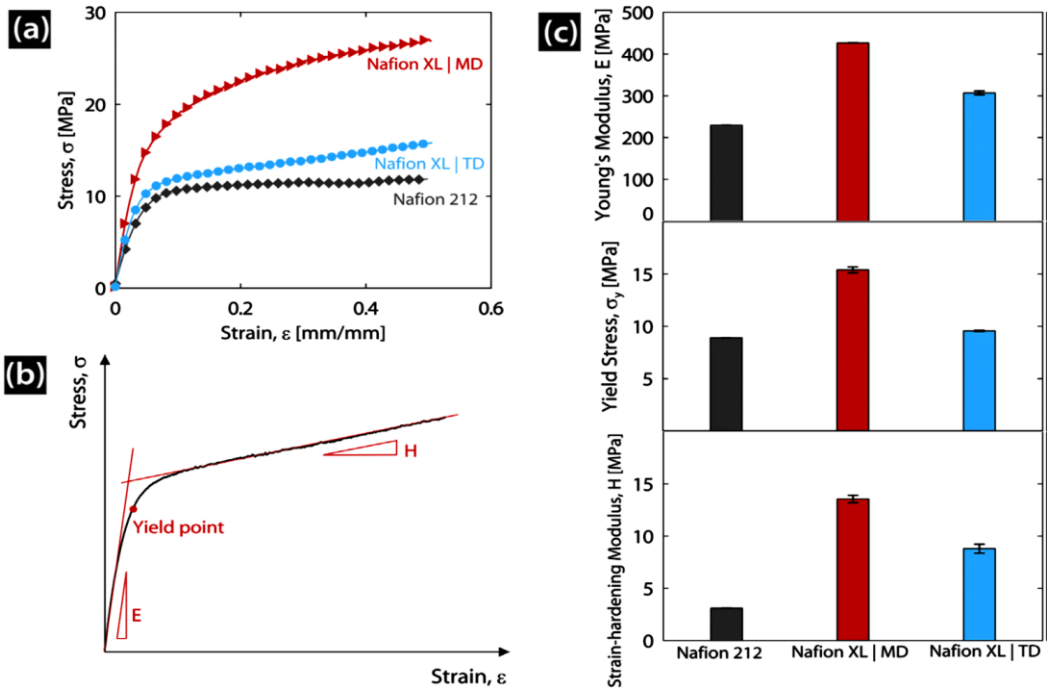

Figure 6 **Mechanical properties of a non-reinforced membrane (Nafion 212) and a reinforced membrane (Nafion XL) in two main directions, Reprinted from [66] with permission from Elsevier**

The first commercial reinforced membrane technology was unveiled by DuPont as Nafion XL MEA for PEFC at the Hannover Messe trade fair in Germany [72]. A

comparison of this reinforced membrane with two other non-reinforced membranes is presented in Table 2.

Table 2 Physicochemical and transport properties of a reinforced membrane (Nafion XL) and two types of non-reinforced membranes, Reprinted from [73] under the Creative Commons Attribution-NonCommercial 3.0 Unported Licence from Royal Society of Chemistry.

Nafion	Thickness (dry, μm)	Thickness (wet, μm)	Swelling ratio (though-plane, %)	Swelling ratio (in-plane, %)	Area resistance (Ω cm^2)	VO^{2+} permeability (10^{-7} cm^2 min^{-1})
XL	30	40	33.3	6.0	0.30	1.1
212	52	61	17.3	17.0	0.39	5.7
115	125	150	20.0	18.0	0.52	10.9

Because the in-plane swelling ratio of reinforced membranes is much lower than that of non-reinforced membranes, most researchers neglect the effects of humidity and only consider temperature impacts on reinforced membranes' modelling [73].

Numerous experiments have been conducted to determine the characteristics of reinforced membranes. However, there have only been a few attempts to model these membrane categories. The literature review suggests that recommended modeling techniques for non-reinforced membranes could inspire innovative ideas. Burlatsky et al. [74] proposed a mathematical model for predicting the GORE-SELECT (non-reinforced) membrane's life in PEFC as a function of RH cycling amplitude and membrane mechanical properties. They employed a non-linear extension of the Eyring method to predict stress relaxation in a constrained, reinforced membrane polymer. Although the water content in the membrane and RH of input fuels have a non-linear dependency, they assumed a linear correlation between the membrane's swelling and water content. For modeling, they considered that the polymer viscoelastic deformation is transferred from polymer chains to entanglements, and the slippage of the chain through entanglements generates the polymer's irreversible elongation. The Eyring model has been extended in Burlastsky's study to account for stress relaxation in a stretched-constrained polymer under any time-dependent deformation. In this model, polymer chains are the same as elastic springs, and entanglements are like visco-elastic dampers. For their damage accrual model, the elongation as stress and number of cycles in DMA were measured and used to extract some model parameters. Hasan and colleagues [75] conducted a study where they used the critical plastically dissipated energy (C-PDE) as a criterion for analyzing fatigue crack growth while considering environmental factors. The results showed that, like other

properties of Nafion NRE 211, the C-PDE is affected by temperature and humidity. Specifically, it decreases as temperature increases, while its relationship with humidity is non-monotonic. Khorasany et al. [76] developed a fatigue lifetime prediction model for nonreinforced membranes based on the elastic-plastic constitutive method and Smith-Watson-Topper (SWT) fatigue equilibrium. In their work, for strains below the yield point, the linear elasticity by Hooke's law was considered, and the visco-elastic and visco-plastic behaviors of the membrane were neglected, but for every temperature and humidity, the dependent Young's modulus and Poisson's ratio were obtained from prior experiments, and for the plastic yield response, the von Mises yield criterion was selected. Mehrtash [77] employed linear deformation to investigate the behavior of a non-reinforced membrane under hygro-thermal loading. In addition, it was assumed that both hygral and thermal strains were linearly proportional to changes in water concentration and temperature. Mehrtash established a correlation between hygral strain and membrane water content using a polynomial equation that was fitted to swelling data at a temperature of 65 °C. Silberstein et al. [78] developed two models to describe the behavior of a material under different loading conditions. The first model, Model I, accounts for both intermolecular and network mechanisms that operate in parallel during monotonic loading. The second model, Model II, was developed to address cyclic loading conditions, and includes an additional back-stress component in the intermolecular mechanism. Khattra and colleagues [79] investigated the impact of time-dependent material properties on the mechanical response of a PFSA membrane undergoing humidity cycles. They developed a constitutive model that includes an independent elastic-plastic response, as well as a time-dependent elastic-viscous response that is influenced by changes in temperature and humidity, based on isotropic hardening. The swelling strains caused by water absorption were determined using an empirical relationship developed by Kusoglu [80]. The Notron-Hoff stress-strain rate law was used to model the behavior of the dashpot element. Kusoglu's work utilized a linear Hooke's law, followed by a plastic response, while Young's modulus was found to be a function of temperature and water content in the non-reinforced membrane. Singh [81] employed a two-parallel network to model a non-reinforced membrane and used the Paris law along with the J-integral to predict crack propagation in a pre-existing crack in the model. Ding [82] simulated crack propagation through the thickness of a membrane by computing the accumulation of plastically dissipated energy ahead of the crack tip under cyclical RH loading. In Theiler's research [83], deformation energy, estimated from the modified Eyring equation, was used as a

criterion for the mechanical failure of a non-reinforced membrane. The study revealed that the amplitude of humidity variation in the cycle, cycle duration, and temperature can all affect the membrane's lifespan.

Microcracks are forming and spreading as a result of the dynamic stresses imposed by temperature and humidity fluctuations. Any variation in temperature and relative humidity can result in thermal and swelling strains in the membrane, which result in residual stress since the membrane is constrained by the other components of the MEA [84, 85]. As a result, it is preferred that the majority of active studies evaluate the mechanical fatigue lifetime of a reinforced membrane in a full fuel cell in in-situ settings from both an experimental and a modeling perspective. Under different temperature and hydration conditions, a fuel cell membrane in a vehicle might not fail for thousands of hours.

In order to assess the mechanical fatigue characteristics of membranes used in PEFCs, the US Department of Energy (DOE) has established an accelerated stress testing (AST) protocol [16]. The membranes need to undergo 20,000 cycles at a temperature of 80 °C while being exposed to 2 minutes of relative humidity at 150%, followed by 2 minutes of relative humidity at 0%. This evaluation process helps determine the ability of the membranes to withstand the mechanical stresses associated with the operation of PEFCs; however, many modern membranes, especially reinforced membranes, have successfully endured 20,000 cycles of relative humidity cycling [27, 86]. For instance, Ramani's study [87] aims to use X-ray computed tomography to determine how morphological damage develops in a reinforced membrane by pure mechanical degradation because of wet/dry cycling in a fuel cell. Although they intentionally introduced pre-defects on the CLs in their accelerated tests, which included supersaturated wet phases (150% RH) and subsequent dry phases (0% RH), both at 80 °C cell temperature, and the pre-existing cracks completely propagated in the thickness of the membrane after 4500 cycles, every fatigue test has lasted longer than 300 hours (about 2 weeks). Because of this, if reinforced membranes do not already contain flaws like cracks, doing in-situ mechanical fatigue tests on them takes much longer. When [28, 88] investigated the longer RH cycles, which showed fewer passing cycles, they found that a longer time-to-failure, or dry phase time in every cycle, has been linked to more serious mechanical damage. Mukundan et al. [27] used shorter RH cycles and observed more cycles passing without failure. These studies demonstrate an indirect correlation between a membrane's

dry phase duration throughout each humidity cycle and its mechanical fatigue lifetime. In an investigation into how cell hardware affects the outcomes of RH cycling, Chen and his coworker [89] found that all three RH cycles and the findings from the two test cells confirmed the notion that the length of each RH cycle's dry phase and the final fatigue lifetime are related.

J.R. Rice proposed plastic dissipation energy as a criterion for fatigue fracture formation in 1967 [90]. According to this idea, numerous studies [75, 82, 91-93] have used the plastic energy criterion to predict the initiation of fatigue cracks in metals and polymers. Several of these experiments assessed total plastic energy rather than dissipated plastic energy. There are two types of total plastic energy that a system absorbs in response to mechanical stress from the outside world: hysteretic and non-hysteretic. In contrast to non-hysteretic plastic energy, which is stored in the material's microstructure and can be recovered through additional deformation, hysteretic plastic energy, which accounts for nearly 90% of the total plastic energy in metals, is dissipated during deformation [94, 95]. According to [75], a model for the growth of fatigue cracks in a PFSA membrane under various ex-situ environmental conditions relevant to PEFC operations has been established. In this study, the critical plastically dissipated energy (C-PDE) for a variety of environmental conditions was derived numerically and used to estimate the crack growth rate for any fatigue loading under those conditions. This was done using experimental data [81] on ex-situ fatigue crack growth rates. The findings of the research [28, 87-89] suggest that reinforced membranes in mechanical ASTs, despite CL cracks developing early, do not exhibit significant H_2 crossing or visible fractures for the majority (80–90%) of their longevity. This indicates the time needed for crack initiation contributes to most of the fatigue lifetime of a reinforced membrane, which may be used to rate the severity of various mechanical ASTs. Hasan et al. used total plastic energy as a criterion of crack initiation of a reinforced membrane at one temperature but in three different humidity cycles in their finite element method (FEM) simulation. While their model has been calibrated using one of the experimental datasets in [96], their method can handle varied RH cycles with varying dry phase durations. In their simulations, they assumed that the majority of the total plastic energy is its hysteretic energy component, which will dissipate, and that the effects of the total plastic energy's non-hysteretic part, which has no impact on crack initiation, have been neglected.

In another experimental study, a pressure difference between the membrane's cathode and anode sides was used to accelerate AST. The duration of the entire test was reduced to less than two weeks due to the membrane's significant residual stress [97].

1.3 Coupling Chemical and Mechanical degradations

The couplings between chemical and mechanical degradation in the membrane of a PEFC is significant [98, 99] and can lead to accelerated degradation of the cell. These couplings are complex and can manifest in numerous ways.

Chemical-induced mechanical degradation: Chemical degradation weakens the polymer membrane by causing chain scission, cross-linking, and other chemical changes [98]. For instance, oxidation reactions can produce free radicals and reactive species that attack the polymer chains, reducing the membrane's mechanical integrity. As a result, the membrane becomes less flexible and more brittle [100], making it more susceptible to mechanical stresses and strains during fuel cell operation. This increased brittleness can lead to mechanical damage under operating conditions.

Mechanical-induced chemical degradation: Mechanical stresses and strains experienced by the fuel cell components, including the membrane, can create localized regions of high stress concentration. In these stress-concentrated regions, the polymer membrane may become more permeable to aggressive chemical species [98]. This facilitated diffusion of chemical species into the membrane can initiate or accelerate chemical degradation reactions, such as oxidative attack. Furthermore, cracks or defects formed due to mechanical stresses can act as preferential pathways for chemical species to penetrate deeper into the membrane, exacerbating chemical degradation mechanisms [98, 99].

Chen and his coworkers [101] used small-scale fuel cell testing and micro XCT visualization to perform 4D in situ membrane degradation analysis of the mechanisms and root causes of combined chemical and mechanical membrane degradation. The test was composed of steady state OCV held to generate chemical stress and RH cycling between wet and dry states to produce mechanical stress. Membrane cracks were the dominant failure mode in the channel region while membrane creep was the main deformation observed in the land region. Most membrane cracks were driven by membrane buckling

during RH cycling when membrane underwent cyclic swelling and shrinking. Lim at.al [33] evaluated the in-situ degradation of PFSA membranes using a cyclic open circuit voltage (COCV) accelerated stress test (AST) protocol. The degradation process involved a chemical phase and a mechanical RH cycling phase. Initially, the membrane showed a mild decay rate, but later, it experienced an increased decay rate leading to failure. Fluoride emission rate (FER) from anode and cathode effluents also increased as a function of OCV operation time. Analysis of degraded membrane samples revealed reductions in fluoride content in both side chain and main chain regions. SEM morphological analysis showed that the membrane thinned uniformly and developed pinholes, leading to hydrogen crossover leaks and ultimate failure. Tensile tests on degraded membranes indicated decreased fracture strain and increased elastic modulus, suggesting a stiffer and more brittle structure vulnerable to pinhole initiation. They demonstrated that the combination of chemical and mechanical degradation mechanisms significantly accelerated the overall rate of degradation in the PFSA membranes. In [102], Lim et al. developed a model to simulate pinhole growth by a coupled chemo-mechanical constitutive approach. To measure the distribution of pinholes, the study followed two steps: (i) defining an initial pinhole density based on the amount of fluorine released in Fenton test and (ii) considering pinhole growth under cyclic loading. Pinholes provide a pathway for reactant gas crossover, which is an indicator of membrane failure and is used to assess the membrane's life span and durability. In Alavijeh's study [34, 99], they investigated the decay in mechanical properties of catalyst coated PFSA membranes, simulating regular duty cycle fuel cell operation by employing the COCV AST protocol, which applies elevated chemical and mechanical stressors. Tensile tests demonstrated a mild increase in elastic modulus but dramatic reductions in final strain and ultimate tensile strength during degradation, indicating a transformation from a soft and ductile material to a stiff and brittle one with local variations in properties. Fracture toughness decay was observed early in degradation, likely due to locally elevated chemical degradation leading to potential fracture initiation sites. The chemical-induced brittleness reduced membrane resistance against crack propagation caused by mechanical degradation during wet/dry cycles.

1.4 Motivation and objectives

The above-mentioned literature review is mostly focused on the non-reinforced membrane from various aspects, but mostly in ex-situ conditions, while the research on reinforced membranes is not comprehensive. In addition, some of the studies on reinforced membranes used older generations of reinforced membranes, which are anisotropic in plane, while new reinforced membranes are thinner and isotropic in plane. In the nearest studies [71], the mechanical response of a reinforced membrane material without its fatigue effects has been studied, and in [70], the pressure-differential method for fatigue assessment has been considered but only at one temperature without providing a FEM model to simulate its process. The main goal of this PhD dissertation is to provide a comprehensive analysis of both ex-situ and in-situ fatigue modeling of a reinforced membrane. The proposed approach will leverage new techniques that speed up fatigue experiments and a constitutive model that can encompass the effects of humidity and temperature on the properties of the membrane in addition to their effects on expansion and contraction as well as the impacts of strain rate due to various RH cycles.

The current accelerated test is so time-consuming, especially for reinforced membranes, and therefore, the idea of coupling pressure-differential accelerated mechanical tests (ΔP-AMST) into in-situ complete modeling of a fuel cell can facilitate an efficient fatigue study of reinforced membranes. This mapping approach can be extended to estimate the mechanical fatigue lifetime of a membrane under various conditions in a complete fuel cell. Studying the ex-situ fatigue behavior of a reinforced membrane and comparing results with the in-situ study can provide a comprehensive method to assess the mechanical fatigue of a reinforced membrane. For both ex-situ and in-situ modeling, the developed constitutive model not only covers the effects of temperature, humidity, and strain rate but can also cover compressive stresses due to clamping pressure and the pressure differential between fuel and air applied on the membrane, while the original model just works for tensile stress. The possible correlations between ex-situ and in-situ experiments and models are investigated, which can help to achieve a more accurate estimation of the mechanical fatigue lifetime of reinforced membranes and create more practical protocols to assess the mechanical fatigue durability of reinforced membranes. To provide a more comprehensive lifetime estimation, we propose an extension of the model to incorporate the effects of chemical membrane degradation on fatigue durability.

The primary goal of this work is to develop a comprehensive model for the mechanical fatigue behavior of a reinforced membrane in a PEFC from both ex-situ and in-situ aspects. After making these models and verifying them, different fuel cell operation conditions are applied to the model, and the membrane fatigue lifetimes are assessed both in-situ and ex-situ such that the key interactions between operating parameters and fatigue durability can be better understood. To reach this objective, the following tasks are performed:

Ex-situ

- Tensile tests on the reinforced membrane to extract its mechanical properties in different ambient conditions by DMA.
- Developing required theories and FEM modeling for the tensile tests
- Mechanical loading fatigue tests by DMA
- FEM modeling of fatigue tests

In-situ

- Pressure-differential accelerated mechanical stress tests in different pressures and temperatures along with humidity cycles
- Developing required theories and FEM modeling of ΔP-AMST for stress distributions and fatigue lifetime
- Modeling a complete fuel cell in order to estimate in-situ membrane fatigue lifetime
- Coupling the chemical degradation with the mechanical fatigue model

Drawing a comparison between ex-situ and in-situ results to extract their probable correlation function is also done.

2 Theory

In this section, the theories that are used for finite element analysis for modeling tensile tests, ex-situ fatigue DMA tests, pressure-differential accelerated mechanical stress tests, and a complete fuel cell are developed.

2.1 General governing models and equations for membranes

Membranes, either non-reinforced or reinforced, show viscoelastic behavior like other polymers, which refers to the combination of viscous (flow-like) and elastic (spring-like) properties exhibited by certain materials when they are subjected to stress or deformation. When stress is applied to them, they will exhibit both a deformation that is proportional to the stress and a delayed, time-dependent relaxation [103]. Consequently, in order to model these materials, various springs and dashpots in different configurations, while every spring and dashpot itself can be linear or non-linear, have been presented in studies. In Figure 7, just three preliminary combinations showing that both springs and dashpots have linear behavior have been presented, while in more accurate and complex models, different combinations with non-linear springs and dashpots have been developed.

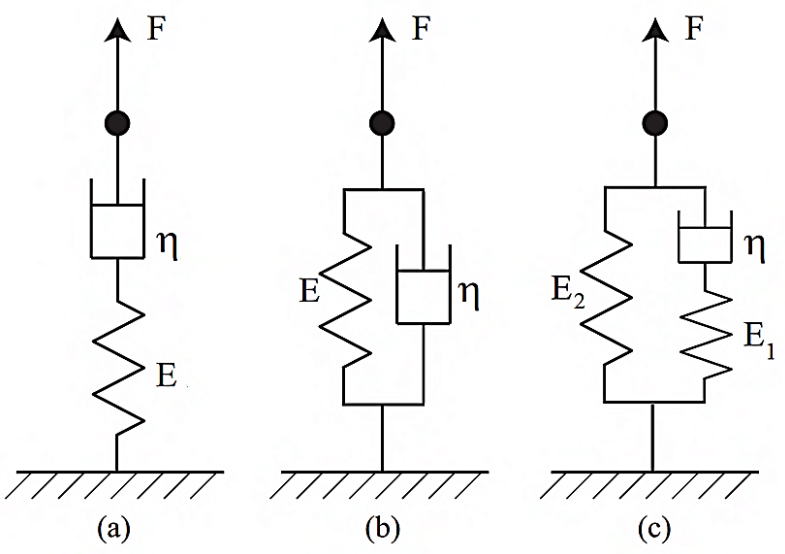

Figure 7 **Types of viscoelastic material models: (a) Maxwell; (b) Kelvin Voigt; (c) Standard linear solid, Reprinted from [103] with permission from Springer Nature**

In Table 3, a list of dominant isotropic viscoelastic models in studies has been provided [104]. The hyperelastic spring theories are non-linear elastic springs that show high strain under low stress as well as their nonlinearity, as shown in Figure 8.

Table 3 **The most popular isotropic governing models for viscoelastic polymers**

Spring hyperelastic model	Dashpot model
Neo-Hookean	Linear Viscoelastic
Yeoh	Power-Law Flow
Mooney-Rivlin	Bergstrom-Boyce
Polynomial	Exponential Energy Activated
Reduced Polynomial	Bergstrom-Boyce Network-Dependent
Marlow	Power-Law Flow with Strain-Dependence
Arruda-Boyce	Power-Law Shear and Volumetric Flow
Eight-chain	Sinh Energy Activation
Ogden	Tsai-Wu Power
Eight-chain	Bergstrom-Boyce Flow with Strain-Dependent m
Horgan and Saccomandi	Chaboche Non-Linear Kinematic Hardening Plasticity
Knowles	Double Power-Law
Extended Tube	G'Sell-Jonas
BAM	
Van der waals	
G'Sell-Jonas	

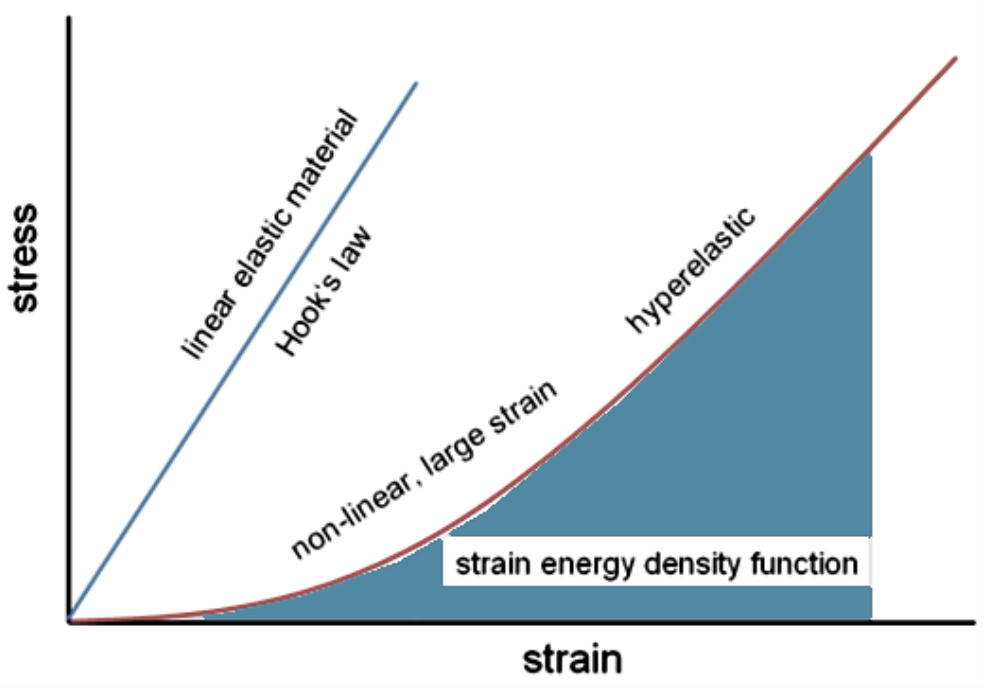

Figure 8 **A schematic comparison between linear elastic and hyperelastic materials [105]**

As the root concept of most mechanical models for viscoelastic materials like membranes, the Maxwell model has been explained here. In the Maxwell rheological model in Figure 9, there is a network comprised of a linear spring ($\sigma = E\varepsilon_1$) and a linear dashpot ($\sigma = \eta\dot{\varepsilon}_2$) as flow components (the relaxation stress part) that have been shown in Figure 9 [104]:

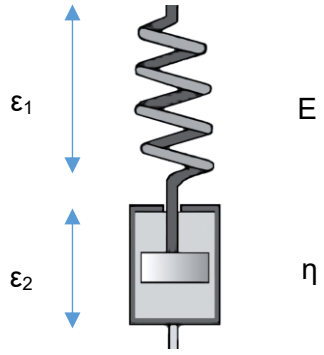

Figure 9 **Rheological representation of the Maxwell model for viscoelastic materials**

Therefore, the strain rate would have the following equation:

$$\dot{\varepsilon} = \frac{\mathrm{d}}{\mathrm{d}t}(\varepsilon_1 + \varepsilon_2) = \frac{\dot{\sigma}}{E} + \frac{\sigma}{\eta} \quad (1)$$

where ε is the strain, σ is stress, η is viscosity. Under the constant strain circumstance ($\dot{\varepsilon}$= 0), stress will be reduced with time from the initial stress σ_0 according to the equation (2):

$$\sigma(t) = \sigma_0 \exp\left[\frac{-t}{\eta/E}\right] \quad (2)$$

A relaxation modulus is defined by [106]:

$$E_r(t) = \frac{\sigma(t)}{\varepsilon} \quad (3)$$

$$E(t) = E_0 \exp\left[\frac{-t}{\eta/E}\right] \quad (4)$$

E_0 is the initial Young's modulus. The Maxwell model accurately predicts exponential stress decay over time, particularly for most polymers. Nevertheless, certain materials exhibit more intricate stress relaxation behaviors that cannot be adequately captured by a singular spring and dashpot configuration. To address these limitations, advanced models have been devised, incorporating multiple springs and dashpots arranged either in parallel or series. The generalized Maxwell model, for instance, incorporates several Maxwell elements arranged in parallel, acknowledging that relaxation occurs not at a singular time but across a range of times. A number of parallel Maxwell models create a multi-network Maxwell model as shown in Figure 10:

N networks of spring+ damper

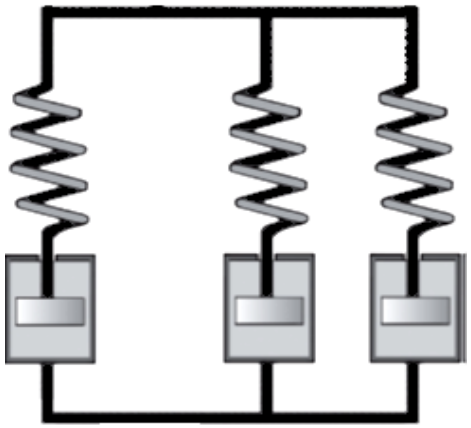

Figure 10 A multi-network Maxwell model

The effective stress relaxation modulus for this multi-network model when we also add a single spring (like the Wiechert-Maxwell model [107]) as displayed in Figure 11 will be equal to:

$$E_{\mathrm{R}}(t) = E_0 + \sum_{i=1}^{N} E_i e^{-t/\tau_i} \tag{5}$$

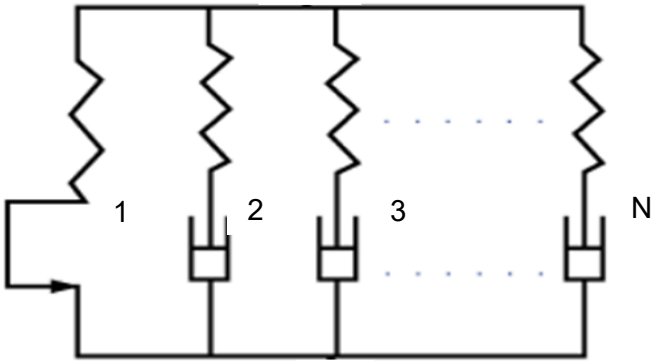

Figure 11 A multi-network Maxwell model plus a linear spring is equivalent to a Prony series.

While $\tau_i = \eta/E$ is the relaxation time and E_i and τ_i are named as Prony pairs. At the time of t=0, from equation (5), the effective stress relaxation modulus will be:

$$E_R(t=0) = E_0 + \sum_{i=1}^{N} E_i \tag{6}$$

Now, the effective stress relaxation modulus can be defined as below form [108]:

$$E_R(t) = E_0 + \sum_{i=1}^{N} m_i E_R(t=0)\, e^{-t/\tau_i} \tag{7}$$

$$m_i = \frac{E_i}{E_R(t=0)} \tag{8}$$

The shear modulus and bulk modulus are extracted from following equations [108]:

$$G(t) = \frac{E_R(t)}{2(1+\vartheta)} \tag{9}$$

$$K(t) = \frac{E_R(t)}{3(1-2\vartheta)} \tag{10}$$

In Figure 12, the stress relaxation for a non-reinforced membrane in two predefined strains has been displayed.

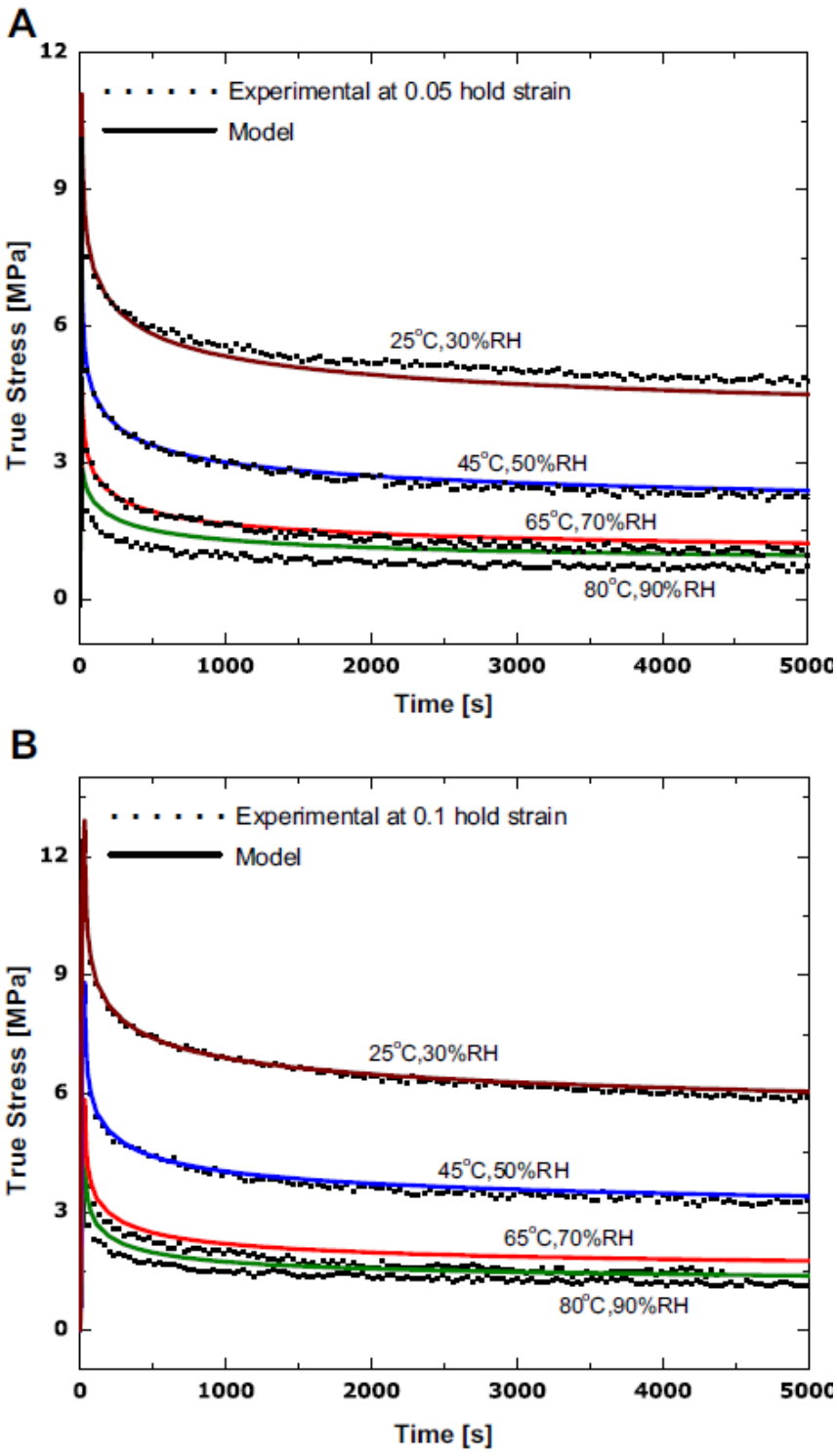

Figure 12 **Stress relaxation tests in different ambient conditions with two different strains, Reprinted from [79] with permission from Elsevier**

Generally, hyperelastic material models and viscoelasticity models are classified into phenomenological experience-based models such as Fung, Mooney–Rivlin, Ogden, Polynomial, Saint Venant–Kirchhoff, Yeoh, and Marlow approaches and mechanistic models such as Arruda–Boyce and the Neo-Hookean method, or a hybrid of phenomenological and mechanistic models such as Gent and Van der Waals. A phenomenological model is only applicable for the exact loading circumstances that have been validated, while mechanistic models that are based on micromechanics are more reliable for predicting the response in more general boundary conditions [104].

Viscoelasticity approaches with high accuracy and flexibility that can have a high potential for modeling a reinforced membrane are [80]: Bergstrom – Boyce Model, Arruda-Boyce Model, Hybrid Model, Three Network Model (TNM), and Parallel Network Model. Each model achieves high accuracy for different reasons. Take the Bergstrom–Boyce Model, for example, where the elastomer's true response is represented by two parallel networks, A and B. Network A is a nonlinear hyperelastic network, while network B comprises a nonlinear hyperelastic component in series with a nonlinear viscoelastic flow element. Additionally, an eight-chain model is employed for its springs. In this model, the macromolecules, or chain molecules, are typically situated along the diagonals of a unit cell within principal stretch space on average. The Bergstrom–Boyce model involves approximately 15 material parameters, and these can be extended by considering additional factors such as humidity [80]. One of the projects that has employed a TNM to obtain the time-dependent mechanical response due to relative humidity cycling on a reinforced membrane (GORE-SELECT-57) is Khattra and his co-workers' study [109]. One network is for the time-independent elastic-plastic response, and the other two networks define the time-dependent elastic-viscous response. Yoon et al. [110] utilized a nonlinear viscoelastic–viscoplastic constitutive model for a non-reinforced membrane that is a combination of the nonlinear viscoelastic Bergstrom-Boyce approach and a hydration-temperature-dependent empirical equation for elastic modulus. The elastic modulus, as a function of humidity and temperature, is defined as [110]:

$$E(\lambda, \theta) = \exp\{(A_1 \cdot \theta + B_1) \cdot \lambda_m + (A_2 \cdot \theta + B_2)\} \quad (11)$$

A1, A2, B1, and B2 are fitting constant and

$$\lambda_m = 0.043 + 17.81a_T - 39.85a_T^2 + 36.0a_T^3 \text{ for } 0 < a_T \leq 1 \quad (12)$$

The water content, denoted as λ_m, within Nafion is determined by the ratio of water molecules to charged sites ($SO_3^-H^+$). In the context of fuel cells, empirical measurements have established a connection between the water content in Nafion and the humidity levels within the fuel cell. α_T is the water activity (RH) defined by α_T = P_w/P_{sat} (θ), where P_w is water vapor pressure and P_{sat} is the saturation water vapor pressure at the temperature. The isotropic G'Sell-Jonas's theory is based on phenomenological observations that can encompass both temperature and humidity impacts on material strength along with their effects on elongations, while in the most complex and accurate models mentioned above, they consider only the temperature effect on material strength and the humidity effect in only on elongations, not material softness [111, 112]. This approach has demonstrated its accuracy for non-reinforced membranes [113] and also requires fewer fitting material parameters than other viscoelastic models. Due to its strong potential for non-reinforced membranes, this method was developed for this study. In the reinforced membrane of the fuel cell, it also experiences plastic deformation during high humidity fluctuations. From the presented material models in Table 3, only G'Sell-Jonas covers this, and for others, a term for a plastic deformation component should be added, which proves the comprehensiveness of this theory.

For comparing the result of modeling based on G'Sell-Jonas with other modeling methods, the tensile tests were modeled based on the Ogden approach too, which shows more accuracy than G'Sell-Jonas while for every temperature and RH, a minimum of 5 fitting parameters are needed, while in G'Sell-Jonas, with 7 fitting parameters, we can simulate all environmental conditions. In the Ogden Model, there isn't the effect of material softness due to humidity, and only its elongation effect is considered, while G'Sell-Jonas covers both.

2.2 Constitutive model based on G'Sell-Jonas and von Mises

A phenomenological model was introduced in 1979 by G'Sell and Jonas to predict the plastic behavior of solid polymers under constant real strain rates, particularly for semi-crystalline polymers whose glass transition temperature is lower than the service

temperature. Their study's objectives were to: (i) present a new technique for observing the creep plastic behavior of high-density polyethylene (HDPE for short) under constant true stress; (ii) relate this behavior to the typical response under constant load; and (iii) interpret the findings based on microstructural models. They implemented their approach using videometric testing methods created in their lab. Finally, they developed an equation that included temperature, humidity, and strain rate in both the viscoelastic and viscoplastic phases of polyethylene [111, 114]. After that, other researchers tried to use G'Sell-Jonas for other polymers, like membranes. Kusoglu et al. [112] found material parameters in the G'Sell-Jonas equation by fitting them to their tensile tests on PFSA, and after that, the stress-strain behavior of PFSA at various temperatures and humidity levels has been studied. In another work, Khattra and his co-worker [113] employed the G'Sell-Jonas method in their constitutive model in order to model the residual fatigue life of a non-reinforced membrane. In these previous works, the idea of using this method was ignited, but because all of them are for non-reinforced membranes and ex-situ modeling, a modified version of this G'Sell-Jonas method was generated in this study. It is worth mentioning that in this study, the membrane only experiences tensile stress for 60 s in its dry phase, and because it is a reinforced membrane and its mechanical strength is greater than that of the non-reinforced membrane in Figure 6, the effect of stress relaxation in fatigue modelling has been neglected. Besides, based on Figure 12, the gradient of graphs at higher temperatures is less, so for 60–90 °C, which covers most fuel cell operation time, this assumption, ignoring the effect of stress relaxation on analyses, is acceptable.

The phenomenological model developed by G'Sell-Jonas [111-113] is considered one of the most accurate and straightforward approaches for characterizing the constitutive response of membranes, as it incorporates the effects of temperature, humidity, and strain rate in a single equation:

$$\sigma_{G'Sell-Jonas}(\varepsilon, T, H) = K(T,H)\left(1 - e^{-w(H)\varepsilon}\right)e^{h(H)\varepsilon^2}\dot{\varepsilon}^m \quad (13)$$

$$K(T,H) = k_0 e^{(-\alpha T - \beta T)}\ ; \quad (14)$$

$$W(H) = w_0(1 - w_1 H); \quad (15)$$

$$h(H) = h_0(1 + hH); \tag{16}$$

$$m(H) = cH + d \tag{17}$$

In the above equations, k_0, α, β, w_0, w_1, h_0, h_1, c, and d are material fitting parameters. $K(T,H)\left(1 - e^{-w(H)\varepsilon}\right)$ is for viscoelastic, $e^{h(H)\varepsilon^2}$ is for plastic flow, and $\dot{\varepsilon}^m$ is for strain rate impact. In this new G'Sell-Jonas form, m, which accounts for strain rate effects, is also a function of temperature and humidity as it could not be adjusted with a constant value for all temperature and humidity spectra. The reinforced membrane exhibits linear elastic stress behavior under small stress (less than 1 MPa), which is calculable using:

$$\sigma_{ij} = \frac{E}{(1+\vartheta)}\left\{\varepsilon_{ij}^{el} + \frac{\vartheta}{(1-2\vartheta)}\varepsilon_{kk}\delta_{ij}\right\} \tag{18}$$

Where ε_{ij}^{el} is elastic strain components, ε_{kk} is the trace of the strain tensor, ϑ is Poisson's ratio, δ_{ij} is the Kronecker's delta, and E (T, RH) is Young's modulus as a function of the membrane's temperature and relative humidity.

By using the J_2 plasticity theory, the plastic component of the constituent response is computed in which the von Mises effective stress is stated in terms of the deviatoric components of the stress as:

$$\sigma_{mises} = \sqrt{\frac{3}{2}S_{ij}} \tag{19}$$

$$S_{ij} = \sigma_{ij} - \frac{1}{3}\sigma_{kk}\delta_{ij} \tag{20}$$

where S_{ij} is the deviatoric stress tensor obtained by removing the volumetric (or hydrostatic) stress component σ_{kk} with the assumption that the plastic deformation does not happen under the latter. The associative plastic flow rule is used for the plastic slip rate by employing the yield function as the following:

$$F_y = \sigma_{mises} - \sigma_y \quad (21)$$

where σ_y stands for the present yield stress. To obtain the updated yield stress, the isotropic hardening law is applied.

$$\sigma_y = \sigma_{y0} + \sigma_{G'Sell-Jonas}(\varepsilon^p, T, H) \quad (22)$$

Thereby, σ_{y0} is the initial yield stress, and ε^p is the effective plastic strain magnitude. Using the additive decomposition assumption, $\varepsilon = \varepsilon_{elastic} + \varepsilon_{inelastic}$, the elastic strain tensor required for equation (18) is obtained. The inelastic strain is determined by the following relationship:

$$\varepsilon_{inelastic} = \varepsilon_{thermal} + \varepsilon_{hygral} + \varepsilon_{plastic} \quad (23)$$

$$\varepsilon_{thermal} = \alpha\,(T - T_{ref}) \quad (24)$$

where α is the coefficient of thermal expansion ($1/K$), T and T_{ref} are current and reference temperatures, respectively. Because of water sorption/desorption, there is a volumetric change in the membrane, resulting in hygral strain, which is stated as:

$$\varepsilon_{hygra\_in\text{-}planel} = a \times ln\left(\frac{1}{1-\varphi_w}\right)\frac{T}{T_{ref}} \quad (25)$$

$$\varepsilon_{hygra\_through\text{-}plane} = b \times \varepsilon_{hygra\_in\text{-}plane} \quad (26)$$

According to [70, 80, 109, 115], a and b are the reinforced membrane's optimal fitting parameters for the swelling ratio in-plane and through-plane.

In Table 4, more details of the swelling ratio in plane and in thickness for one non-reinforced membrane and two types of reinforced membranes have been provided.

Table 4 Comparison of swelling ratio of Nafion 212 (Non-reinforced membrane), Nafion XL, and ePTFE reinforced PSFA in liquid water at 24±1 °C, Reprinted from [70] with permission from Elsevier

	Change in length [%]		Change in Thickness [%]	Swelling Ratio thickness/plane	Change in Volume [%]
	MD	TD			
Nafion 212	8.14 ± 0.24	8.96 ± 1.31	8.93 ± 1.03	1.10	28.35 ± 2.60
Nafion XL	1.09 ± 0.36	5.01 ± 0.73	15.64 ± 1.63	14.35 (TD) 3.12 (MD)	22.76 ± 2.74
Nafion XL[a]	1.00	5.00	–	–	–
ePTFE reinforced PFSA	1.50	1.20		$\sim 10^{c}$	

[a] Dupont Nafion XL membrane property sheet, measured from 50%RH to liquid water at 23 °C.

According to the equation below [80], the water volume fraction φ_w depends on the membrane's water content λ, equivalent weight EW, and density ρ_p.

$$\varphi_w = \frac{18\lambda}{\frac{EW}{\rho_p} + 18\lambda} \tag{27}$$

In the context of a polymer with sulfonic acid groups in the acid form, the equivalent weight refers to the number of grams of the dry polymer per mole of sulfonic acid groups. It represents the mass of the polymer per unit of acidic functionality. Knowing the molar mass of the dry polymer and the number of sulfonic acid groups per mole of polymer, the equivalent weight can be calculated. The equivalent weight for a reinforced membrane would be the same as that of a non-reinforced membrane, as the reinforcement material does not affect the chemical composition or active component of the membrane.

2.3 Modifying the G'Sell-Jonas equation to support compressive stresses

The G'Sell-Jonas theory is limited to modeling only tensile stress, whereas in real fuel cell operation conditions the membrane is subjected to both tensile and compressive

loads. During the operation of the PEFC, several factors can lead to compressive and tensile stress on the membrane:

Clamp Compression: The fuel cell stack is typically held together by clamping forces to ensure a proper seal and to maintain the structural integrity of the cell. These clamping forces can induce compressive stress on the membrane.

Thermal cycles: As the fuel cell operates and heats up, temperature changes can cause different components, including the membrane, to expand or contract. If the expansion is constrained, it can lead to compressive stresses in the membrane and vice versa for tensile stress.

Humidity cycles: Changes in the humidity level can cause the membrane to swell or contract, which may result in compressive or tensile stresses, respectively.

Air and fuel pressure: Air and fuel pressure are essential operating parameters in a PEFC, and they can significantly influence the cell's performance and overall efficiency, which can cause tensile and compressive stresses on the membrane.

To address this limitation of G'Sell-Jonas theory that can only work for tensile stresses, a generalized G'Sell-Jonas equation has been developed to model both tensile and compressive stresses:

$$\sigma(\varepsilon, T, H)_{generalized\ G'Sell-Jonas} = step(\varepsilon)K(T,H)\left(1 - e^{-w(H)abs(\varepsilon)}\right)e^{h(H)\varepsilon^2}\dot{\varepsilon}^m \tag{28}$$

$$step(\varepsilon) = \begin{cases} +1, & \varepsilon \geq 0 \\ -1, & \varepsilon < 0 \end{cases} \tag{29}$$

The generalized G'Sell-Jonas equation assumes that the magnitude of strain in the membrane is the same for both compressive and tensile stresses. Additionally, the membrane is assumed to be isotropic in-plane, but the thermal and swelling expansion coefficients in the thickness direction are 10 times larger [70, 80, 109, 115] than in plane. The generalized G'Sell-Jonas equation is used as an isotropic hardening function, which is added to the initial yield stress to calculate the updated yield stress at each time step.

2.4 Constitutive model based on Ogden theory

One of the strongest phenomenological models for hyperplastic materials such as rubbers, polymers, and biological tissue is the Ogden approach (Figure 13). Phenomenological models of hyperelasticity utilize experimental data with a minimized number of material parameters to determine strain potentials. In this model, the strain potential is calculated based on the following equation in terms of the principal stretches λ_j, j=1,2,3 as [116]:

$$W = \sum_{n=1}^{N} \frac{\mu_n}{\alpha_n} (\lambda_1{}^{\alpha_n} + \lambda_1{}^{\alpha_n} + \lambda_1{}^{\alpha_n} - 3) \tag{30}$$

μ_n and α_n are material parameters. In Abaqus, in order to consider temperature impacts on material behavior in the Ogden model, the following equation is exploited [108]:

$$W = \sum_{n=1}^{N} \frac{2\mu_n}{\alpha_n{}^2} \left(\overline{\lambda_1}^{\alpha_n} + \overline{\lambda_2}^{\alpha_n} + \overline{\lambda_3}^{\alpha_n} - 3\right) + \sum_{n=1}^{N} \frac{1}{D_n} + (J_{el} - 1)^{2n} \tag{31}$$

N is a material parameter; and μ_n, α_n, and D_n are temperature-dependent material parameters and the deviatoric principal stretches $\overline{\lambda_j} = J^{\frac{-1}{3}} \lambda_j$. The Mooney-Rivlin and neo-Hookean forms can also be obtained from the general Ogden strain energy potential for specific selections of μ_n and α_n.

The elastic volume ratio, J_{el}, relates the total volume ratio, J, and the thermal volume ratio (is a material property that describes how the volume of a material changes with temperature), J_{th}:

$$J_{el} = \frac{J}{J_{th}} \tag{32}$$

and $J_{th} = (1 + \varepsilon^{th})^3$

where $\varepsilon^{th} = \alpha \Delta\theta$ is the linear thermal expansion strain, α is the thermal expansion coefficient, and $\Delta\theta$ is the temperature change.

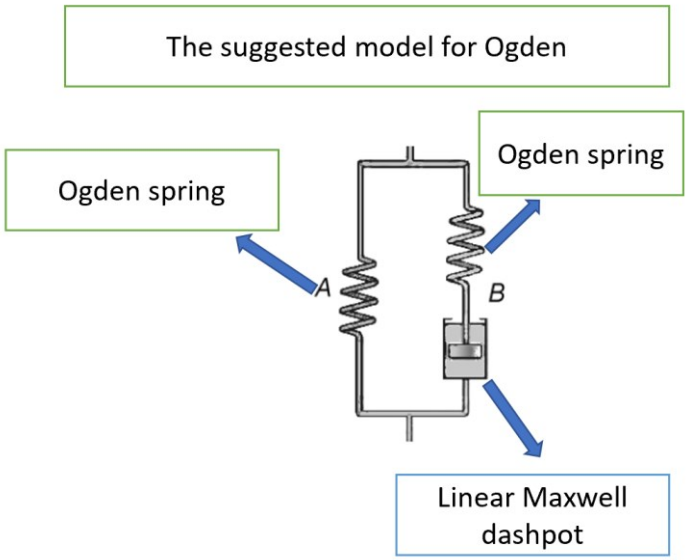

Figure 13 The Ogden theory when the effects of stress relaxation have been considered

2.5 Other theories behind FEM fatigue modeling for this study

2.5.1 Calculating the Young's modulus of the catalyst layer

Literature articles like [61, 70, 109] provide information on the properties of the other parts of a full fuel cell in the finite element model. Extracting the properties of the CL, however, is challenging because it is deposited on the membrane as a wet film that forms a thin, porous layer after solvent evaporation. However, based on solid mechanics [117, 118] by using the Young's modulus of the membrane and catalyst coated membrane (CCM), the young modulus of the CL is calculated from (33):

$$E_{Cl} = (2 + \frac{A_m}{A_{Cl}})E_{ccm} - E_m \tag{33}$$

2.5.2 Goodman theory for modifying amplitude stress

The impact of residual stress from the pressure differential, which appears as mean stress in fatigue cycles, is also not negligible. As a result, it is nonsensical to base decisions solely on amplitude stress (σ_a), and the Goodman relation [119] is used to derive modified amplitude stresses, as illustrated by the following equation:

$$\sigma_{a\_modified} = \begin{cases} \sigma_a + \dfrac{\sigma_e}{\sigma_{ult}}\sigma_m & for \quad \sigma_e < \sigma_m \\ \sigma_a & \sigma_e \geq \sigma_m \end{cases} \tag{34}$$

where mean stress is σ_m, ultimate tensile strength is σ_{ult}, and fatigue endurance is σ_e.

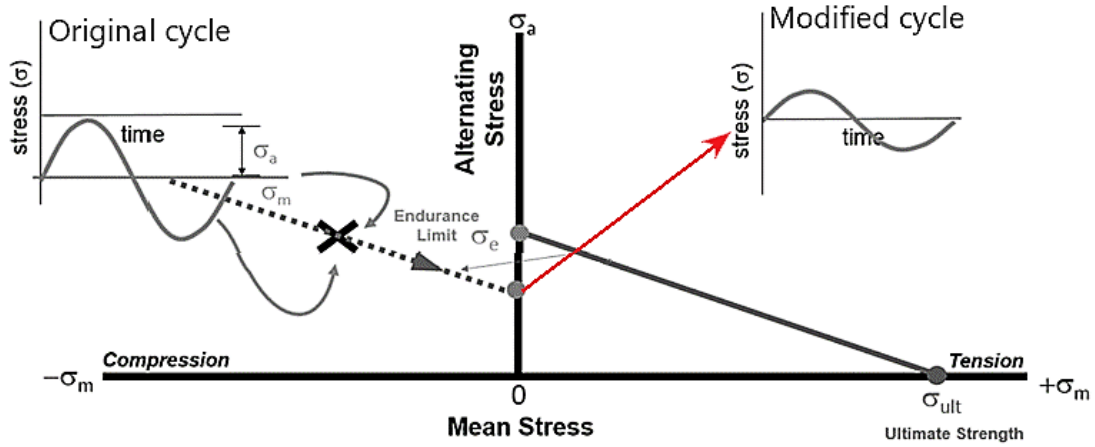

Figure 14 Modified amplitude stress calculation using the Goodman method [120]

A Goodman diagram (Figure 14) is a graphical representation illustrating the relationship between mean stress (σ_m) and alternating stress (σ_a), which leads to fatigue failure in a material. The diagram features two axes: the horizontal axis represents mean stress, and the vertical axis represents alternating stress.

The Goodman diagram consists of three key lines:

Goodman Line: This straight line connects the endurance limit (σ_e) on the vertical axis with the ultimate strength (σ_{Ult}) on the horizontal axis. Its purpose is to demarcate the boundary between safe and unsafe combinations of mean and alternating stresses.

Endurance Limit Line: Represented as a horizontal line, it shows the maximum value of alternating stress that a material can endure without failing, even after an infinite number of cycles. This line is parallel to the horizontal axis and intersects the endurance limit point.

Ultimate Strength Line: Displayed as a vertical line, it indicates the maximum value of mean stress a material can withstand without breaking. Like the endurance limit line, this line is parallel to the vertical axis and passes through the ultimate strength point.

The regions on the diagram are categorized as follows:

Safe Zone: This area lies below the Goodman line and to the left of the ultimate strength line. In this zone, the material can survive an infinite number of cycles without failure.

Unsafe Zone: The region above the Goodman line or to the right of the ultimate strength line is considered unsafe. Materials experiencing stress combinations within this zone will fail after a finite number of cycles.

Engineers and materials scientists utilize the Goodman diagram to assess the fatigue performance of materials and make informed decisions in design and operational scenarios. By staying within the safe zone, they can ensure the durability and reliability of components and structures, preventing fatigue-related failures.

2.5.3 Plastic dissipation energy

Plastic dissipation energy, also known as plastic work or hysteresis energy, refers to the energy that is dissipated as heat when a material undergoes plastic deformation. It is a measure of the amount of energy that is absorbed by the material during plastic deformation and is an important parameter in determining the fatigue behavior and crack initiation and propagation of materials.

The plastic dissipation energy can be calculated by integrating the area under the stress-strain curve during plastic deformation using the following equation, illustrated by grey color in Figure 15.

$$w = \int \sigma d\varepsilon - \sigma \frac{\varepsilon_{elastic}}{2} \tag{35}$$

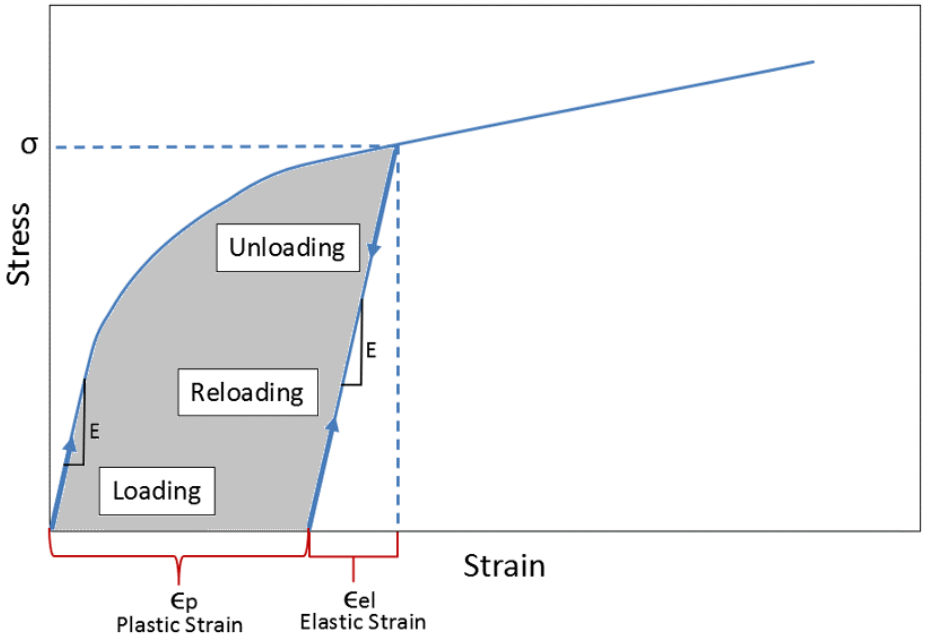

Figure 15 How the plastic dissipation energy is calculated in every fatigue cycle.

where w is the plastic dissipation energy, $\varepsilon_{plastic}$ is the plastic strain, and σ is the stress. The plastic dissipation energy is related to the fatigue behavior of a material, as it is a measure of the amount of energy that is absorbed by the material during cyclic loading. During cyclic loading, a material undergoes repeated plastic deformation, leading to the accumulation of plastic dissipation energy. The accumulation of this energy can lead to fatigue failure, which is a common failure mechanism in many materials.

3 Experimental Methodology

In order to have a comprehensive study on the mechanical fatigue of the reinforced membrane, both ex-situ and in-situ experiments and modelling have been done. Ex-situ tensile tests in different environmental conditions were done to find material parameters for the developed G'Sell-Jonas model. Ex-situ fatigue testing with DMA is for investigating the fatigue behavior of the membrane in different environmental conditions. In DMA, the source of stress is mechanical loading, not expansion and contraction due to humidity and temperature cycles conditions. To extend its results to a full fuel cell under its real conditions, where humidity and temperature cycles are the sources of applied stresses on the membrane, in the in-situ phase, the pressure-differential accelerated mechanical stress tests have been implemented to see the membrane's mechanical fatigue behavior in real conditions.

3.1 Ex-Situ approach

3.1.1 The test procedure for tensile tests

The study used membranes from a single batch of isotropic commercially available reinforced membranes with thickness 15 μm (made of PFSA ionomer and reinforced with an ePTFE core layer like Figure 5). To eliminate any possible adverse effects, the samples were left at room temperature for a few days before the test, and without any preprocessing, they were mounted on tensile test grippers. Tensile testing was conducted using a DMA (TA Instruments Q800) with a temperature and humidity chamber. Prior to the tensile test, the samples were kept at the desired temperature and relative humidity for 30 minutes in an isothermal state to ensure sufficient equilibration in the sample length. The DMA tensile test results are shown as normal stress and normal strain. For tensile tests, samples were cut rectangularly with 20 mm as length and 5 mm as width by a sharp blade. From each side, 5 mm of the length was under the grips, and so the actual size of the membrane under tensile stress is 10 mm × 5 mm. The samples were mounted on the DMA like in Figure 17 with a tweezer. In DMA, for every test, first humidity and temperature reach the specified point, and after that, the membrane is kept in that condition for 30 minutes. Next, the strain with the specified rate is applied to the membrane until it reaches 100% strain.

3.1.2 The test procedure for fatigue tests in DMA

During the ex-situ fatigue testing stage, the dogbone-shaped membrane is subjected to cyclic loads to imitate the mechanical stress conditions it would experience from expansions and contractions. The testing process takes place under specific environmental conditions of 25 ^{0}C and 90% RH and utilizes a DMA model Q850 to apply a mechanical load with an adjusted mean, amplitude, and frequency (Figure 16-a) to the membrane (Figure 16-b). The testing continues until the membrane experiences a sudden mechanical rupture. This process helps to evaluate the durability and strength of the membrane material under conditions that are representative of its intended use.

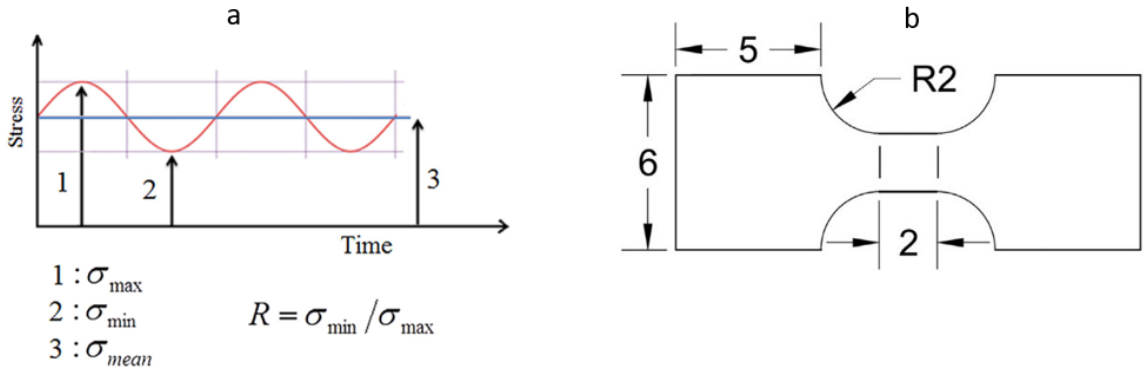

Figure 16 **a) Periodic force (sinusoidal), b) dogbone shaped samples, from [121] with permission from Elsevier**

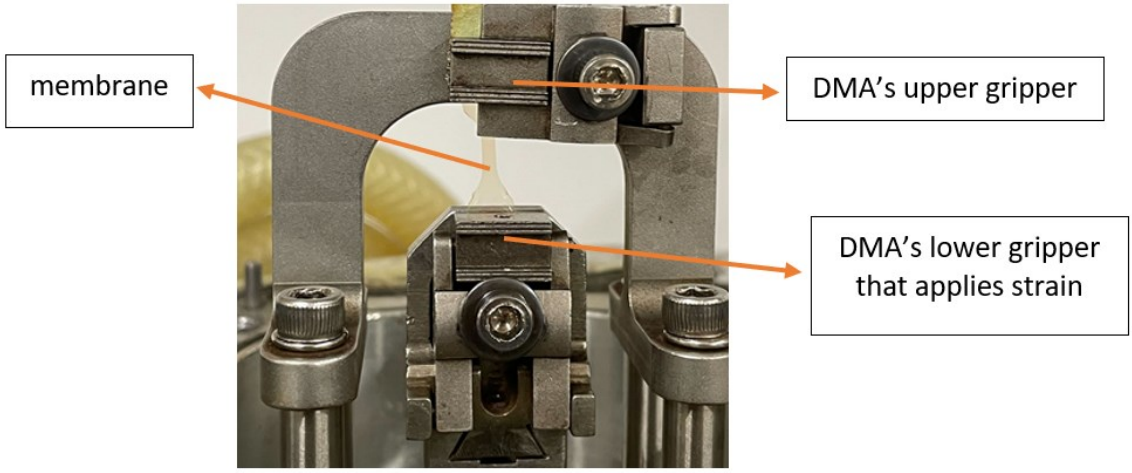

Figure 17 **How the membrane is mounted on DMA Q850 for fatigue test.**

In the fatigue tests done in DMA, the force track (force track is just a terminology in DMA Q850) is 150% (= $\frac{F_{static}}{F_{OSC}}$×100%)), $R = \frac{\sigma_{min}}{\sigma_{max}} = 0.2$, frequency is 10 Hz and 5 Hz, and the max stress and min stress applied by DMA on the membrane are defined as the following equations:

$$F_{max} = (Force\ track + 100\%) \times F_{Oscillation\ Force} = 2.5\ F_{Oscillation\ Force} \quad (36)$$

$$F_{min} = (Force\ track - 100\%) \times F_{Oscillation\ Force} = 0.5\ F_{Oscillation\ Force} \quad (37)$$

$$F_{mean} = \frac{1}{2}(F_{min} + F_{max}) = Force\ track \times F_{Oscillation\ Force} = F_{Static} \quad (38)$$

$$F_{Oscillation\ Force} = Stress \times Area$$

$$R = \frac{\sigma_{min}}{\sigma_{max}} = 0.2 \quad (39)$$

3.2 In-Situ approach

3.2.1 Pressure-differential accelerated mechanical stress test (ΔP-AMST)

The ΔP-AMST method involves subjecting the membrane to cyclic humidity changes and a pressure differential between the cathode and anode sides, resulting in a higher triaxial stress amplitude on the membrane. Figure 18 depicts a schematic representation of the experimental setup used in this method. The setup includes a clear polycarbonate spacer (19 mm thick) with a circular hole through its thickness, placed on top of the frame. A pressurized bladder, set at 2 bar, is installed to ensure uniform compression and sealing of the fuel cell assembly. The assembly comprises a reinforced membrane, a gas diffusion layer (GDL) larger than the hole diameter (25.4 mm) in the spacer and, two Kapton layers like illustrated in Figure 19 The GDL controls the membrane shape and prevents the formation of water droplets on the membrane, and Kapton layers are responsible for attaching GDL to the membrane and sealing the anode and cathode sides. First, all Kapton layers, membranes, and GDL are cut using a cut die. There is an empty rectangle on both Kapton layers. The membrane adheres to one of them, GDL

adheres to another, and two Kapton layers stick to each other to complete the sample. The membrane and GDL are square-shaped, with dimensions of 40 mm × 40 mm for this test. For running the ΔP-AMST tests, a Greenlight Innovation 50 cm^2 (active area) fuel cell hardware, as shown in Figure 20, is connected to test station Greenlight Innovation G40 (Figure 21) to conduct stress tests on the membrane. The station included water-injected evaporator-type humidifiers, mass flow controllers, and a backpressure control system, among other features. To cause membrane fatigue, the station employed ΔP-AMST, which involves applying quick, large-amplitude relative humidity cycles at 90 °C. The difference between ΔP-AMST and the standard DOE AMSTs protocol is that a wide range of pressure differentials are used in ΔP-AMST to generate residual stress in the membrane and hasten its mechanical fatigue degradation while in AMSTs' protocol, the pressure differential between the anode and cathode sides is zero [97]. The carrier gas in the original DOE procedure is air; however, nitrogen was employed in the ΔP-AMST in this study to eliminate any influence from chemical degradation. In addition, in the DOE protocol, cycles from 0% RH (2 min) to 90 °C dewpoint (2 min) are applied to the MEA [122]. To further accelerate the degradation process, consecutive humidity cycles consisting of a 60 s dry phase (0% RH) and a 30 s wet phase (100% RH) were utilized in this study, which is four times faster than the method used in a previous study [97]. The anode and cathode compartments of the test station had a nitrogen flow rate of 4 slpm. The humidity cycling continued until the membrane failed due to fatigue fracture, indicating a loss of pressure differential, similar to reactant gas leaking over a deteriorated membrane in a PEFC. It is worth mentioning that the following criteria have been considered to assess when the membrane has failed the ΔP-AMST tests: When the applied pressure differential in a test is less than 5 kPa and reduces to 1 kPa after passing humidity cycles due to gas crossover caused by microcracks and holes, it shows that the membrane has failed, and the test is terminated. When the applied pressure differential in our test is greater than 5 kPa, the test is terminated when it falls by one-fifth of the set pressure.

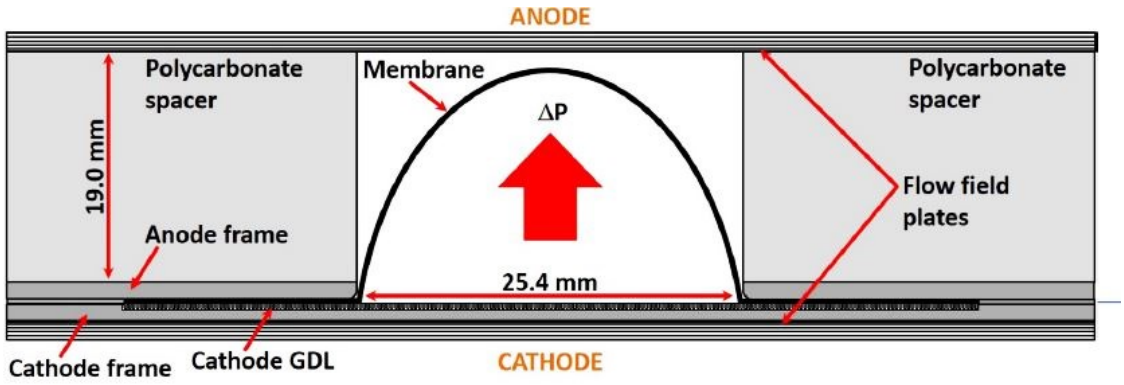

Figure 18 Cross-sectional view of the fuel cell test assembly in ΔP-AMST [97]

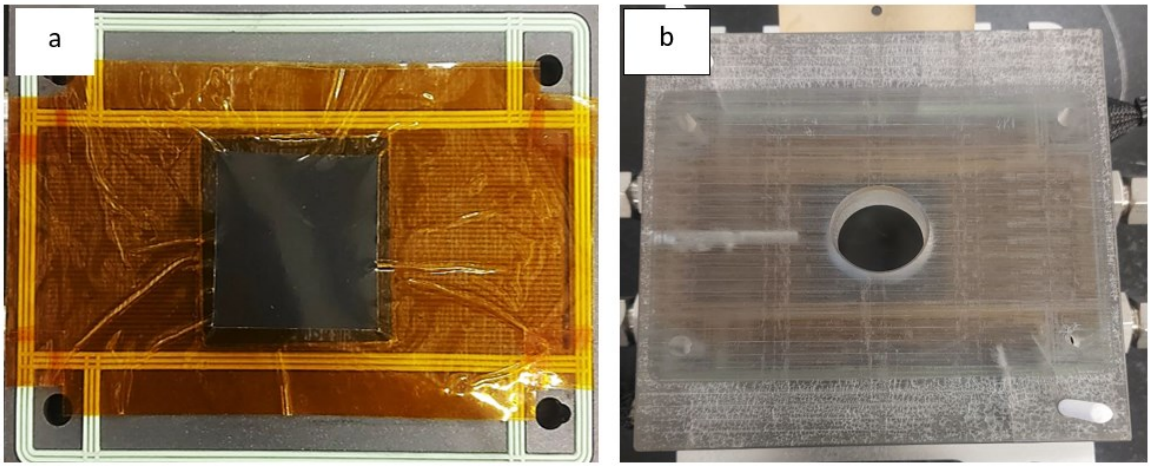

Figure 19 a) A prepared sample for ΔP-AMST, b) the spacer on the sample.

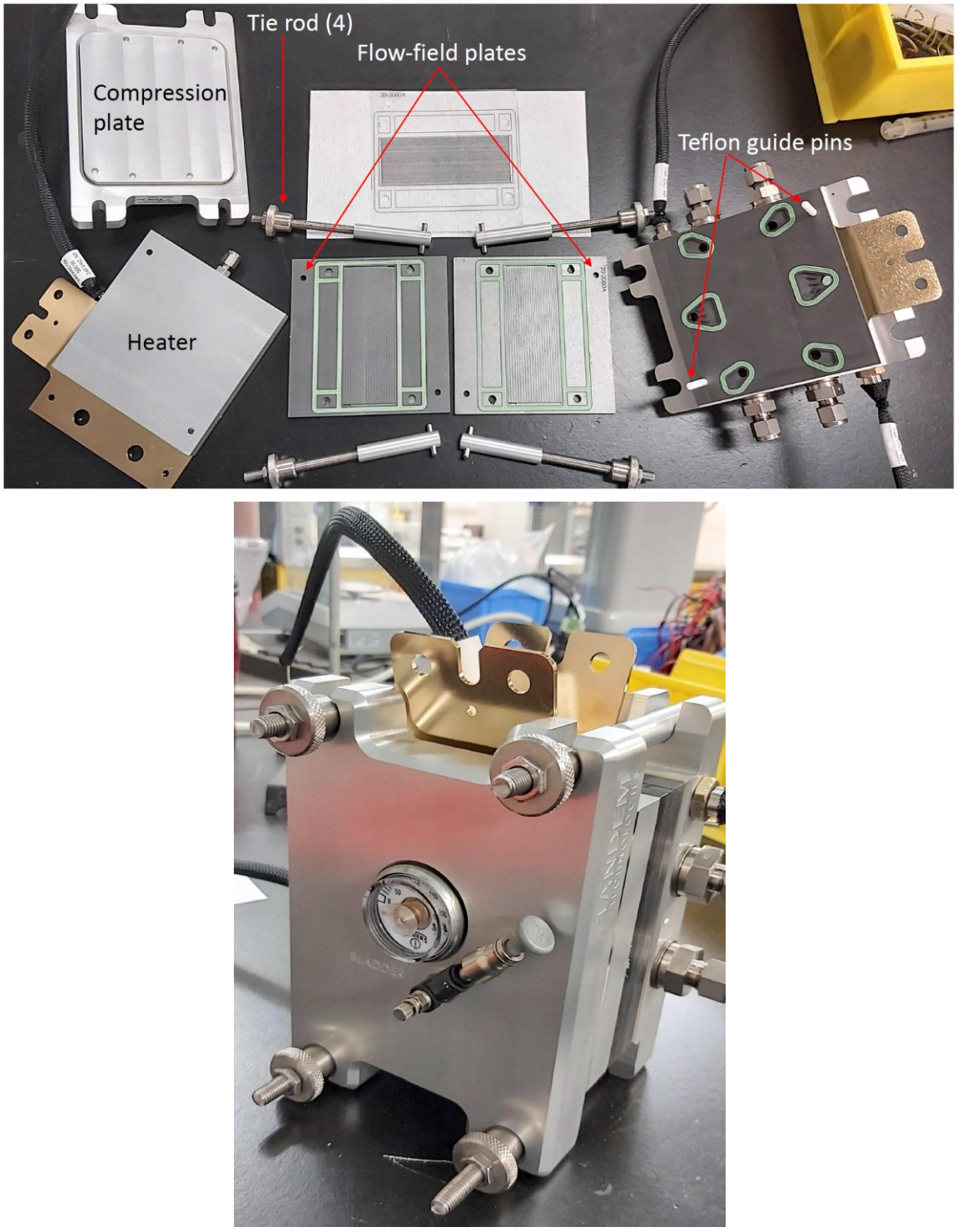

Figure 20 The cell hardware used for ΔP-AMST tests

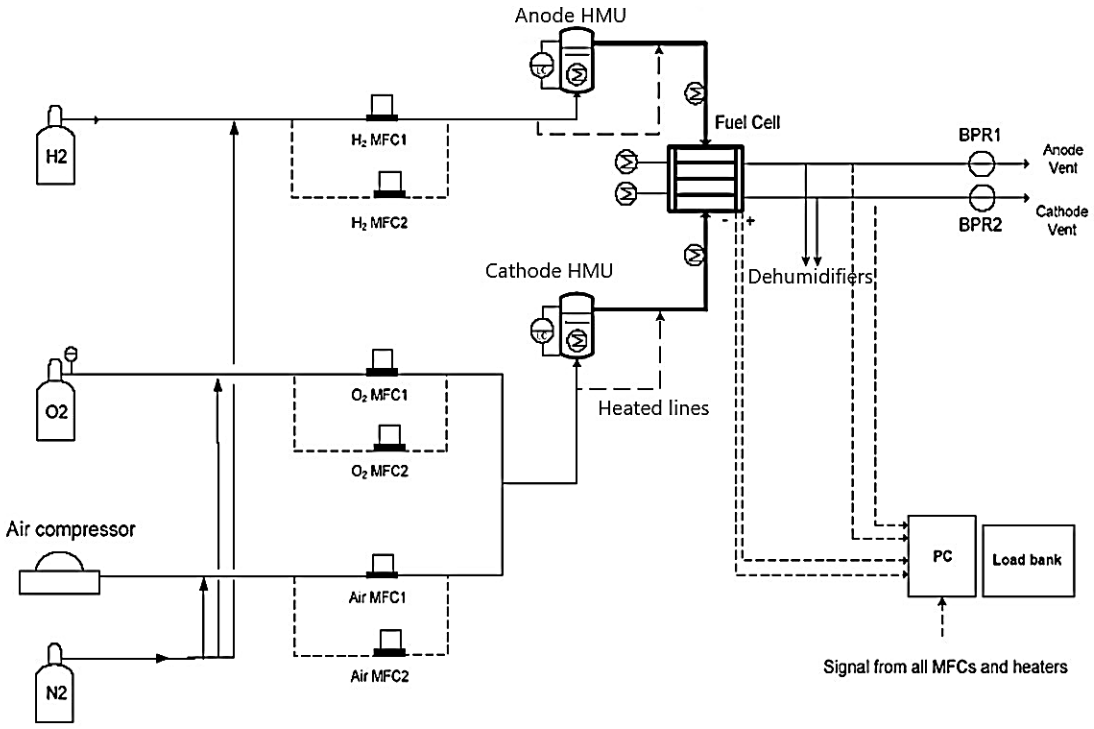

Figure 21 An overall view of fuel cell test station structure, Reprinted from [123] with permission from Elsevier

3.2.2 Uncertainty and error analysis on fuel cell test station results

In this study, the pressures, temperatures, and gas flow rates from the fuel cell test station can influence the measurement results and their uncertainty.

Pressure Measurements: For pressure measurements, the error tolerance can vary depending on factors such as the pressure range being measured, and the precision required for the specific test. In many cases, pressure sensors with accuracies of around ±0.1% to ±1% of the full-scale range are commonly used in industrial applications.

Temperature Measurements: For temperature measurements, the error tolerance is typically expressed in degrees Celsius (°C) or Fahrenheit (°F). High-precision temperature sensors, such as platinum resistance temperature detectors (RTDs) or thermocouples, may have accuracies in the range of ±0.1°C to ±1°C.

Relative Humidity Measurements: Relative humidity is measured as a percentage, and the error tolerance can vary based on the sensor type and calibration. High-precision humidity sensors may have accuracies in the range of ±1% to ±5%.

Flow Rate Measurements: Mass flow controllers (MFCs) are commonly used for controlling gas flow rates in fuel cell test stations. MFCs typically have specified accuracies, and these can vary based on factors such as the type of gas being controlled and the flow rate range. Accuracies of ±1% to ±2% of full scale are common for MFCs.

Therefore, when a fuel cell test station is in a healthy and calibrated situation, a maximum deviation of ±1% in pressure, ±1°C in temperature, ±5% in RH, and ±2% in flow rate may occur.

In these tests, a dry flow from N_2 cylinders with 0% RH is supplied to the cell for the dry phase. Since the reason for failure is tensile stresses and all tests have the same level of dryness, the effects of a ±5% deviation in RH are considered negligible. Consequently, the maximum deviation in extracted fatigue lifetime due to these errors can be up to 5%, assuming a linear correlation. However, because the membrane won't be completely dry during the dry phase, the deviation at 100% RH will likely be much less than 5%.

In our fuel cell test station, the deviations in temperature, relative humidity (RH), and flow rate are all less than 2%, while the pressure is less than 10% in the worst case. These deviations have been shown in section 5.1 (Estimating the in-situ mechanical fatigue lifetime of the reinforced membrane)

For membrane thickness deviation, there isn't any open information in the membrane's data sheets and manufacturers' websites. However, based on data sheets from different companies and some comparisons, we can estimate that it would be less than 10%.

4 Results and discussion

In this section, the results of experiments that have been done in the methodology section and the FEM modelling of those tests with discussions are presented.

4.1 Ex-situ approach

4.1.1 Tensile tests results

To ensure accuracy, the test was conducted three times under extreme conditions (80 °C – 90% RH), and all three results were found to be consistent with each other, as depicted in Figure 22. The first step of the study involved examining the tensile stress-strain behavior of the reinforced membrane in four different environmental conditions specific to PEFCs: (25 °C, 30% RH), (25 °C, 90% RH), (80 °C, 30% RH), and (80 °C, 90% RH), as well as two different strain rates of 0.01/min and 0.1/min. The resulting strain-stress curves for the reinforced membrane are presented in Figure 23.

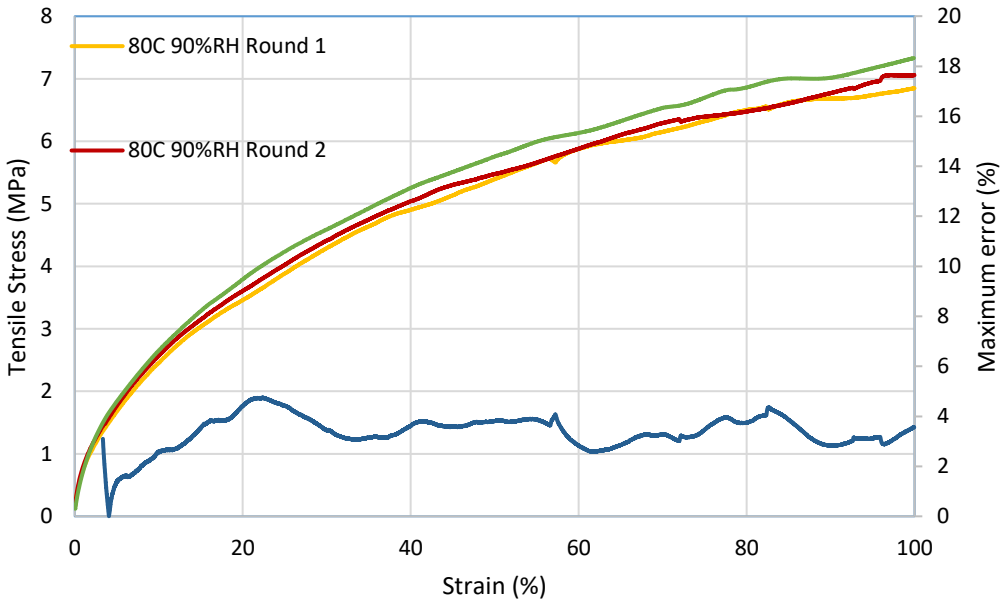

Figure 22 Repeating the tensile test with a 0.01 strain rate at 80 °C and 90% RH three times.

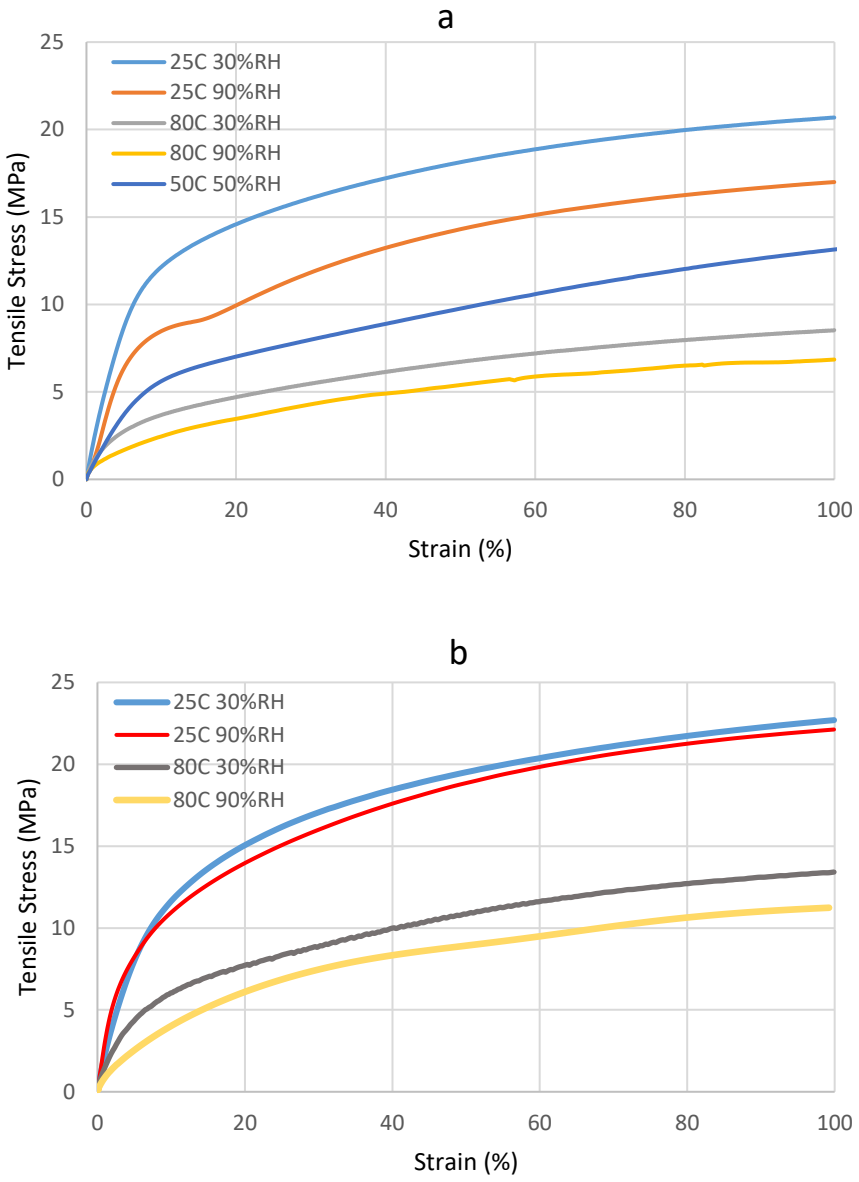

Figure 23 **a) Tensile tests in different temperatures and relative humidity with a strain rate of 0.01/min; b) a strain rate of 0.1/min.**

In Figure 23, the reinforced membrane, along with non-reinforced and other reinforced membranes, demonstrates that temperature has a more significant impact than humidity. When the temperature is lower, the membrane experiences higher stress at the same strain, whereas higher humidity leads to lower stress at the same temperature. Consequently, elevated temperatures and humidity cause the membrane to become softer, increasing the risk of failure under lower stress conditions. To determine the Young's modulus, we need to find the slope of the linear portion of the stress-strain curve,

which corresponds to the material's elastic behavior and here, the slope of a line between 0% stain and 2% strain (that is a common criterion in solid mechanics [124]) has been used for calculating Young's modulus. In two graphs with the same humidity but different temperatures (25 °C, 30% RH and 80 °C, 30% RH), the Young's modulus decreased from 209MPa to 82 MPa. In contrast, at the same temperature but different humidity levels (25 °C, 30% RH and 25 °C, 90% RH), it decreased from 209 MPa to 128 MPa at 2% strain, and the difference between their tangent lines decreased more as the strain increased (graphs blue and red). As shown in Figure 23-b, at higher strain rates, the effect of humidity versus temperature on the Young's modulus decreased more. Overall, it is evident that the membrane exhibits greater rigidity at higher strain rates because there is not enough time for stress relaxation. The reinforced membrane displays significantly greater mechanical strength compared to a non-reinforced membrane made of PFSA, almost double the strength at 23 °C and 50% RH as reported in reference [58]. In general, materials with higher mechanical strength will experience less strain for a given level of stress. This reinforced membrane is thinner and displays less stress at the same strain compared to other reinforced membranes like Nafion XL (with a thickness of 27.5 μm) and the GORE-SELECT® membrane (with a thickness of 20 μm), all of which are in the MD directions at 25 ^{0}C and 50% RH [66, 115]. To evaluate whether our reinforced membrane is isotropic in the MD and TD directions, two tensile tests in the MD and TD directions were done. In the first test, the ambient conditions in DMA were 25 °C and 50% RH, and a strain load of 0.05/min was applied to the membrane. In the second test, 80 °C, 90% RH, and a strain rate of 0.01/min were selected. Based on Figure 24, it is reasonable to consider the reinforced membrane in this study to be isotropic in plane, especially in hot temperatures and humidity at lower strain rates. In the first test, the variance in tensile stress between the MD and TD is under 5% for strains below 10%. However, for higher strains, the difference increases to approximately 10-15%. In the second test, a similar pattern is observed, with the stress difference between MD and TD staying below 5% until strains reach 20%. Beyond that point, it rises to around 10-15%. From the perspective of Young's modulus, both tests show that the Young's modulus values in MD and TD are equivalent.

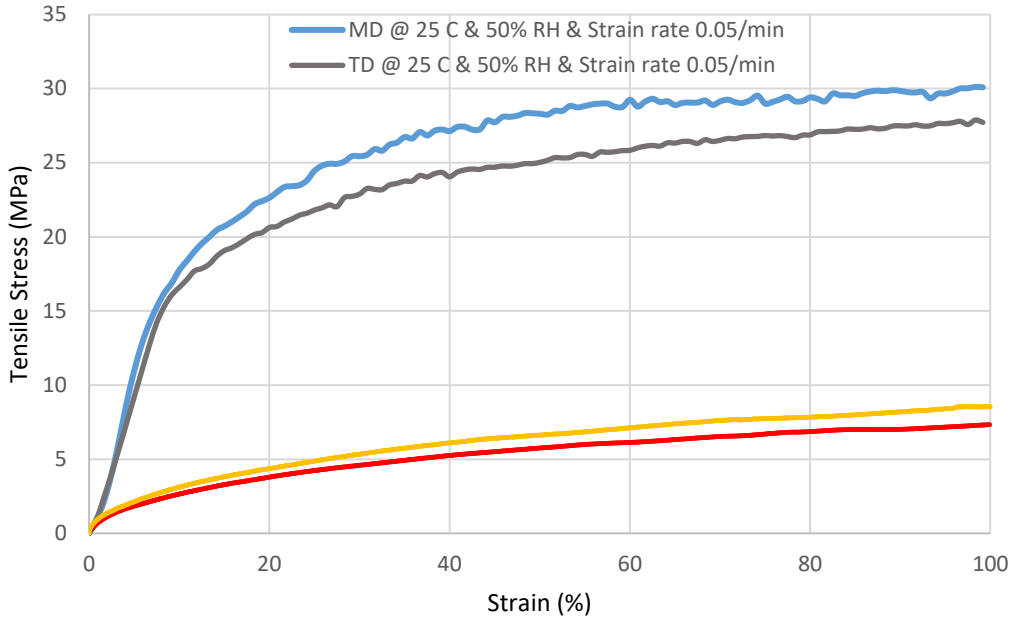

Figure 24 **Tensile tests in both MD and TD directions in order to check the reinforced membrane's isotropicity, 25 °C, 50% RH, and strain rate 0.05/min – 80 °C, 90% RH, and strain rate 0.01/min**

4.1.2 FEM modeling based on Ogden and G'Sell-Jonas's theories for the tensile tests

The main purpose of this section is to model the membrane's tensile tests in ex-situ by two methods, one of which is Ogden, which is more accurate but has more material constants and doesn't cover the strain rate effects, while G'Sell-Jonas is more comprehensive while has fewer material constants but is less accurate than Ogden. The Ogden theory considers both elastic and viscoelastic effects in materials. It employs strain energy density functions in its mathematical formulation to describe how the material responds to deformation over time. To accurately characterize the behavior of viscoelastic materials, the model requires determining a set of material parameters through experimental data. The strength of the Ogden theory lies in its capacity to precisely capture the complex characteristics of viscoelastic materials. It can successfully handle nonlinear behavior, anisotropy, and time-dependent responses. This versatility allows the model to be applied to a wide array of materials, ranging from rubber-like substances to biological tissues [116]. The G'Sell-Jonas theory is a constitutive model specifically designed to describe the mechanical behavior of viscoelastic materials, with a particular focus on polymers. The theory incorporates two distinct mechanisms: elastic response and viscous

flow. To represent the material's mechanical response accurately, the model combines a Maxwell-like viscoelastic element in parallel with an elastic element. This model is well-suited for characterizing the behavior of polymers, especially under conditions of high strain rates and elevated temperatures. It takes into account both short-term elastic behavior and long-term viscoelastic relaxation, making it effective in capturing the time-dependent response of these materials [111].

In Figure 25, the finite element model in Abaqus version 2022 (student license) based on Ogden for the tensile test has been compared with the DMA results. The model, like its tensile stress test, is constrained from one side, and strain applies on the other side. Abaqus has Ogden theory as its default option and has an internal optimization core to obtain material constants based on the imported tensile test results.

In Figure 25-a-b, for N= 2 and 3 in equation 30, the material constants for fitting stress calculated based on Ogden to experimental data have been extracted. In Figure 25-c-d, in FEM, normal strain = 0.5 is applied, which is equal to true strain = 0.408, and consequently, the true stress from modeling and the DMA tensile test are 8.167 MPa and 8.06 MPa, respectively, which illustrates a high consistency between Ogden’s modeling and experiment.

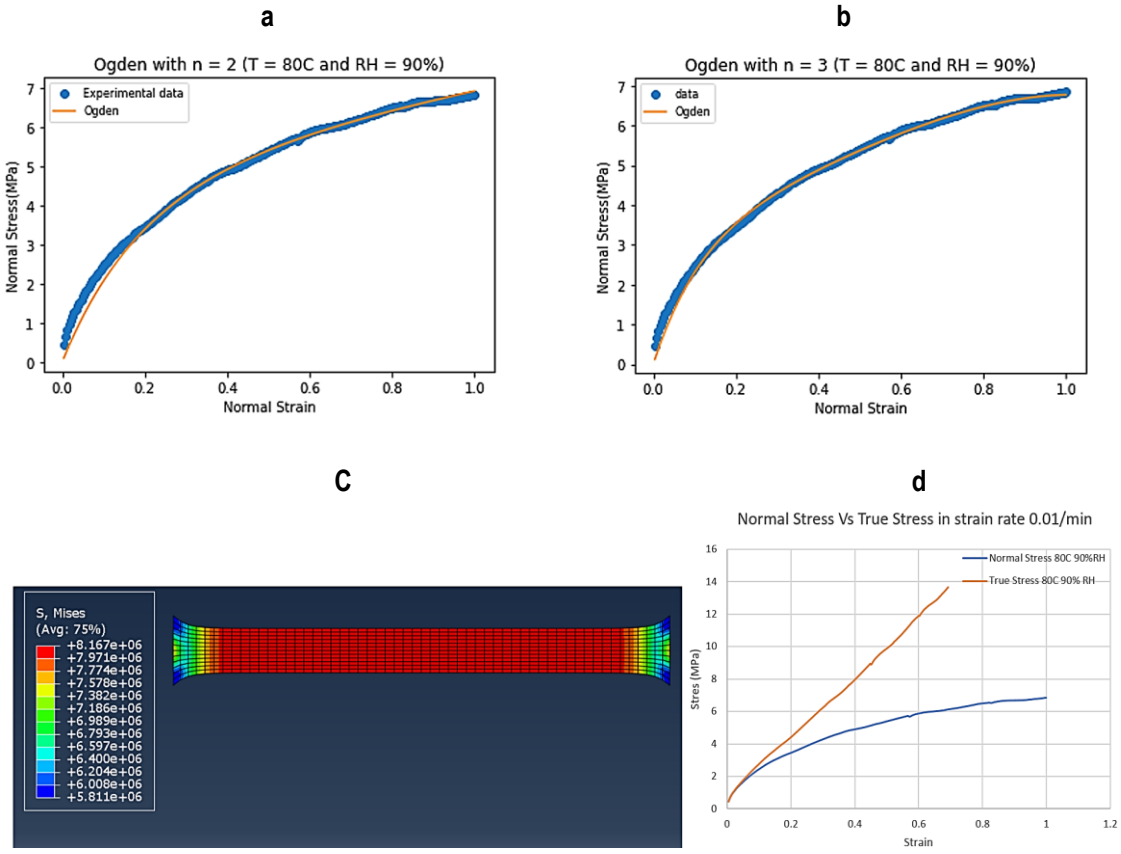

Figure 25 Fitting the Ogden theory model to experimental tensile data

In the main simulation, the optimized material parameters for G'Sell-Jonas's theory based on the DMA tests have been extracted in Python in Figure 26-a, which has a good consistency with tensile stress experimental reports, and then the true stress-strain curve from the FEM model for a rectangular membrane in 80 °C and 90% RH is illustrated in Figure 26-b, which is completely consistent with the same FEM conditions based on Ogden in Figure 25-c-d. The stress distribution for both rectangular and dogbone shapes based on the G'Sell-Jonas has been displayed in Figure 27. This demonstrates that when the membrane assumes a rectangular configuration, stress distribution is even throughout. However, when it takes on a dogbone shape, stress concentration occurs primarily at the corners due to significant variations in intersection areas, which can be approximately twice as large as the middle section of the dogbone shape.

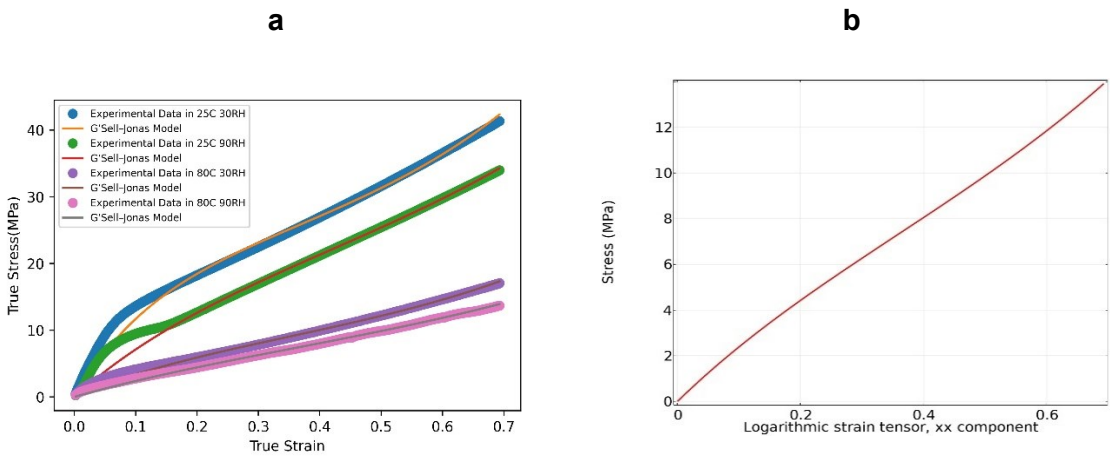

Figure 26 **a) Experimental data (strain rate 0.01) and fitting graphs in Python for optimized material parameters. b) Modeling result for 80 °C and 90% RH based on G'Sell-Jonas theory**

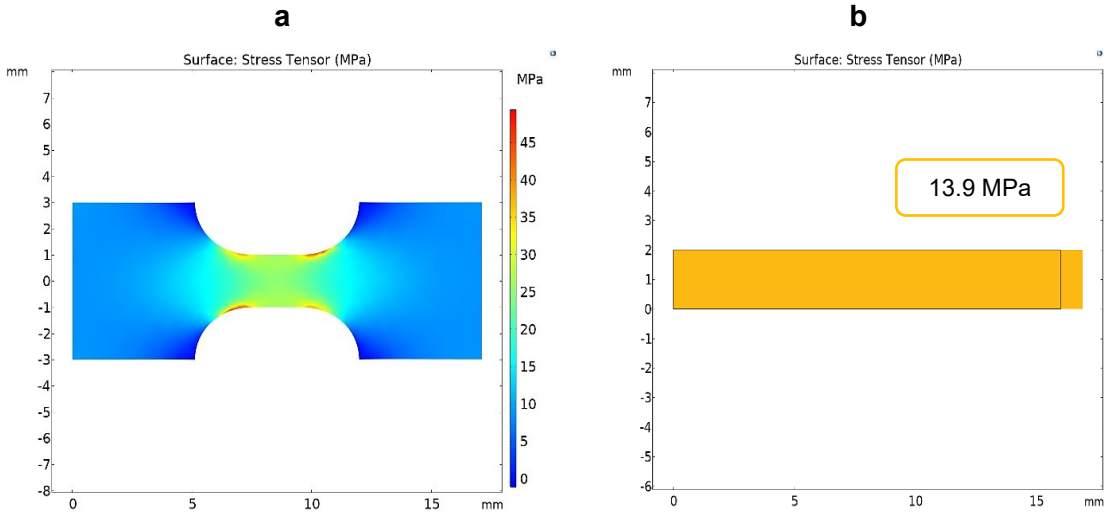

Figure 27 **Simulated stress distribution in tensile test at 80 °C and 90% RH in a) dogbone and b) rectangular shaped sample models.**

Material fittings for the developed G'Sell-Jonas from equations 13 to 17 have been brought into Table 5. A Python library called SciPy optimize has been utilized in the stage of optimizing these material parameters to fit the developed G'Sell-Jonas in equation 13 to the experimental data from tensile stress tests. First, the experimental data was divided into two groups: 25–50 °C and 50–80 °C. For instance, for 50–80 °C, a batch of material parameters for (50 °C, 50% RH) was extracted first, followed by a batch of material parameters for (80 °C, 30% RH) and (80 °C, 90% RH), and finally, a batch of material parameters that could fit on all graphs was extracted between these two material

parameter domains. This process is repeated for 25–50 °C, and optimized material parameters in this temperature domain are obtained.

Table 5 Material parameters in developed G'Sell-Jonas in equation 13 and Young's modulus in equation 11

50 - 80 °C	k_0(MPa)	α(1/K)	β	w_0	w_1	h_0
	5	-0.003	0.002	4.398	0.006	1.318
	h_1	c	d			
	-0.005	0.0021	0.033			
25 - 50 °C	k_0(MPa)	α(1/K)	β	w_0	w_1	h_0
	19	-0.0010	0.006	8.16	0.007	1.377
	h_1	c	d			
	-0.005	0.005	-0.0990			
25 - 80 °C	A_1(1/C)	B_1(1/C)	A_2(1/C)	B_2(1/C)		
	0.0005	-0.08	-0.0210	6.064		

The developed G'Sell-Jonas model provides a good fit for both cases (25-50 °C and 50-80 °C), with the fitting curves accurately matching the experimental results for long strains. For small strains (stress less than 1 MPa), the membrane's mechanical behavior follows a linear elastic model (equation 18).

Figure 26- a is just for tensile stress, while in real fuel cell operations, membranes should endure compressive stresses too, and therefore, we proposed the generalized G'Sell-Jonas in equation 28. The generalized G'Sell-Jonas approach was utilized to extract fitting curves (depicted in Figure 28) for both tensile and compressive stresses. The extracted curves were found to have acceptable compliance with the experimental results, particularly at elevated temperature and humidity levels that are more relevant to a wider range of fuel cell operational conditions.

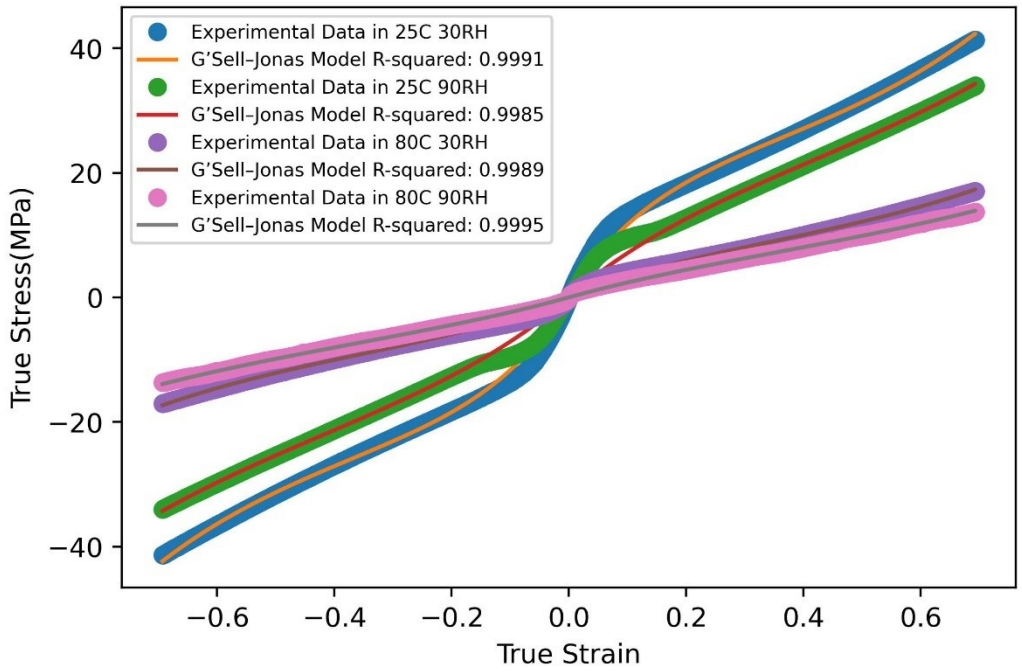

Figure 28 The fitting graphs based on generalized Sell-Jonas on the experimental data at a strain rate of 1%

It is worth mentioning that in all FEM models in this study, one equivalent layer for all three layers (PFSA- ePTFE- PFSA) has been taken into account in order to illustrate the entire mechanical behavior of the reinforced membrane rather than considering a separate model for each layer.

4.1.3 Fatigue tests results

In this section, the results for both ex-situ fatigue tests that have been implemented in DMA and in-situ fatigue tests based on the ΔP-AMST method are presented.

The investigation of the membrane fatigue behavior in ex-situ involved the application of a wide range of loads with a stress ratio of 0.2 in all combinations of 80 °C and 60 °C with 90% RH and 30% RH on the membrane. This scope of testing was chosen to closely resemble the conditions of the ΔP-AMST tests and real fuel cell operations, making comparisons more reasonable. Figure 29 displays the S-N curve obtained from the DMA fatigue tests and shows that its trend for every environmental condition is similar to that of Khorasany's work for nonreinforced membranes [121]. Figure 29 demonstrates that the membrane's fatigue durability increases in a min-to-max manner with the order

being (80 °C, 90% RH), (60 °C, 90% RH), (80 °C, 30% RH), and (60 °C, 30% RH) for modified amplitude stresses below 3.8 MPa. The results show that the impact of humidity on membrane fatigue durability, particularly at higher humidity levels, is more significant in the DMA fatigue tests than in the DMA tensile tests (Figure 23). For higher modified amplitude stresses than 4.33 MPa, (80 °C, 90% RH) exhibited a higher fatigue lifetime compared to (60 °C, 90% RH) and (80 °C, 30% RH) but less fatigue lifetime than (60 °C, 30% RH). In Figure 29, every test has been repeated several times and the average has been presented, and it is worth mentioning that for every test, the maximum deviation from the average is less than 15%. All data points on the curves were acquired at a frequency of 10 Hz, which corresponds to the mechanical loading frequency used in DMA. However, the individual diamond markers represent tests conducted at 5 Hz. We conducted mechanical loading at 5 Hz across three different ambient conditions, each with a distinct modified amplitude stress level, in order to gain an overall understanding of the frequency's impact on the membrane's DMA fatigue lifetimes. Consistently, for all three tests with mechanical loading at 5 Hz, the fatigue lifetime has increased several times. However, in in-situ tests, it was observed in [28, 88] that by decreasing RH frequency, the fatigue lifetime also decreased. This occurred because at lower frequencies, the membrane in in-situ conditions is exposed to dryness for longer periods.

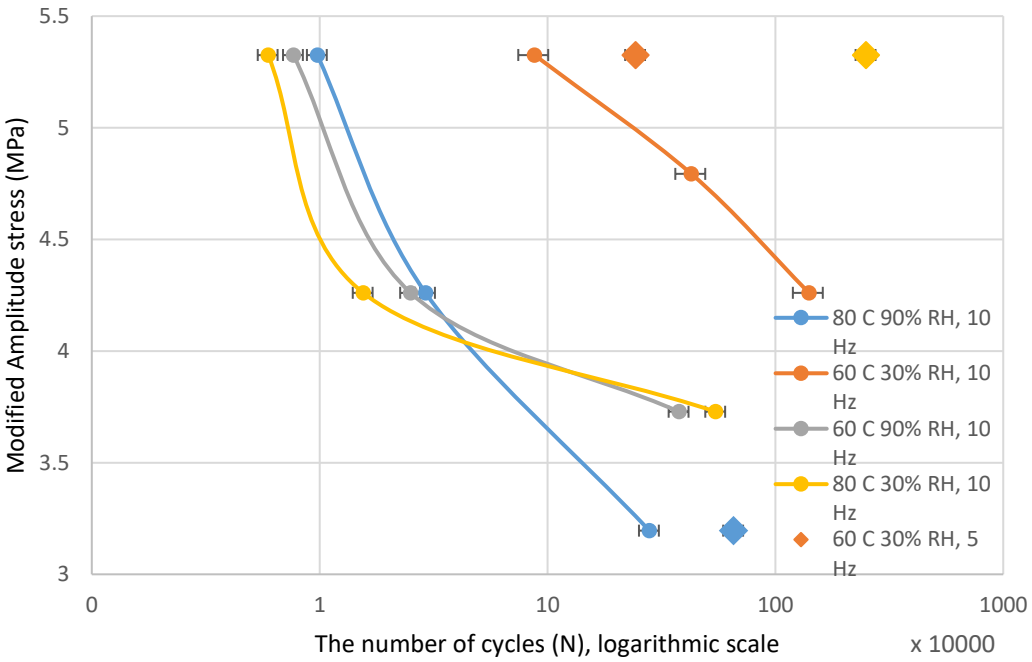

Figure 29 **S-N curve for fatigue DMA for four conditions and different amplitudes of stress**

4.1.4 FEM Modeling of the DMA fatigue tests based on G'Sell-Jonas theory

In this section, the above ex-situ fatigue tests in DMA have been modeled by the developed G'Sell-Jonas theory with its extracted material constants shown in Table 4 for the fatigue results in Figure 29. The developed GSell-Jonas model was used to calculate the stress in every node of the model and based on the experimental data in Figure 29, the fatigue lifetime was calculated by interpolation or extrapolation. Figure 30 presents the fatigue lifetime distribution model for a single ex-situ condition, where the weakest point in the dogbone-shaped membrane was found to be the contact point between the arc and the thinnest part of the membrane. This point was found to have the highest concentration of stress, making it the most vulnerable to fatigue failure.

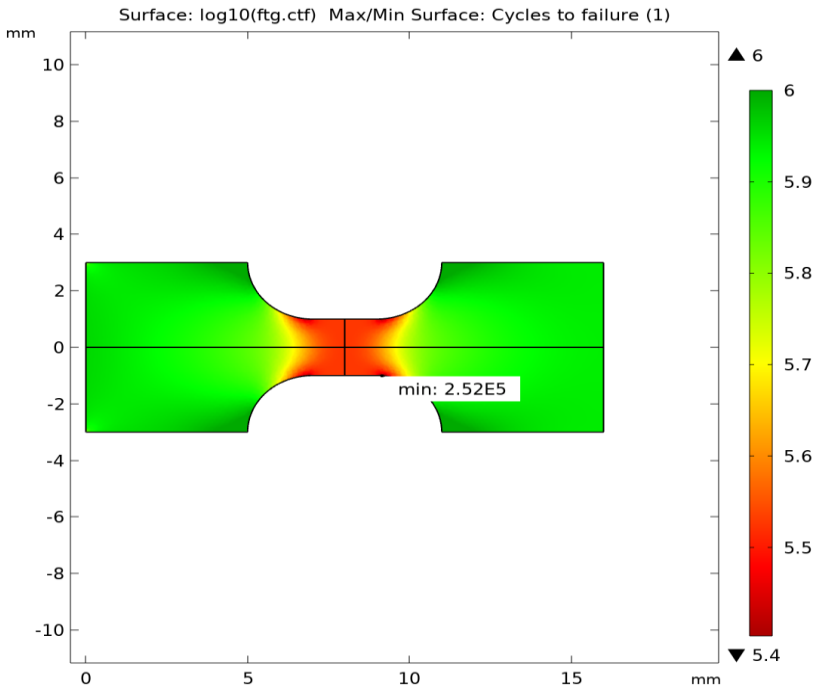

Figure 30 The fatigue lifetime distribution model for 80 °C, 90% RH, Amplitude stress= 3 MPa, and a stress ratio of 0.2 on DMA

In DMA fatigue testing, halving the load frequency has been shown to enhance fatigue lifetimes by three to four times, while decreasing the strain rate is expected to reduce the number of fatigue lifespan cycles in real fuel cell conditions (in-situ) [89, 96]. While the results from DMA tests can be used to compare the fatigue lifetime of different membranes, it is not possible to estimate the fatigue lifetime of a membrane under complete fuel cell conditions based on these results. This may be due to the fact that the membrane experiences triaxial stress in a complete fuel cell and ΔP AMSTs, whereas in a DMA test, the stress applied to the membrane is uniaxial. Another reason for this could be stress relaxation, as in a fatigue DMA test with a lower strain rate, the membrane has more time to release stress and can therefore endure more cycles. However, in a complete fuel cell, the main source of fatigue load is swelling strain, and stress relaxation during the dry phase of every RH cycle is not effective. Furthermore, the strain rate in a fatigue DMA test with a load frequency of 10 Hz is approximately 1500 times faster than the strain rate due to RH cycles in a complete fuel cell when its dry phase is 60 s, like all in-situ tests in this study. Therefore, the behavior of the membrane can be different at such large differences in strain rates.

4.2 In-situ approach

4.2.1 ΔP-AMST results

In this section, the results for the ΔP-AMST tests and how these results are used to derive the S-N curve of the reinforced membrane have been elaborated. The extracted S-N curve is used in FEM modeling of the ΔP-AMST test in the next section.

The tests involved subjecting the membrane to humidity cycles with varying pressure differentials and temperatures for 60 seconds of dry phase and 30 seconds of wet phase. In each test, the temperature and ΔP remained constant while the humidity cycles were applied. In the first series of tests, the temperature was set at 90 °C, with RH ranging from 30% to 100% and ΔP varying from 3 kPa to 23 kPa for each fatigue test. In the second series of tests, the temperature was set at 60 °C, and the same RH cycles were used, with ΔP varying from 3 kPa to 27 kPa. If the ΔP was greater than 23 kPa, sudden bursts occurred, while if it was less than 3 kPa, it took over a week and 12 N_2 cylinders were depleted before the test could be completed. Figure 31 and Figure 32 display the results of some of the tests, including different differential pressures for 90 °C and 60 °C. Monitoring pressure fluctuations on the anode side is a reliable method of detecting membrane failure because the pressure on the anode side suddenly increases due to the created hole in the membrane during fatigue fracture, and the pressure differential (blue graphs in Figure 31 and Figure 32) drops. In both Figure 31 and Figure 32, each subfigure provides information on the applied ΔP on the membrane and the corresponding number of fatigue lifetimes based on the completed RH cycles. The red rectangles in Figure 31 and Figure 32 show the threshold of crack propagation because during crack initiation, an enormous pressure differential drop does not occur until that crack propagates through the plane and connects the anode to the cathode side. At that time, a big drop in pressure occurs. In Figure 31, when examining ΔP-AMST at 60 °C, it becomes evident that as the applied ΔP increases, the membrane's ability to endure RH cycles decreases, resulting in more abrupt failures. Nevertheless, across all tests, there is a noticeable sharp decrease in ΔP near the point of fatigue failure. In Figure 32, which pertains to ΔP-AMST at 90 °C, a similar trend is observed. With increasing ΔP, the membrane's endurance of RH cycles diminishes. Notably, in cases of lower ΔP, there is a gradual decline in ΔP near the time of fatigue failure, as indicated in Figure 32-a, -b, and -c. Consequently, at higher temperatures and lower ΔP conditions, there appears to be a

heightened likelihood of multiple crack initiations, resulting in smaller holes due to crack propagation. This phenomenon can be explained by the fact that materials tend to be more brittle at lower temperatures, making sudden fatigue fractures more probable compared to higher temperatures where materials exhibit greater ductility [124].

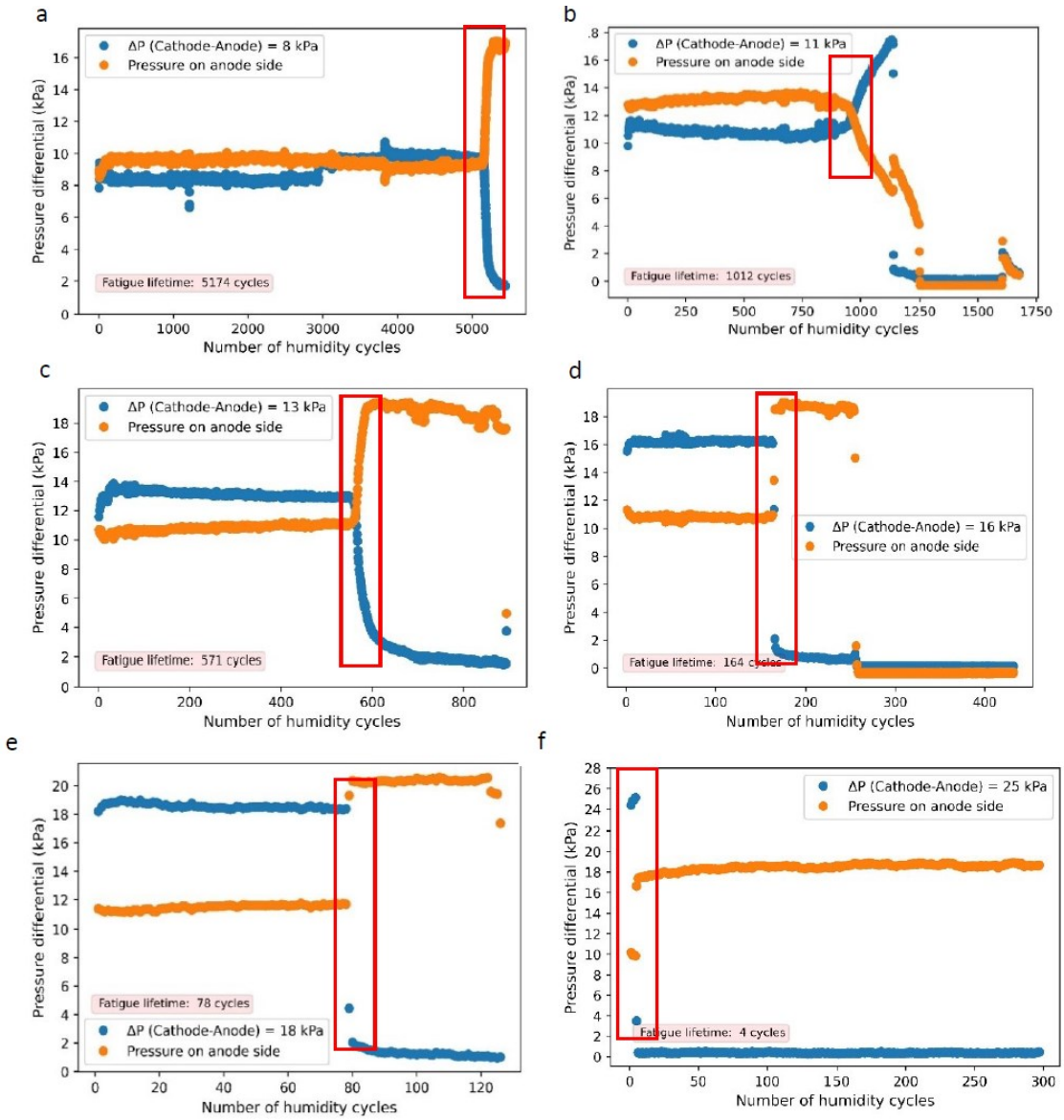

Figure 31 **Pressure-differential accelerated mechanical tests at 60 °C and 30-100% RH, the red rectangle on the graphs shows the approximate threshold of the fatigue fractures.**

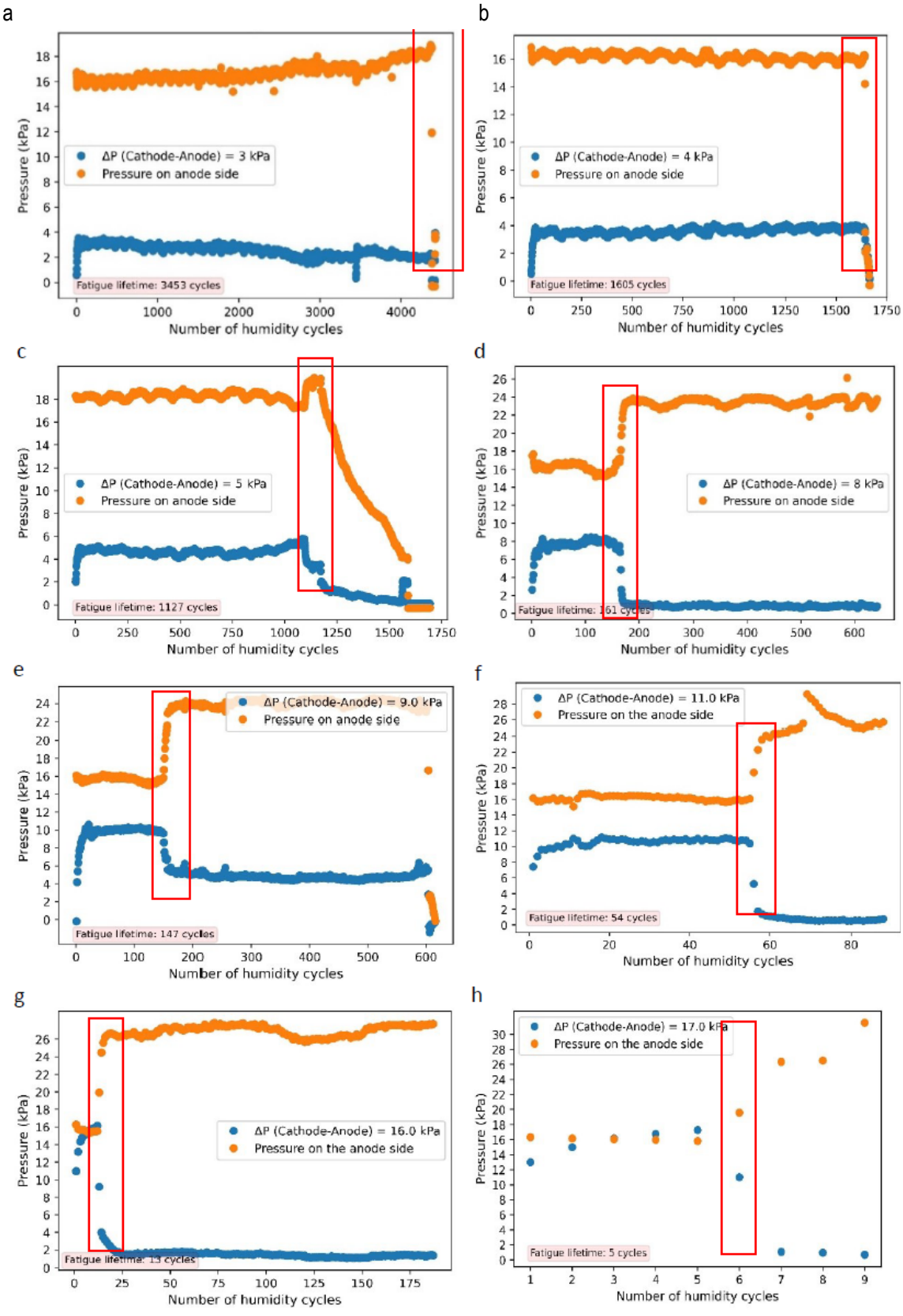
a
Pressure (kPa)
ΔP (Cathode-Anode) = 3 kPa
Pressure on anode side
Fatigue lifetime: 3453 cycles
Number of humidity cycles
b
Pressure (kPa)
ΔP (Cathode-Anode) = 4 kPa
Pressure on anode side
Fatigue lifetime: 1605 cycles
Number of humidity cycles
c
Pressure (kPa)
ΔP (Cathode-Anode) = 5 kPa
Pressure on anode side
Fatigue lifetime: 1127 cycles
Number of humidity cycles
d
Pressure (kPa)
ΔP (Cathode-Anode) = 8 kPa
Pressure on anode side
Fatigue lifetime: 161 cycles
Number of humidity cycles
e
Pressure (kPa)
ΔP (Cathode-Anode) = 9.0 kPa
Pressure on anode side
Fatigue lifetime: 147 cycles
Number of humidity cycles
f
Pressure (kPa)
ΔP (Cathode-Anode) = 11.0 kPa
Pressure on the anode side
Fatigue lifetime: 54 cycles
Number of humidity cycles
g
Pressure (kPa)
ΔP (Cathode-Anode) = 16.0 kPa
Pressure on the anode side
Fatigue lifetime: 13 cycles
Number of humidity cycles
h
Pressure (kPa)
ΔP (Cathode-Anode) = 17.0 kPa
Pressure on the anode side
Fatigue lifetime: 5 cycles
Number of humidity cycles

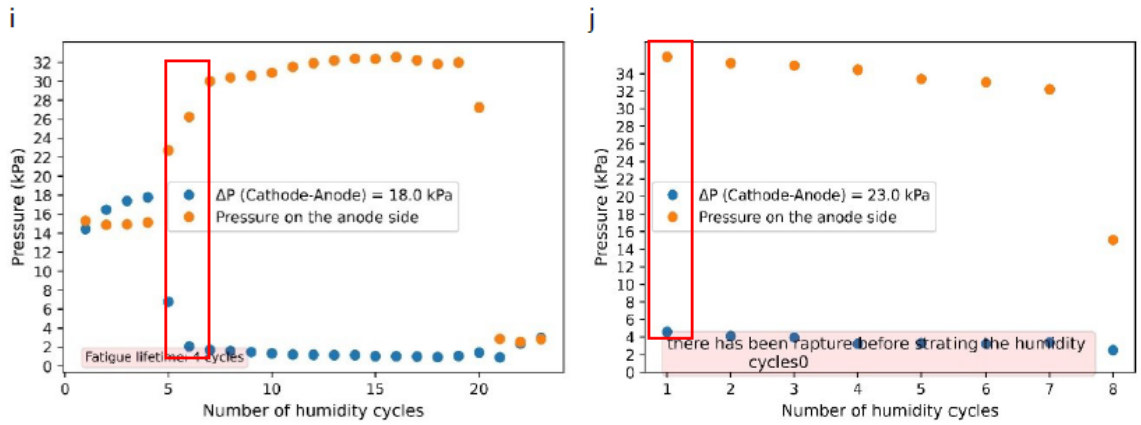

Figure 32 **Pressure-differential accelerated mechanical tests in 90 °C and 30-100% RH, the red rectangle on the graphs shows the approximate threshold of the fatigue fractures**

Figure 31 and Figure 32 show that at 60 °C, membrane is more resilient to fatigue fractures than at 90 °C, and in both of them, after first though-plane crack that led to a little pressure differential drop, the speed of crack propagations becomes higher and membrane fails immediately, which matches Ref [28, 87, 88, 96]. Based on the findings from reference [27], it is observed that after undergoing numerous cycles of relative humidity, the catalyst-coated membrane undergoes a transition from a ductile to a brittle behavior. Additionally, as highlighted in reference [86], when subjected to higher temperatures, the membrane experiences faster in-plane crack propagation. Upon the initiation of in-plane cracks, as described in reference [87], the initial growth of these cracks within the plane occurs relatively slowly. However, as these cracks extend further, their growth rate accelerates. However, as the crack progresses toward the ePTFE reinforcement, the influence of the ePTFE layer becomes increasingly significant. Consequently, the rate of energy dissipation through plastic deformation decreases, requiring more cycles to reach a critical threshold. Once the crack passes through the ePTFE layer, its propagation becomes considerably faster until it reaches the opposite side of the membrane's thickness. Reference [87] also underscores the fact that crack initiation is a more time-consuming process compared to crack propagation. In line with the insights from reference [95], it is worth noting that crack initiation is indeed a time-consuming phenomenon when compared to crack propagation. Moreover, crack initiation is influenced by the material's microstructure and cyclic hardening, whereas crack propagation is primarily governed by the stress intensity factor range. In the context of our ΔP-AMST tests, when operating at lower ΔP levels, the membrane undergoes a transition

from a ductile to a brittle behavior due to prolonged exposure to RH cycles. In a brittle state, multiple crack initiation points emerge, as brittle materials are more sensitive to stress concentrations resulting from any lack of uniformity. Conversely, in ductile materials, localized deformation or yielding occurs, reducing stress concentration. Consequently, the presence of multiple crack initiation points leads to a gradual drop in pressure as these cracks propagate and reach the opposite side of the membrane's thickness (Figure 32-a-b-c). In contrast, at higher ΔP levels, the membrane remains in a ductile state, and a single crack propagates through the plane. Due to the higher stress intensity associated with these higher ΔP conditions, a larger crack forms, resulting in a more sudden and pronounced drop in ΔP when it eventually reaches the opposite side of the membrane's thickness (Figure 32-d-e-f-g-h-i-j). According to the data presented in Figure 31, it appears that the occurrence of multi-crack propagation is less evident at 60 °C. This could be attributed to the substantial difference in the magnitude of ΔP, even in the first test with the lowest ΔP value of 8 kPa, when compared to the lowest ΔP value of 3 kPa in the 90 °C tests shown in Figure 32. As a result, it is plausible to suggest that fatigue failure in the 60 °C tests is likely caused by a single, relatively large crack, rather than the formation of multiple cracks.

Figure 33 illustrates the S-N and ΔP-N curves for both test series (90 °C and 60 °C). The stresses obtained from the FEM model presented in the next section are based on the G'Sell-Jonas method developed in this study for the reinforced membrane. It is worth mentioning that the stress in Figure 33 is the maximum stress in the center of the bulge in every ΔP during the dry phase, when tensile stress would be at its maximum. Because ΔP-AMST tests are time-consuming to repeat all of them several times, just some of them were repeated several times to check the uncertainty of this test, and all of them were around 15% deviated from their averages. In Figure 33, it is evident that membranes exhibit greater resistance to fatigue at lower temperatures when subjected to identical pressure differentials. Additionally, whether at 90 °C or 60 °C, an increase in ΔP leads to higher equivalent stress levels used in modeling, resulting in a shorter fatigue lifetime. When plotting fatigue lifetime cycles on a logarithmic scale, both Stress-N and ΔP-N relationships appear to be approximately linear. Therefore, for other ΔP, easily by linear interpolation or extrapolation, the number of RH cycles in ΔP-AMST that our reinforced membrane will fail, can be predicted.

When the ΔP was set to 3 kPa, the sample took about 6 days (approximately 3500 cycles) to fail, and multiple small holes were created on the membrane, as shown in Figure 34, instead of a single hole as observed in previous tests. This suggests that for low-stress distributions, micro-cracks are initiated and propagate from multiple locations near the center of the circle, resulting in simultaneous failures. At low-pressure differentials, the rate of crack initiation is higher than the rate of crack propagation, whereas the opposite is true at high pressure.

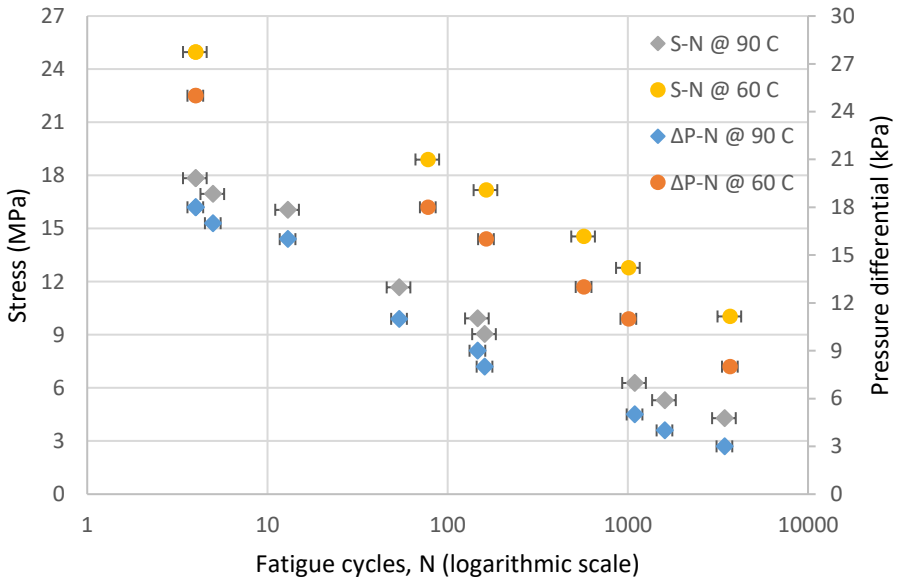

Figure 33 S-N curve for 90 °C and 60 °C and 30-100% RH

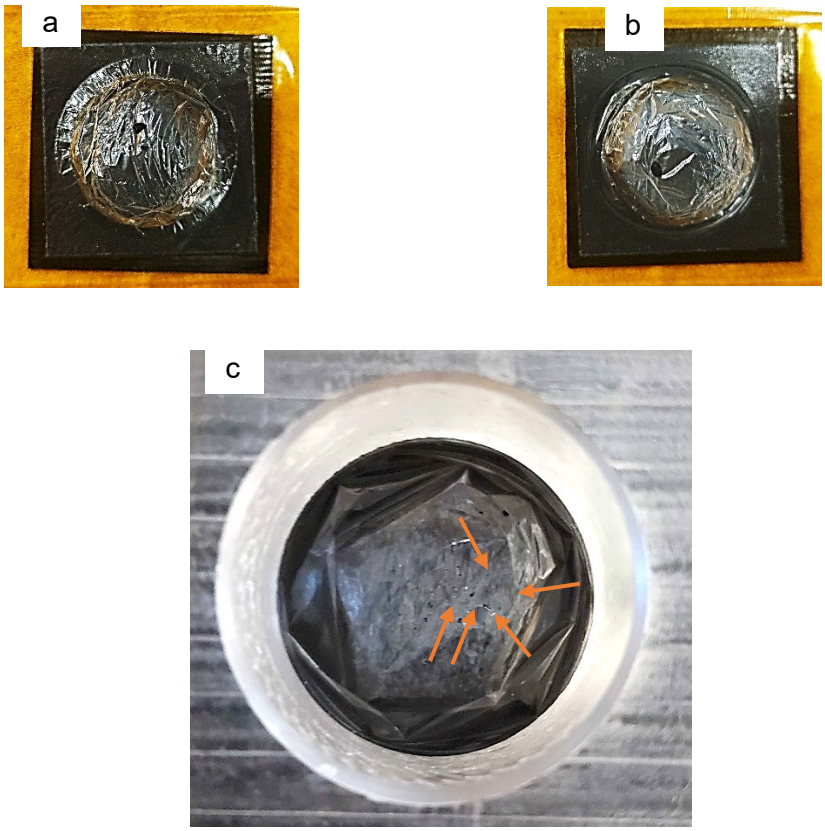

Figure 34 a) The failed membrane for ΔP = 7 kPa, b) ΔP = 12 kPa, c) ΔP = 3 kPa

Based on equation 35 and the S-N curves in Figure 34 and by considering the dry phase duration, for every ΔP in our ΔP-AMST tests, the accumulated plastic dissipation energy has been calculated, and its trend for both 60 °C and 90 °C has been shown in Figure 35. Because the trend of plastic dissipation energy in low ΔP is highly non-linear, predicting fatigue lifetime based on these graphs and their governing equation for ΔP=0, which is similar to a membrane in real conditions, is not reasonable.

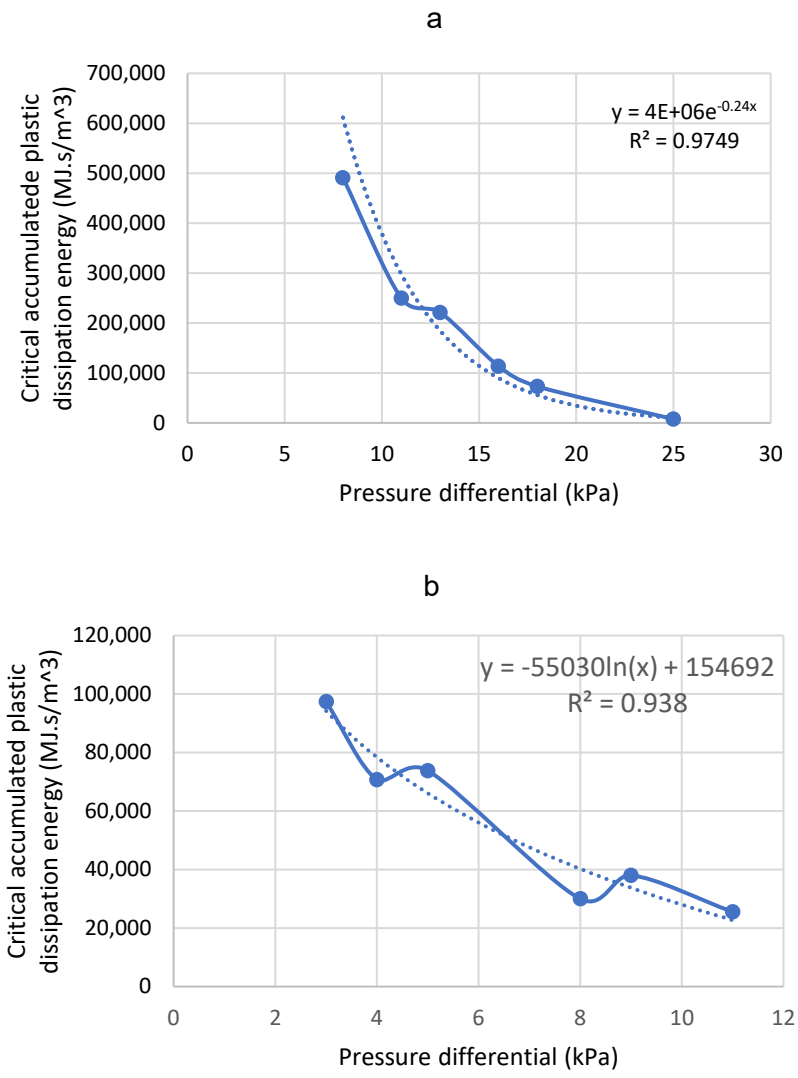

Figure 35 How the CAPDE changes with different ΔPs, a) for 60 °C and b) for 90 °C

The overall trend for both 60 °C and 90 °C can be seen in Figure 34, which demonstrates that when ΔP is reduced, the CAPDE that results in membrane breakdown is growing. This illustrates that a membrane can withstand more humidity cycles before fatigue failure when it experiences lower static stress, which in this case is ΔP. Moreover, when considering the overall trends observed in Figure 34-a-b, it becomes evident that the CAPDEs at 60 °C are consistently five times greater than those at 90 °C. Consequently, it can be inferred that membranes exhibit enhanced resistance to fatigue at lower temperatures, even when subjected to higher pressure differentials. To illustrate, take the example of a membrane exposed to ΔP = 8 kPa at 60 °C; it can endure stress

that is 170% greater than when ΔP = 3 kPa at 90 °C, as indicated by the S-N curves in Figure 33. Remarkably, despite this significant difference in stress, their fatigue lifetimes remain relatively similar, primarily due to the lower temperature, which is 30 °C or 30% less in the first case. This underscores the fact that temperature has a more pronounced effect on a membrane's fatigue life compared to variations in stress magnitude.

4.2.2 FEM modeling of the pressure-differential accelerated mechanical stress test (ΔP-AMST)

The primary objective of ΔP-AMST is to expedite the mechanical fatigue of the membrane under in-situ conditions. By utilizing FEM modeling, the stress distribution in the membrane can be calculated and verified. Therefore, the fatigue lifetime of the membrane can be predicted under different ambient conditions, such as various humidity cycles, temperatures, and pressure differentials. Furthermore, the S-N curve extracted from this modeling can be employed for the fatigue evaluation of an entire cell under actual conditions. For FEM simulation, 3D tetrahedral membrane elements suitable for meshing, which can't endure bending and compressive stress, have been selected in COMSOL 5.6. The meshes are so small (110798 elements) and the time step is 1 s that the results achieve convergence. In Figure 36, for ΔP = 5 kPa mechs are refining in every model, and for the center of the bulge, all mech sizes show consistent results. Here, we have modeled only the membrane, following the developed G'Sell-Jonas model. Other components, such as GDL and frames, have not been modeled because they don't have any effects on FEM results; their functions are considered only in experiments.

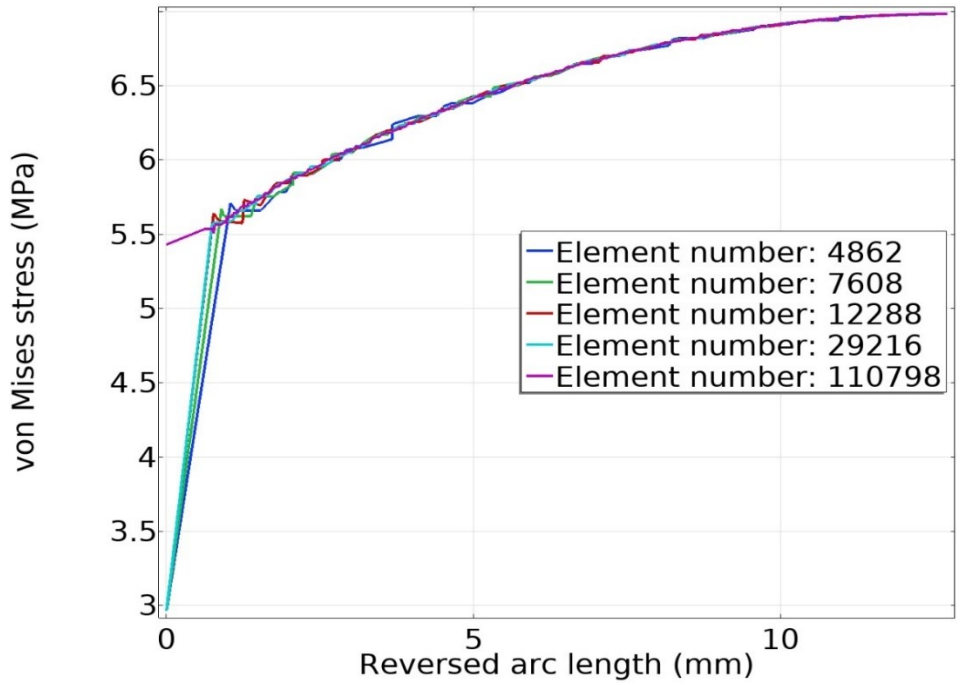

Figure 36 Mesh independency study for ΔP = 5 kPa, T= 90 °C in ΔP-AMST modeling, "Reversed arc length" is from the circumference of the bulge to the center of the bulge

Figure 37 depicts the operational parameters used in the ΔP-AMST modeling, following the G'Sell-Jonas method. These parameters include a ΔP = 4 kPa, T = 90 °C, and sinusoidal RH cycles ranging from 30% to 100%. The timeline illustrated in Figure 37 indicates that from 0 to 90 seconds, the membrane undergoes a transition from its initial state to the designated operational conditions. Subsequently, with ΔP and temperature held constant, the membrane is subjected to the RH cycles. Figure 37-dspecifically presents the changes in swelling strain, both in-plane and through-plane, resulting from these RH cycles. This data helps to understand how the membrane's dimensional changes are influenced by fluctuations in relative humidity over time. As has been displayed in Figure 38, the membrane has been constrained in all directions except the area under the hole in the spacer (Figure 18) and the ΔP has been applied to the membrane.

Although a 2.5% deviation in temperature and a 5% deviation in pressure were observed after the initiation of cycles (90 s) in ΔP-AMST tests in Figure 31 and Figure 32, these fluctuations were ignored since they were random and within their respective

tolerance domains. It should be noted that the membrane elements in this FEM modeling do not have any bending stiffness, which is reflective of its actual properties.

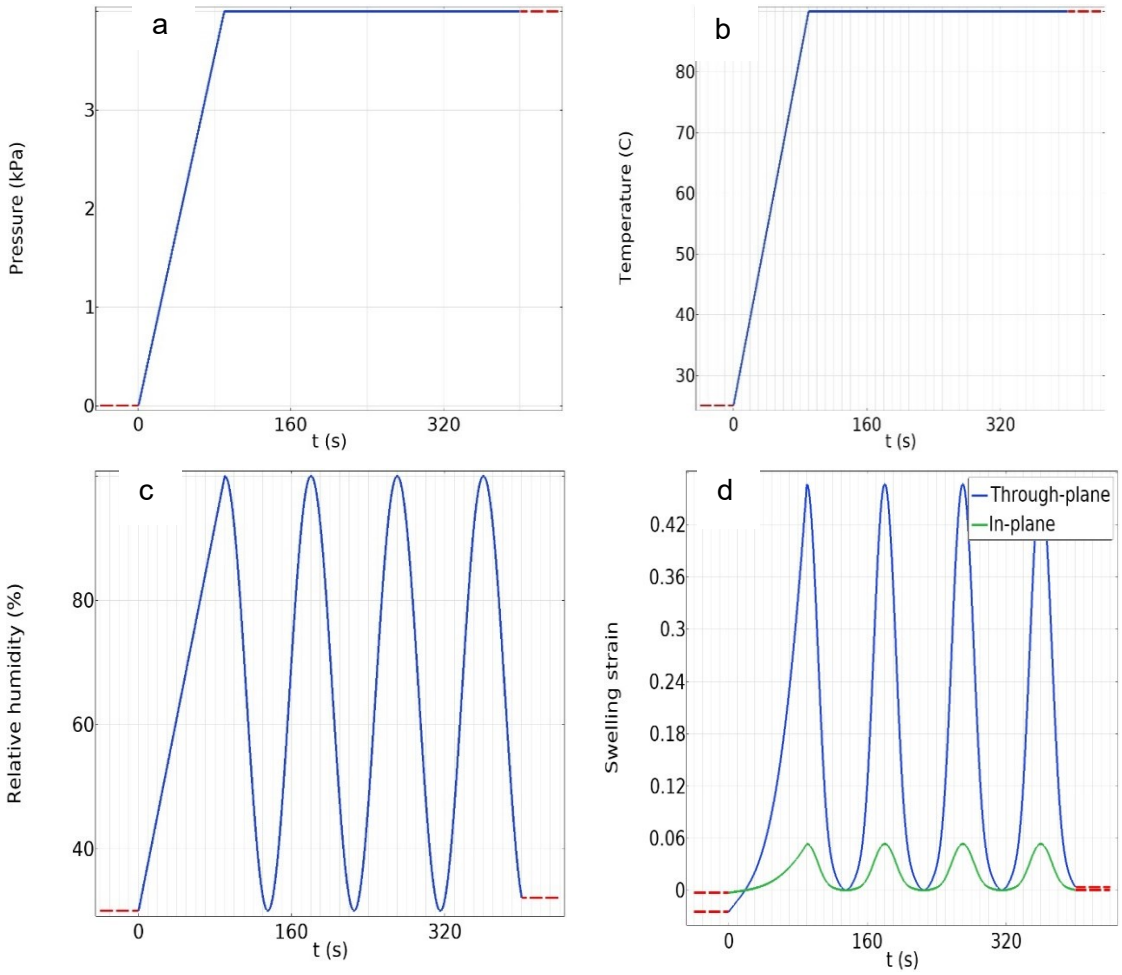

Figure 37 The applied ambient time-dependent conditions in the tests at 90 °C, 30-100 % RH, ΔP=4 kPa, cycles starting from 90 s, a) pressure differential, b) temperature, c) humidity cycles, d) swelling strain in both in-plane and in-thickness (through plane)

The boundary conditions, the stress distribution and fatigue lifetime based on the extracted S-N curve for 90 °C and 30-100% RH cycles are presented in Figure 38. The stress distribution was calculated using the G'Sell-Jonas method, and the fatigue lifetime was predicted using the S-N curves in Figure 33 by interpolation or extrapolation.

a

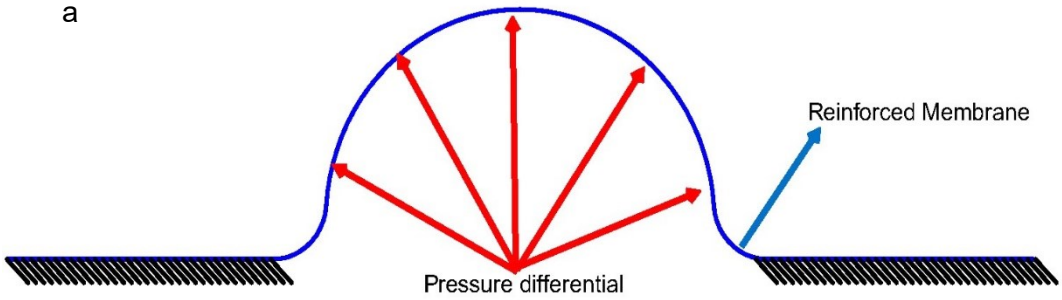
Reinforced Membrane
Pressure differential

b

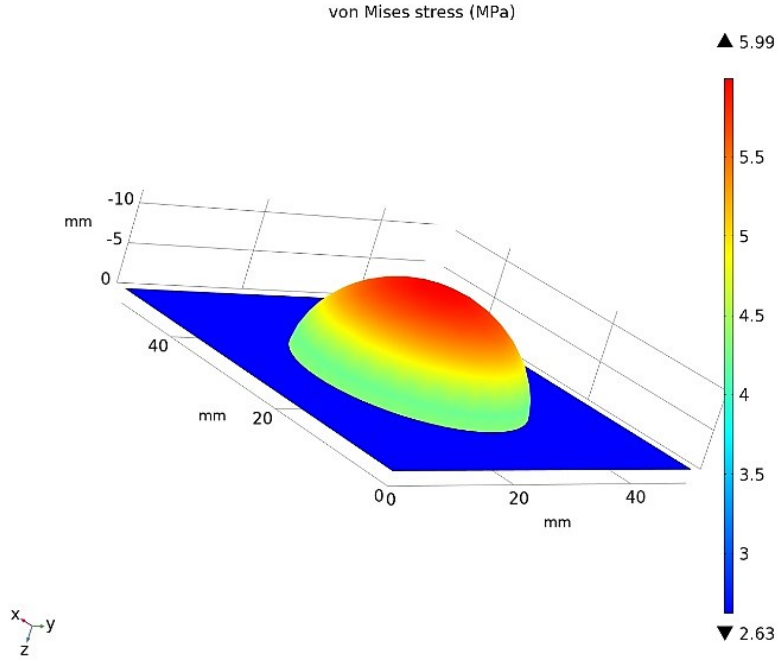
von Mises stress (MPa)
▲ 5.99
5.5
5
4.5
4
3.5
3
▼ 2.63
-10
mm
-5
0
40
mm
20
0
0
20
40
mm
x
y
z

c

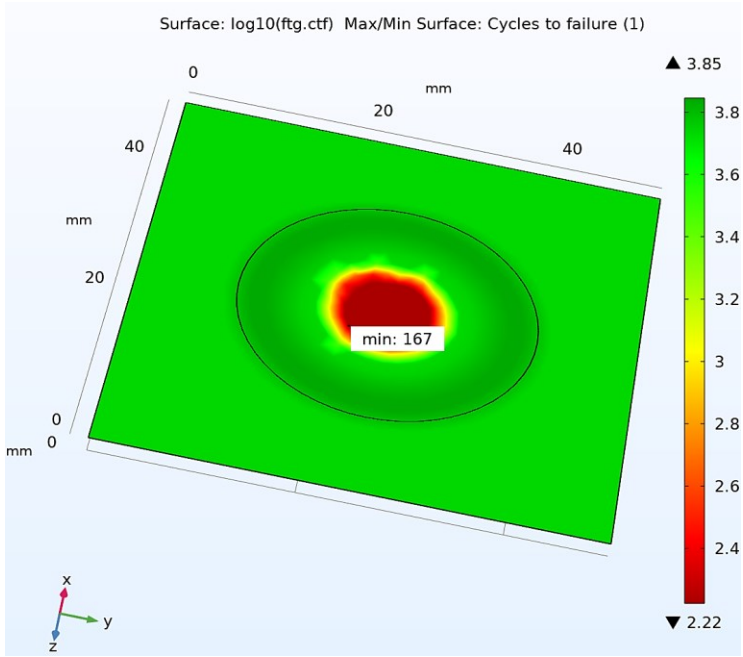
Surface: log10(ftg.ctf) Max/Min Surface: Cycles to failure (1)
▲ 3.85
3.8
3.6
3.4
3.2
3
2.8
2.6
2.4
▼ 2.22
0
mm
20
40
40
mm
20
0
mm
0
min: 167
x
y
z

Figure 38 **a) Boundary conditions, b) Triaxial Stress distribution (von Mises) based on the developed G'Sell-Jonas model with ΔP=8 kPa at 100% RH, c) logarithmic fatigue lifetime distribution with ΔP=8 kPa, both are at 90 °C**

Based on Figure 38, the maximum stress is in the center of the bulge because the membrane has been modeled with membrane elements and can't endure any bending stress, and therefore the maximum stretch and membrane thinning happen at this point, and hence the maximum plastic dissipation energy based on equation 35 should occur at this point, which is confirmed in Figure 39 and its distribution is like the stress distribution in Figure 38-a.

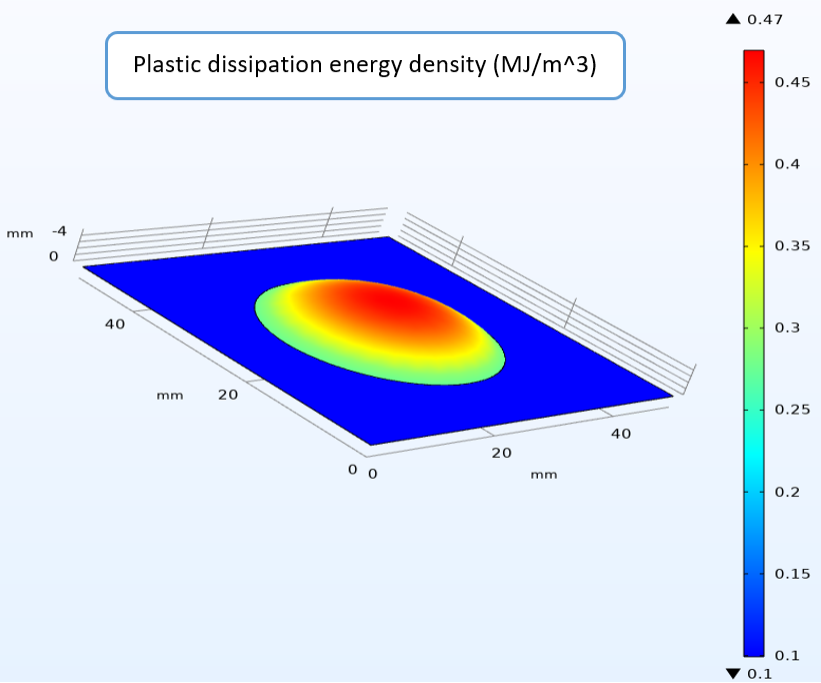

Figure 39 **Plastic dissipation energy (MJ/m^3) in one RH cycle in the driest time (135 s), 90 °C, ΔP= 4 kPa**

Figure 40 has been presented to illustrate how stress varies throughout the course of a full humidity cycle at the center of the bulge. It highlights that the highest stress occurs during the dry phase. This is because, during the dry phase, the vector of the in-plane stress due to dryness on the membrane is tensile, like the in-plane stress caused by ΔP. In contrast, during the wet phase, the vector of the in-plane stress on the membrane due to wetness is compressive and opposite to the in-plane stress caused by ΔP. In Figure 40 that is for three first RH cycles, the same ΔP has been applied to the membrane at both

60 °C and 90 °C while humidity varies, similar to Figure 37-c, which illustrates that both endure the same stress but different strains during the driest time, 135 s. As shown in Figure 23-a, which was taken from the tensile tests, the membrane experiences an in-plane strain that is twice as great at 90 °C as it is at 60 °C. Here, the membrane is under stress in two directions, whereas in the tensile tests, stress only applies in one direction, so it is reasonable that the amount of stress in ΔP-AMST modeling is greater for both temperatures. In Figure 40, it is evident that at both temperatures, the membrane experiences plastic deformation due to the generated stress resulting from applied ΔP and RH cycles. Consequently, the strain at the center of the bulge increases sharply until it reaches the maximum stress level during the driest phase. Afterward, the strain continues to increase, but gradually. Because RH cycle effects have been simulated with swelling strains that are the same for every RH cycle and the impact of creep due to ΔP has been neglected, the stress curve is equal for every cycle, and the strain curve also follows a constant pattern after experiencing the first highest stress.

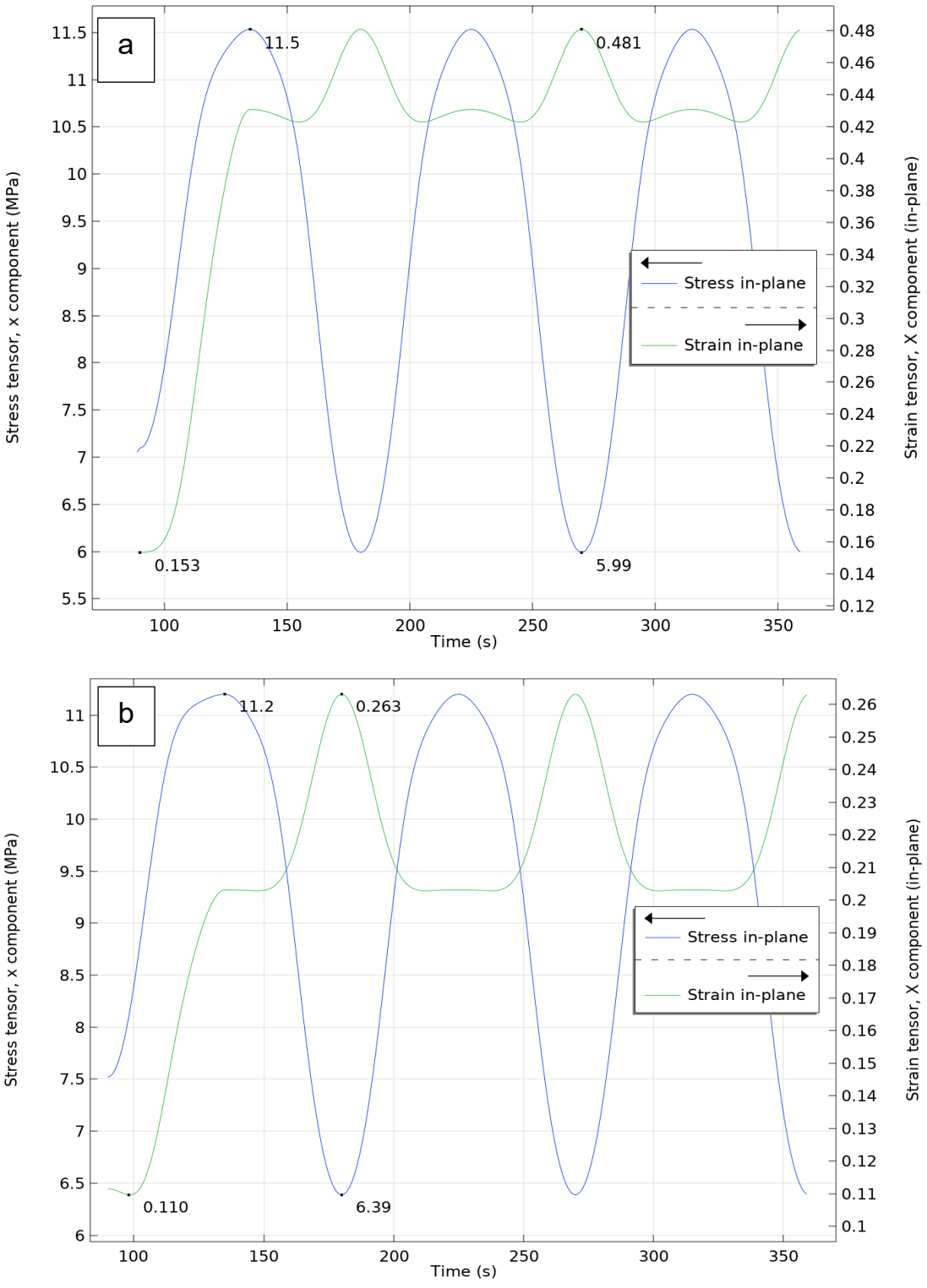

Figure 40 **The stress and the strain in-plane based on the developed G'Sell-Jonas in the center of the bulge occur in a complete humidity cycle of 30–100% RH when ΔP = 8 kPa, RH is 100% in 90 s, RH is 30% in 135 s, and RH becomes 100% again in 180 s. a) 90 °C, b) 60 °C**

To verify the order of our calculated stress based on the model developed with G'Sell-Jonas, the nearest approach was selected that was used in [97]. Hencky's theory (equation 40) [125] is a criterion used to compare the calculated stress on the membrane for different pressure differentials. It states that the maximum normal stress on the membrane can be expressed as:

$$\sigma_r = \sigma_\theta = \frac{B_0}{4}\left(\frac{EP^2a^2}{t^2}\right)^{1/3} \tag{40}$$

where E is Young's modulus, P is the applied ΔP, a is the radius (12.7 mm), t is the membrane thickness, and B_0 is a function of the Poisson's ratio (υ). In Figure 41, for every pressure differential, the stress in the center of the bulge based on the developed G'Sell-Jonas and Hencky equations for both 90 °C and 60 °C in 100% RH has been calculated. For ΔP less than 9 kPa in 90 °C and 13 kPa in 60 °C, the calculated stress based on the developed G'Sell-Jonas and Hencky are less than 3% different, but for higher Ps, this difference is increasing, which can be due to plastic deformations that in G'Sell-Jonas are exponentially dependent on strain while in Hencky are approximately linear. In real fuel cell operation, ΔP is usually near zero, and so our calculated stress method is verified completely with Hencky's approach too.

However, it is worth noting that while Hencky's theory is a useful criterion, it does not take into account important factors such as the effects of humidity, temperature, and strain rate. Therefore, the G'Sell-Jonas model, which considers these factors, is more acceptable for predicting the stress distribution in the membrane. After analyzing the membrane thinning using the finite element model around the bulge center, it was found that the thickness decreased from 89% of the original thickness at 3 kPa to 50% at 23 kPa, as shown in Figure 41. Based on Equation 11 and the material parameters in Table 5, the Young's modulus at 90 °C for RH levels of 30% and 100% is 56 MPa and 38 MPa, respectively. According to Hencky's theory (as expressed in Equation 40), where E is in the numerator and t (thickness) is in the denominator, it can be concluded that in the dry phase, where E is larger and t is smaller due to dryness in both in-plane and through-plane directions, the resulting stress in the dry phase will be larger. This confirms that fatigue is more likely to occur in the dry phase rather than the wet phase of RH cycles. Another study [97] measured membrane thinning after passing cycles, which included the

impacts of hygral cycles and stress relaxations, unlike Hencky's stress theory, which does not account for these effects. Therefore, our approach of measuring membrane thinning immediately after pressure differential is more accurate in determining stresses based on Hencky's theory. Comparing these results with the G'Sell-Jonas method provides more rational verification.

a

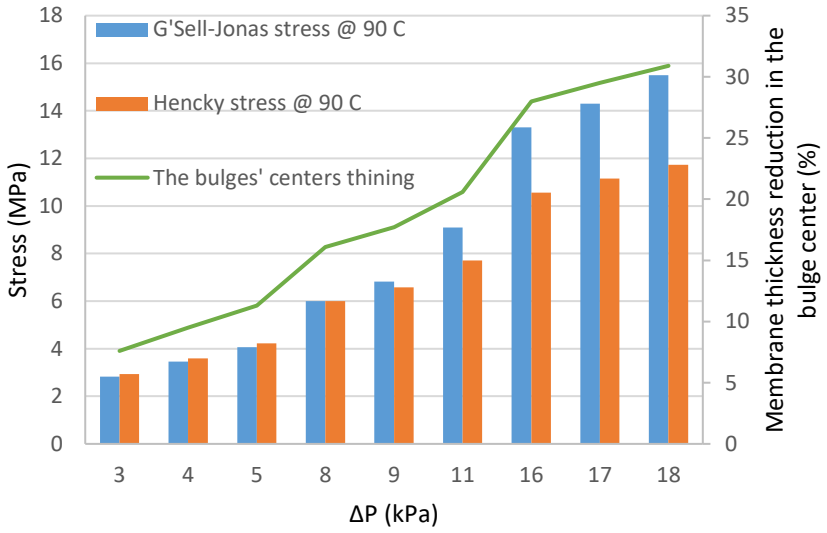

b

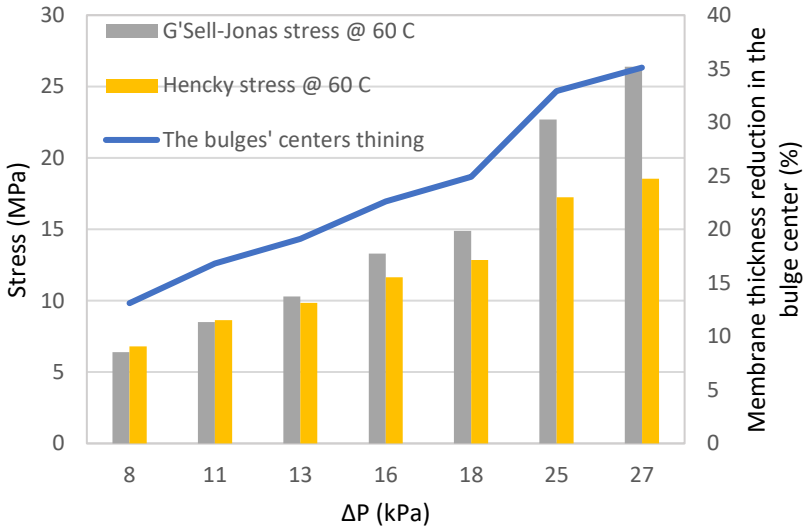

Figure 41 **the developed G'Sell-Jonas vs. Hencky approach at 100% RH in the center of the bulge for a) 90 °C and b) 60 °C**

Based on previous studies in reinforced membrane [89, 96], the swelling ratio through plane in this study is around 8.75 times greater than in plane. In order to investigate the impacts of swelling ratio on maximum stress and plastic dissipation energy, which happen in the center of the bulge, a factor, X, is multiplied in swelling ratio through-plane (z) and a factor $\frac{1}{\sqrt{X}}$ is multiplied in swelling ratio in-plane in both directions (x and y) in order to change swelling ratio through-plane and in-plane while the volume change is constant. The following figures show the effect of swelling ratio in-plane and through-plane on maximum stress and plastic dissipation energy in one cycle during the dry phase (60 s) at different differential pressures, where F is swelling ratio through-plane over swelling ratio in-plane. These graphs demonstrate that when F decreases and we have more isotropically reinforced membrane in the swelling ratio, the in-plane stress, which is the primary cause of crack initiations, will decrease for every applied ΔP. Likewise, the plastic dissipation energy in each cycle will decrease, which can result in a longer fatigue lifetime. Additionally, in higher ΔP, the impact of F on maximum stress is magnified; as a result, this characteristic of the chosen reinforced membrane would be necessary when the pressure differential between the anode side and the cathode side in real fuel cell operation is considerable. By comparing

Figure 43 and Figure 45, the effect of lack of isotropically in swelling ratio for lower temperatures (60 °C) is greater than for 90 °C.

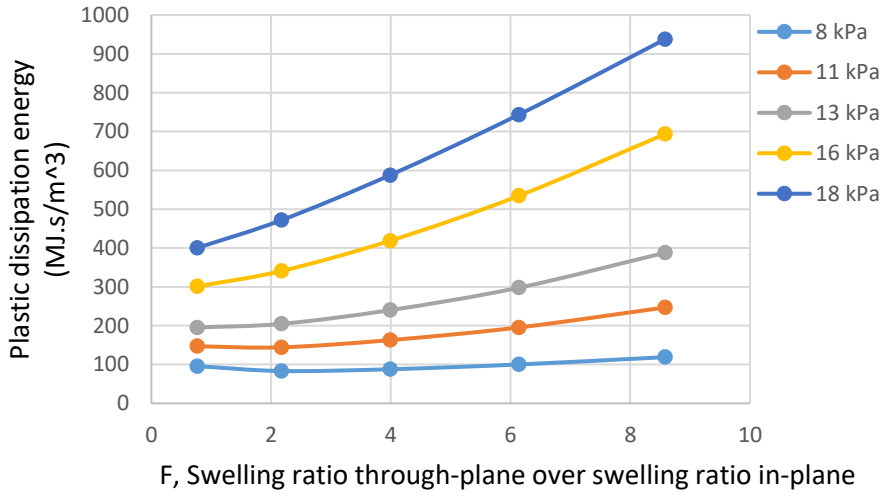

Figure 42 How plastic dissipation energy changes with F at 60 °C

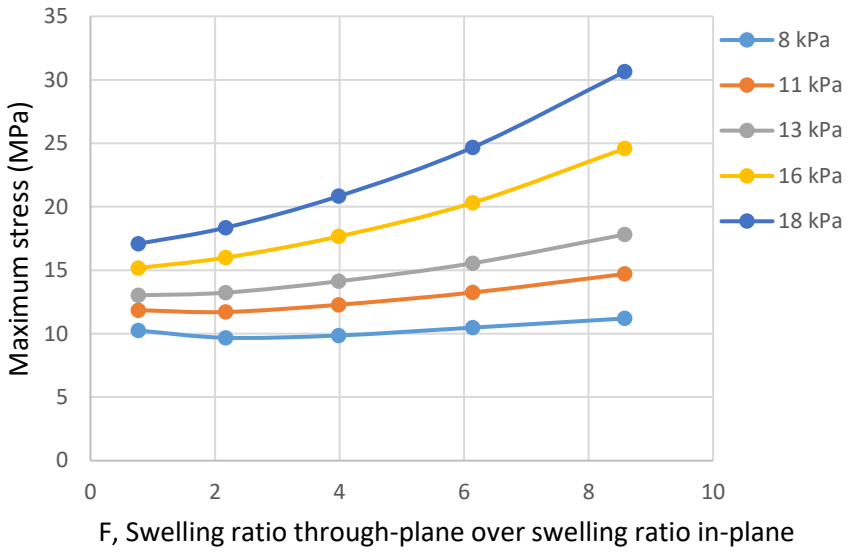

Figure 43 How Maximum stress changes with F at 60 °C

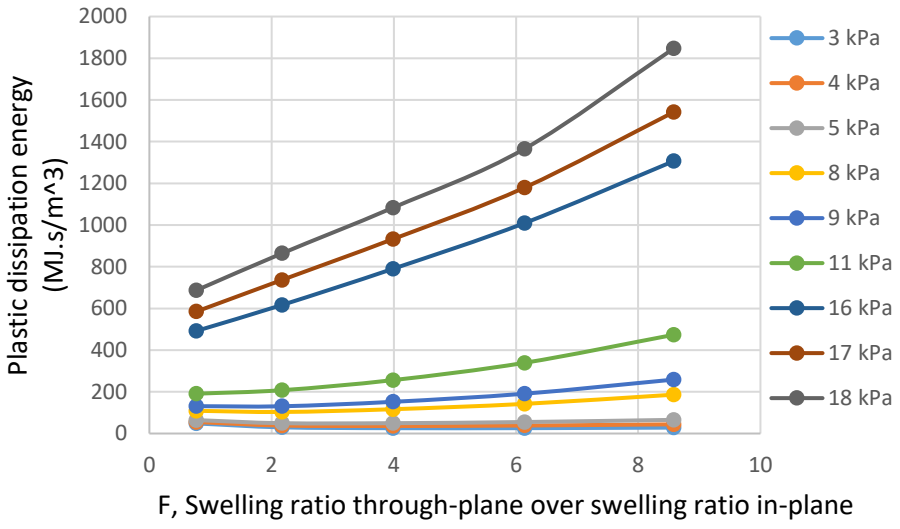

Figure 44 How plastic dissipation energy changes with F at 90 °C

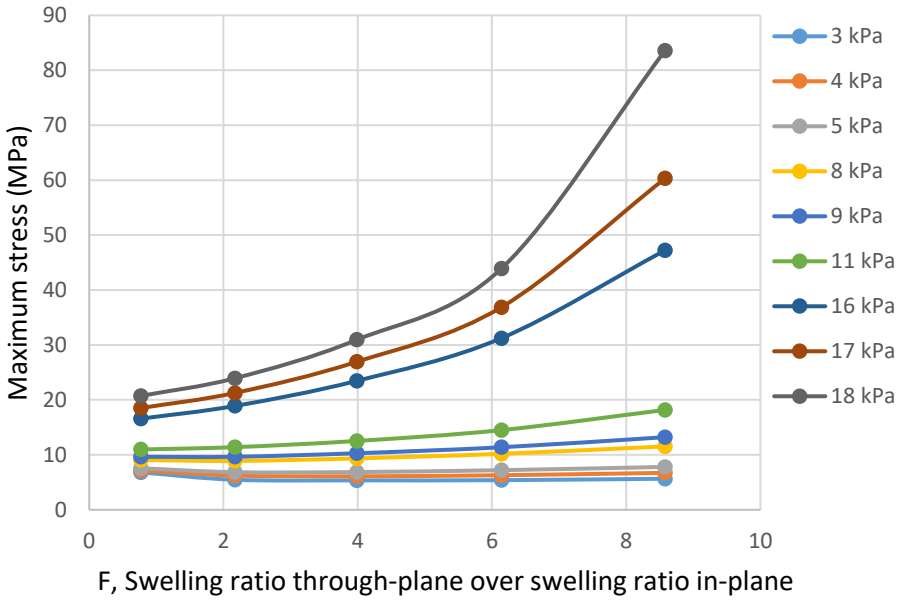

Figure 45 How Maximum stress changes with F at 90 °C

4.2.3 FEM fatigue modeling on a complete PEFC

In the previous section, the FEM model of ΔP-AMST was presented, and now, in this section, the membrane in a full fuel cell has been modeled so that all in-situ constraints and boundary conditions that a membrane endures have been applied. The final purpose of the mechanical fatigue modeling is to apply it to a complete fuel cell with its real conditions. In this modeling, all the main components of a fuel cell, including the CL, GDL, and bipolar plates, are simulated. The boundary conditions on the membrane such as clamp pressure, wall constraints, and interfaces of the membrane with CL, as well as the pressure differential between anode and cathode sides, are considered.

In this study, in three steps, the FEM modeling has been implemented. The first step is to use the generalized G'Sell-Jonas theory (equation 28) to model the experimental results of the tensile tests conducted on the reinforced membrane in four different ambient conditions (80 °C – 90% RH, 80 °C – 30% RH, 25 °C – 90% RH, 25 °C – 30% RH) at two different strain rates (1% and 10%). This step allows for the extraction of all material parameters for equation 28. The second step involves modeling the in-situ ΔP-AMST for the experimental ΔPs to extract the S-N curves. The third step is to model the membrane in complete fuel cell conditions, with all the components, boundary conditions, constraints, and mechanical properties shown in Figure 46 and Table 6, respectively. The selected

geometry represents a 2D cross-sectional periodic unit cell of a single cell fuel cell, featuring a half-channel and half-land domain with the MEA situated between the anode and cathode flow field plates. In Table 6, for the membrane, thermal expansion coefficient, density, and Poisson ratio, for GDL all properties and for CL all properties except its Young's modulus have been extracted from [61, 70, 109]. For CL, its Young's modulus has been calculated based on equation 33. It is worth noting that the linear elastic material model has been considered for both the GDL and CL. For stress magnitudes exceeding 1 MPa, the generalized G'Sell-Jonas theory is used as an isotropic hardening function to model the reinforced membrane. The interface between the GDL and CL underneath the channel is separate, and they don't have any chemical or physical adhesion to each other, and only friction exists between them, while all other interfacial contacts are fully tied. The clamping pressure is set at 1 MPa, with 1.2 bar pressure on the anode side due to fuel pressure and 1 bar pressure on the cathode side due to air pressure. This FEM modeling is parametric, and any temperature or humidity cycle can be defined as its operating conditions.

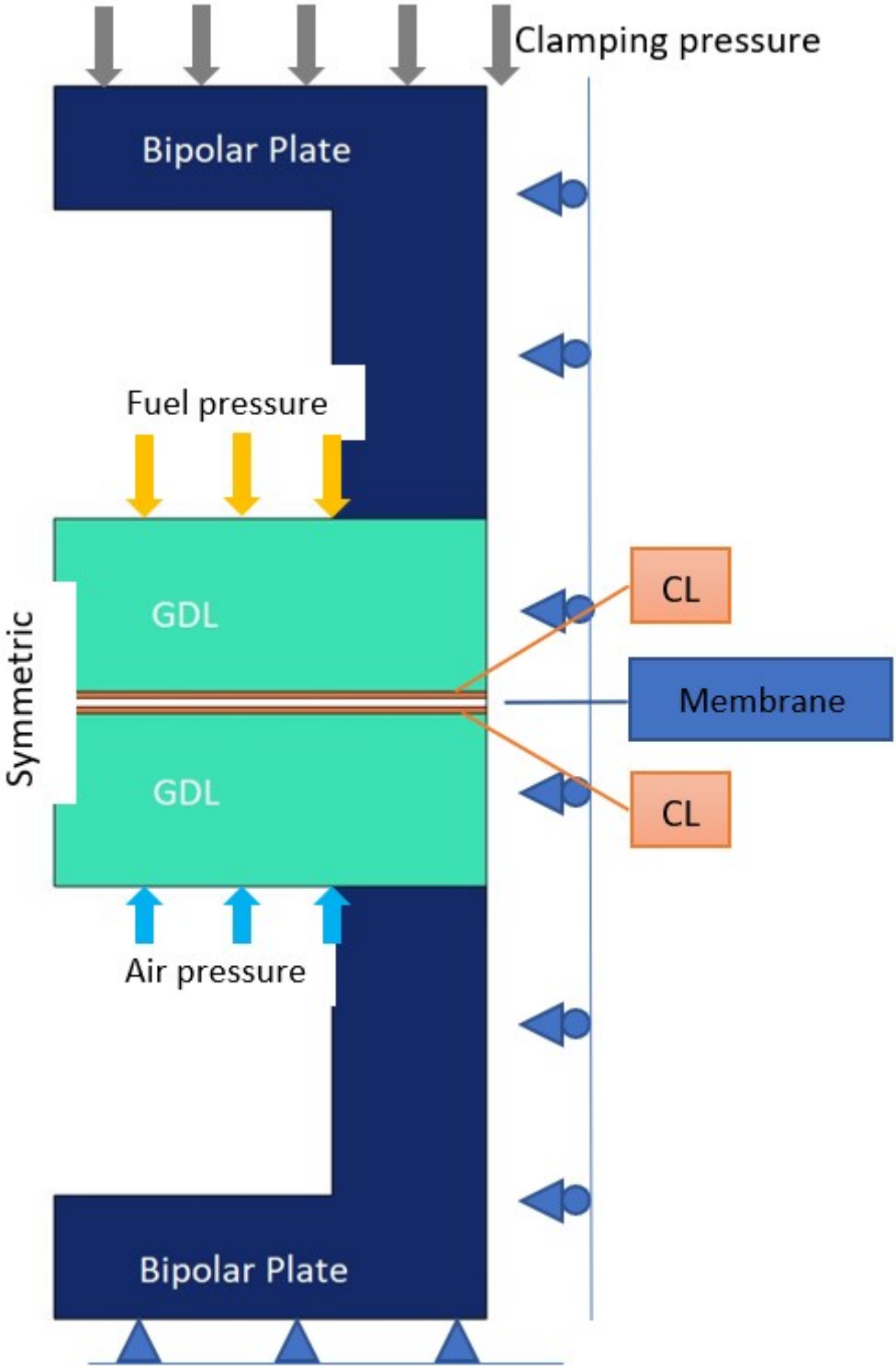

Figure 46 PEFC components, boundaries, and constraints in FEM modeling

Table 6 Material properties of the cell components

Components	Thickness (µm)	Young's modulus (MPa)	Thermal expansion coefficient (1/K)	Density (kg/m^3)	Poisson Ratio
Membrane	15	E (T, RH)	1.2×10^8	1900	0.4
Catalyst layer	10	55	2×10^6	2000	0.3
Gas diffusion layer	280	830	-0.8×10^6	300	0.35

Due to the presence of compressive stress in the in-situ conditions of a fuel cell, the generalized G'Sell-Jonas model is used, since the original G'Sell-Jonas [111, 114] model does not support these conditions. The material parameters required for the membrane were obtained through the tensile test model section in Table 5 and Figure 28, where experimental results were used to optimize the parameters.

Figure 47 displays the in-plane membrane stress distribution in a complete fuel cell at both 60 °C and 90 °C, while the membrane experiences cycles of 60 seconds in 30% RH (dry phase) followed by 30 seconds in 100% RH (wet phase) in each humidity cycle.

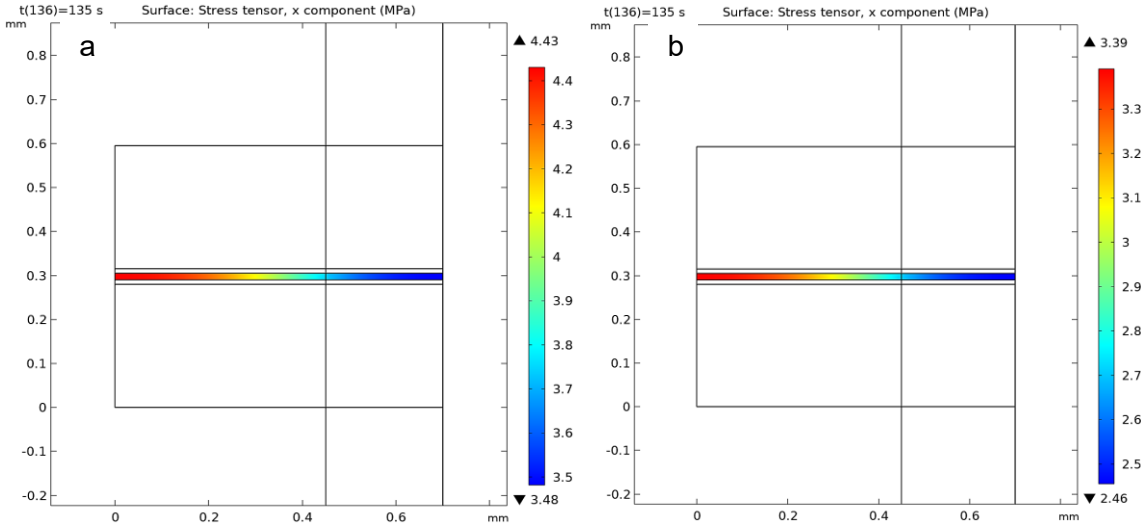

Figure 47 Stress distribution in the x direction (in-plane) in the reinforced membrane in a complete in-situ condition fuel cell in the driest time (135 s, 30 RH) of the RH cycle, a) 60 °C and b) 90 °C

Figure 47 shows that the highest in-plane stress and maximum amplitude stress due to fatigue cycles occur at the center of the membrane under the channel. This location is consistent with previous research [9] that identified it as the area where fracture initiation is most likely to occur. The stress in the x direction is used to measure amplitude and mean stresses because cracks typically initiate at the membrane's surface and propagate through its thickness. Notably, the tensile stress for 60 °C is higher than for 90 °C in the dry phase under both channel and land, as shown in Figure 47. This is because the membrane experiences more stress during the same swelling stain caused by humidity fluctuations at 60 °C because it has a higher Young's modulus at that temperature.

In Figure 48, the stress distribution in the thickness direction is depicted, resulting from clamping pressure, fuel, and air pressures, and swelling strain of the membrane that for both 60 °C and 90 °C are similar. It shows a compressive stress in the entire membrane in through plane direction, which is higher under land than under channel and is reasonable because there is 1 MPa pressure due to the clamp. By comparing Figure 47 with Figure 48, it is inferable that in the dry phase, the membrane is enduring tensile stress in the in-plane direction, while in through-plane, it is under compressive stress.

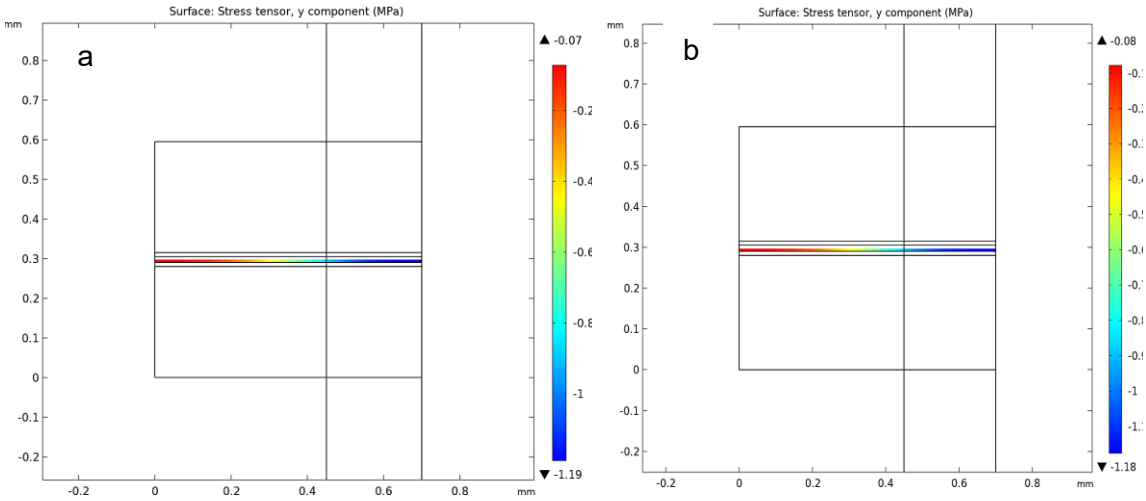

Figure 48 Stress distribution in the y-direction (through-plane) for a) 60 °C and b) 90 °C in the driest time (135 s) of a RH cycle where RH is 30%

Figure 49 shows how stress in-plane (x-direction) and through-plane (y-direction) change during a complete humidity cycle (90 s–180 s) in the center of the membrane under the channel. It is obvious that the stress changes for though-plane are small while for in-plane are great, and in both, the maximum stress occurs around at the driest phase

point (135 s). This figure illustrates again that for both 60 °C and 90 °C, the stress in the through-plane direction is around the same, but in 60 °C, the stress in-plane direction for the critical point is 30% greater than in 90 °C.

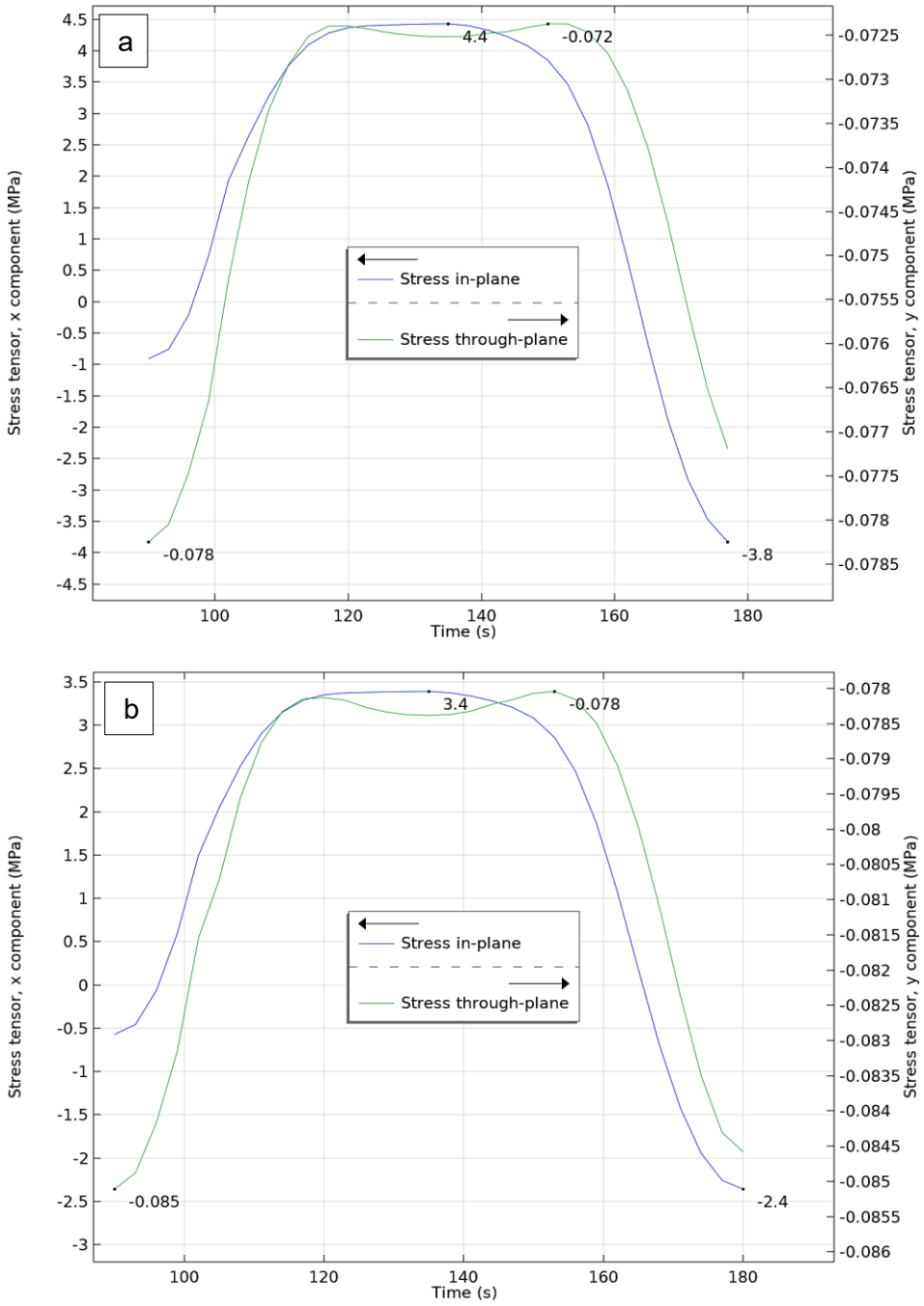

Figure 49 **The changes in stress both in-plane and through-plane for the center of the membrane under channel at a) 60 °C and b) 90 °C while RH changes 30-100%**

Figure 50 depicts the stress in the core layer of the membrane from the center of the channel to the end of land for both dry phase (135 s) and wet phase (180 s). Figure 51 displays the calculated amplitude stresses based on Goodman for the dry and wet phases. Figure 51 confirms that cracks in the membrane are initiated from the center of the channel, as the greatest modified amplitude stress occurs at this critical point for both 60 °C and 90 °C. Once the first crack is initiated at this point, stress concentration is created, causing a significant increase in stress amplitude, and resulting in the propagation of cracks even before initiation in other points that is verified by Ref [87] too. Furthermore, the modified amplitude stress experienced at 60 °C exceeds that at 90 °C. This is because the membrane at 60 °C is more rigid, which allows it to withstand higher stress levels under around similar swelling strains. It's worth noting that the membrane is more durable at 60 °C overall, leading to a longer fatigue lifetime (Figure 33).

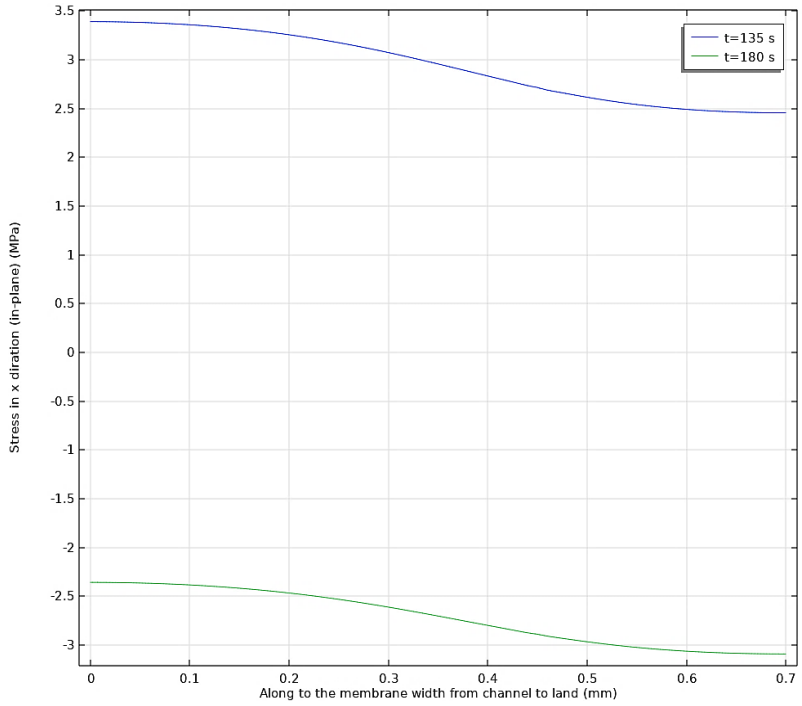

Figure 50 The stress in-plane for dry phase (135 s) and wet phase (180 s) in the core layer of the membrane, 90 °C

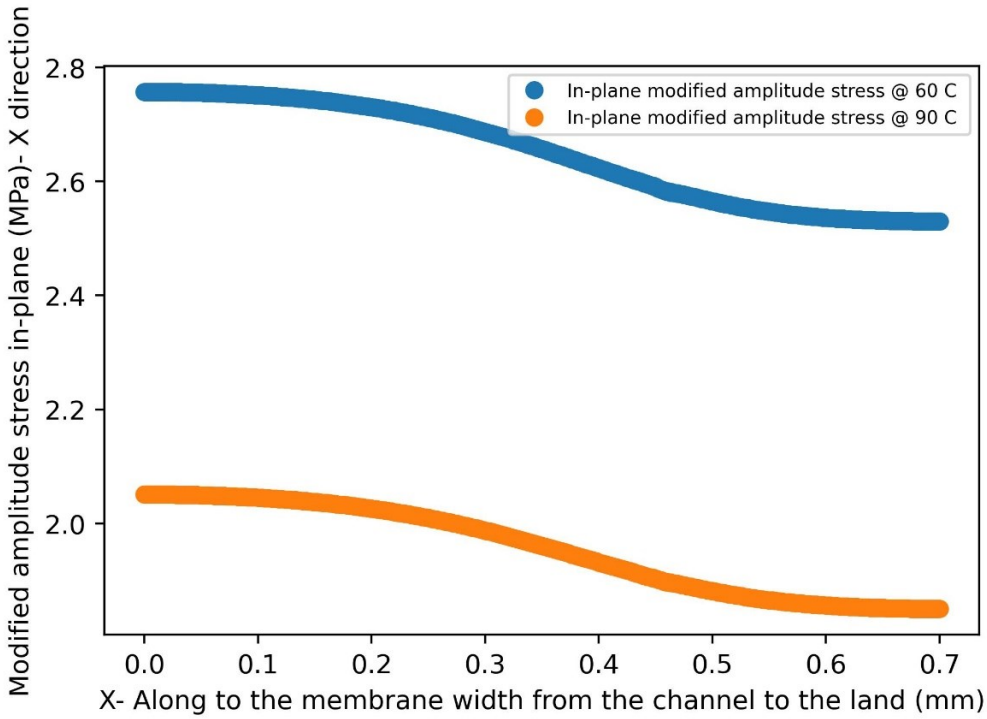

Figure 51 **The modified amplitude stress in-plane between the driest phase (135 s) and the wettest phase (180 s) in the core layer of the membrane, both 60 °C and 90 °C**

For more confirmation of the calculated stress, especially in the in-plane direction, a 3D model of the MEA has also been modelled in Figure 52 with exactly the same boundary conditions as the 2D model at 90 °C RH cycles from 30% to 100%.

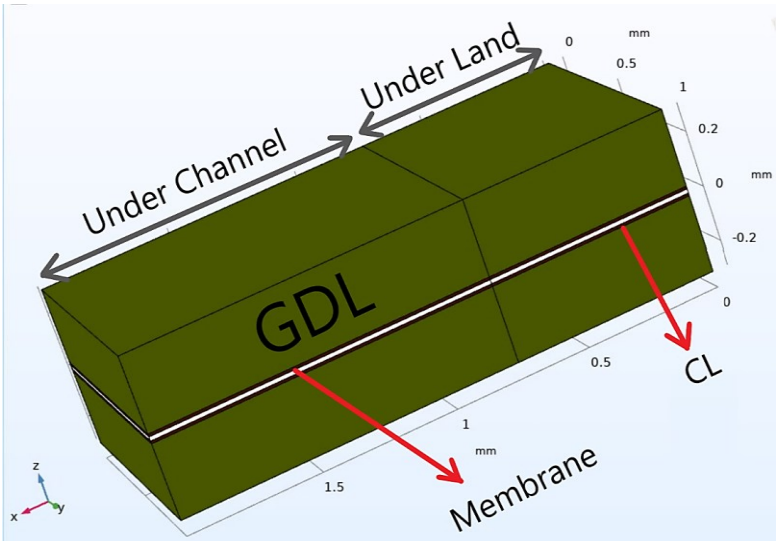

Figure 52 **A schematic figure from the 3D model of the cell**

The in-plane stress distribution in the center of the membrane from land to the middle of the channel in the driest point (135 s) has been shown in Figure 53, representing less than 10% deviation from its 2D equivalent in Figure 47 for 90 °C. Therefore, a 2D model would be accurate enough and would require much less time for calculation.

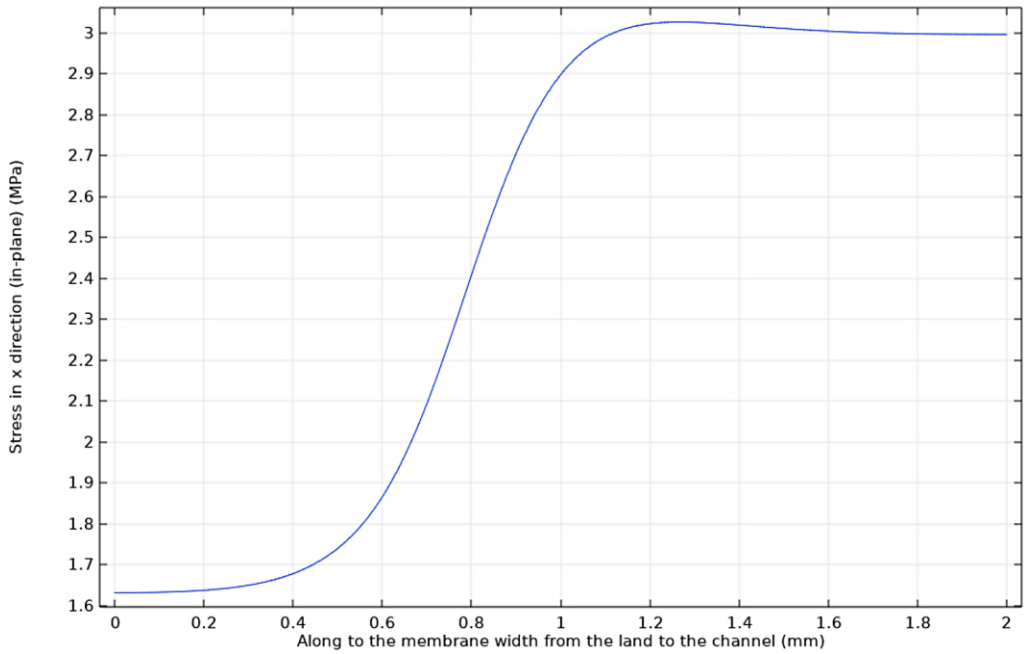

Figure 53 The in-plane stress distribution in the center of the membrane from land to the middle of the channel for the 3D model

5 Estimating the in-situ fatigue lifetime of the reinforced membrane

The ultimate step of this study is to use the tests and modelling from both accelerated tests in ex-situ and in-situ in previous sections to estimate the mechanical fatigue lifetime of the membrane in a complete fuel cell with its real conditions. Algorithms for integrating the effects of chemical membrane degradation on mechanical fatigue durability are also presented.

5.1 Estimating the in-situ mechanical fatigue lifetime of the reinforced membrane

The fatigue lifetime estimation approach in this study is based on the principle of accumulated plastic dissipation energy, which is a strong indicator of crack initiation and propagation in fatigue models. The approach involves mapping the fatigue lifetime from ΔP-AMST to a complete fuel cell.

In the first step, “FEM modeling of the pressure-differential accelerated mechanical stress test (ΔP-AMST)”, ΔP-AMST experiments are conducted at two temperatures (60 and 90 °C), where humidity changes from 30% to 100% in 60 s and 30 s, respectively. Using the experimental results and modeling, the accumulated plastic dissipation energy and modified amplitude stress in the center of the bulge that has the maximum stress for the experimented ΔPs are calculated.

In the second step, “FEM fatigue modeling on a complete PEFC”, for the membrane in the complete fuel cell, the modified amplitude stress and plastic dissipation energy for one humidity cycle are computed at the critical point of the membrane, which has the largest in-plane stress and is in the middle of the channel.

In the third step (that is this section), equivalent ΔPs in the experimented ΔP-AMST that have the same amplitude stress as the complete fuel cell are extracted through interpolation among the experimented ΔPs for each complete fuel cell temperature model (60 and 90 °C).

In the fourth step (that is this section), the accumulated plastic dissipation energies are calculated for the two equivalent ΔPs as inputs for the ΔP-AMST FEM model.

Finally, in the last step (that is this section), by dividing the accumulated plastic dissipation energy in the ΔP-AMST model by the plastic dissipation energy in one cycle of the complete fuel cell, the fatigue lifetime is projected from ΔP-AMST to the complete fuel cell for every temperature. Figure 54 illustrates this estimation approach for a complete fuel cell's fatigue lifetime. In this workflow, we have omitted the influence of creep effects. To calculate the total plastic dissipation energy, we simply multiply the plastic dissipation within one cycle by the number of fatigue lifetime cycles. Additionally, to account for the influence of dry phase durations on fatigue lifetime, we also multiply this duration by the accumulated plastic dissipation energy. Consequently, this approach not only predicts the fatigue lifetime of an entire fuel cell based on ΔP-AMST and an in-situ accelerated test, but also takes into consideration the effects of RH cycle frequency. Another innovative aspect of this method is its applicability to any type of membrane, including coated catalyst membranes, provided that their tensile tests and ΔP-AMST results are available. Alternative methods for determining the in-situ fatigue lifetime of membranes can be quite time-consuming. For instance, protocols such as DOE can be labor-intensive and lengthy. Additionally, some approaches rely on crack propagation modeling, which often involves conducting tests in an ex-situ environment. Alternatively, when attempting to implement methods for online crack monitoring, techniques like XCT can be expensive and demand more time compared to our approach.

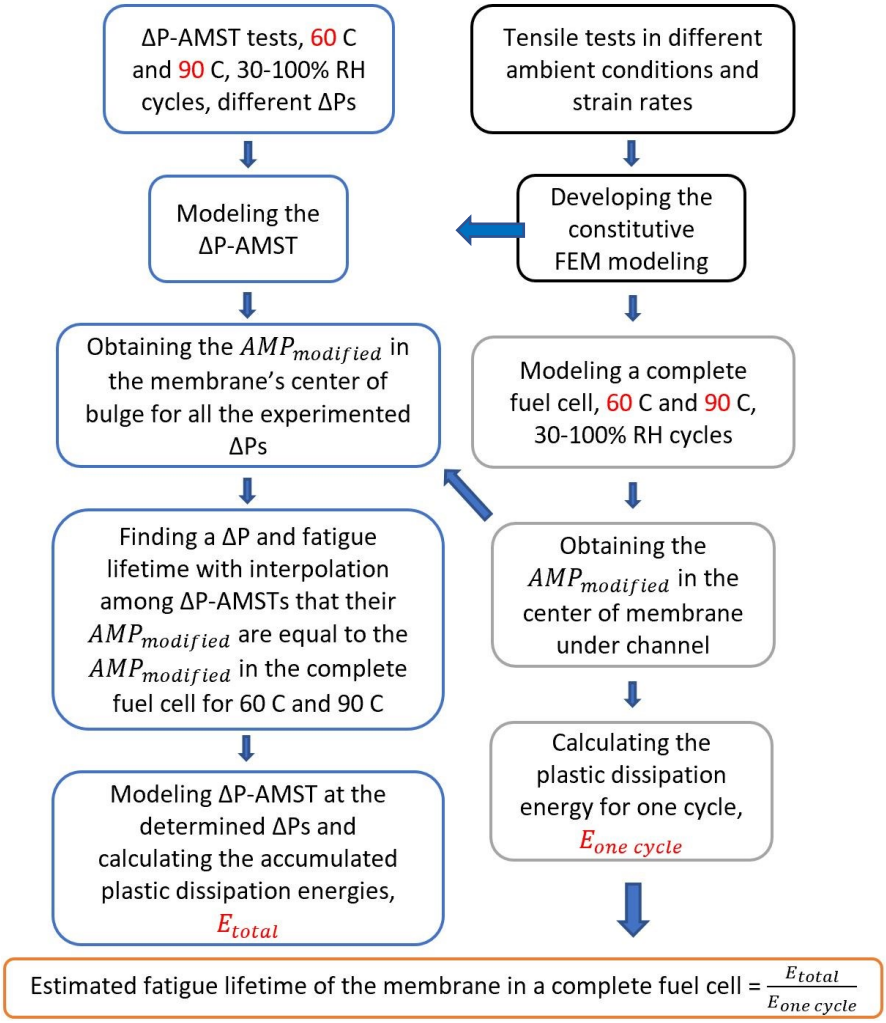

Figure 54 The entire process of estimating the membrane's fatigue lifetime in the complete fuel cell model is based on tensile tests, ΔP-AMST experiments, and FEM models.

The mapping method for calculating the real mechanical fatigue lifetime in a complete fuel cell based on the ΔP-AMST has been verified through Table 7. The table presents the fatigue lifetimes obtained from the mapping method and experimental tests for different RH and temperature conditions available in the literature for reinforced membranes. Three membrane fatigue studies were performed at 80 °C in Ref [89, 96], and in each experiment, the membrane went through a different dry phase during its humidity cycles. In the final column of Table 7, the fatigue lifespan has been reported. The results show that the predicted fatigue lifetimes from the mapping method are in good agreement with the experimental tests from other studies, which indicate the reliability and accuracy of the method. It is worth noting that the dry phase of the RH cycles has been

reported in Table 7 because during this phase, tensile stress is applied to the membrane due to swelling strain, which is the root cause of crack initiation. The reported results suggest that the mapping method can be a useful tool for predicting the fatigue lifetime of the membrane in a complete fuel cell under different operating conditions. It is worth mentioning that because reinforced membranes have more mechanical durability, in-situ mechanical fatigue tests are costly and time-consuming [97, 126], and therefore there is little information available in the literature about their in-situ fatigue lifetime. However, these issues have been addressed by the presented approach.

Table 7 Verifying this fatigue lifetime mapping approach for other conditions

The tests and modelling in this study							Verifications with [89,96]
Temperature (C)	Dry phase (s)	Strain Rate %	Plastic dissipation energy in one cycle of a complete fuel cell (MJ.s/m^3)	Plastic dissipation energy in one cycle of ΔP-AMST (MJ.s/m^3)	Accumulated plastic dissipation energy (MJ.s/m^3)	Estimated fatigue lifetime of the membrane in a complete fuel cell (RH cycles (N))	Fatigue lifetime (RH cycles (N))
90	60	5.33	8.03	87.74	76378.80	9515	
60	60	4.86	11.14	232.50	296978.42	26658	
80	44	6.96	9.11			16449	17648
80	29	10.56	6.44		149912.00	23286	20218
80	89	3.44	16.44			9120	11178

Table 7 shows that the predicted fatigue lifetimes have a deviation of about 10% from those reported in references [89, 96] (in the three last rows), which is reasonable given the slight differences in material properties. For the presented tests in Table 7 from [89, 96], every test has been repeated twice, and their presented results for fatigue lifetimes are less than 5% from their averages for 44 s and 89 s as dry phases in every RH cycle and around 10% for 29 s and therefore, the predictions for these tests based on our approach is rational. To account for the dry phase duration in each cycle and to eliminate the impact of element size in critical points in both the ΔP-AMST and the complete fuel cell, the plastic dissipation energies were multiplied by the dry phase times and divided by the element volumes in FEM modeling. If we assume a 10% deviation in the applied ΔP as shown in Figure 33, the fatigue lifetime at 90 °C in Table 7 would range from 8563 to 10466 cycles, representing a variation of ±10% around the base value of 9515 cycles.

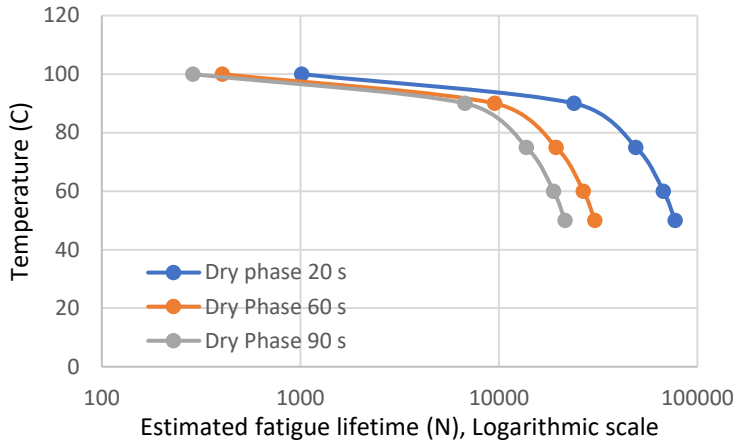

Figure 55 Estimated fatigue lifetime for the reinforced membrane in a complete fuel cell at 100, 90, 75, 60, and 50 °C with 20, 60, and 90 s as the dry phase time in every cycle

Figure 55 shows the estimated mechanical fatigue lifetimes for various temperatures and relative humidity cycles based on FEM model constructed for both ΔP-AMST and a complete fuel cell. The graphs in Figure 55 suggest that the membrane fatigue lifetime decreases significantly at higher temperatures. For instance, if the dry phase is 90 s, the fatigue lifetime at 100 °C is 288 cycles of 30–100% RH, while at 50 °C it is 21545 cycles. This trend is also observable in the tensile test results (Figure 23-a), where the Young's modulus at 100 °C is around 30–40% of the Young's modulus at 50 °C, and therefore, the membrane at higher temperatures is softer. Besides, this trend that in higher temperature, membrane's fatigue lifetime is much less was confirmed in our ΔP-AMST. However, this effect can be mitigated by increasing the RH and avoiding the dry mode on the membrane. Figure 39 and Figure 48 demonstrated that the highest stress and strain levels occur during the dry phase. Therefore, if we prolong the membrane's exposure time to the dry phase, it will lead to an increased dissipation of plastic energy, ultimately resulting in a reduction in the membrane's fatigue lifetime. For instance, based on Figure 55, in 60 °C, when the dry phase for every cycle decreases from 90 s to 20 s, membranes will experience more wet phases, and the fatigue lifetime has increased from 18873 to 67449 and this trend is confirmed by [27, 28, 88, 89, 96].

Figure 56 demonstrates how the fatigue lifetime varies under different dry phase conditions, specifically at 30-100%, 50-100%, 70-100%, and 90-100% RH, at both 90 °C and 60 °C temperatures. The dry phase duration is 60 seconds in both temperatures. The

data clearly highlights that the dry phase level plays a significant role in determining fatigue lifetime. For instance, at 90 °C and 30-100% RH, the predicted fatigue lifetime is 9521 cycles, whereas at 70-100% RH, it substantially increases to 16905 cycles.

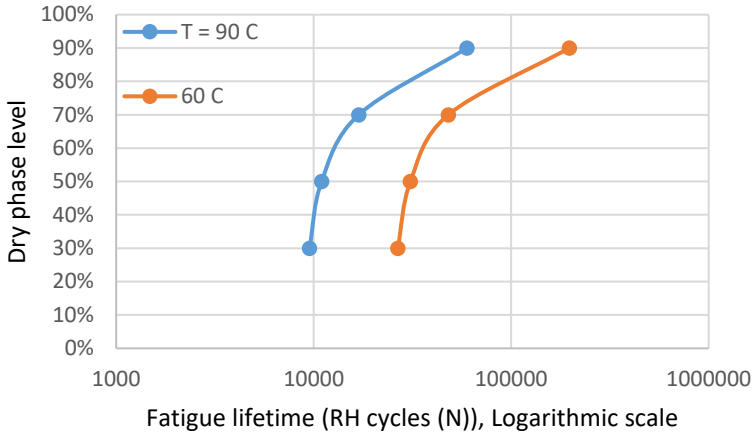

Figure 56 Fatigue lifetime predictions in different dry phase levels at both 60 and 90 °C

The swelling ratio in through-plane in this study is approximately 8.75 times bigger than in plane, according to earlier studies in reinforced membrane [89, 96]. A factor, X, is multiplied in the swelling ratio through-plane (z), and a factor $1/\sqrt{X}$ is multiplied in the swelling ratio in-plane in both directions (x and y), to change the swelling ratio through-plane and in-plane while the volume change is constant. This is done to investigate the effects of swelling ratio on maximum stress and plastic dissipation energy, which occur in the center of the channel. The influence of swelling ratio in-plane and through-plane on maximum stress and plastic energy dissipation in one cycle during the dry phase (60 s) is depicted in Figure 57 at various differential pressures, where F is swelling ratio through-plane over swelling ratio in-plane.

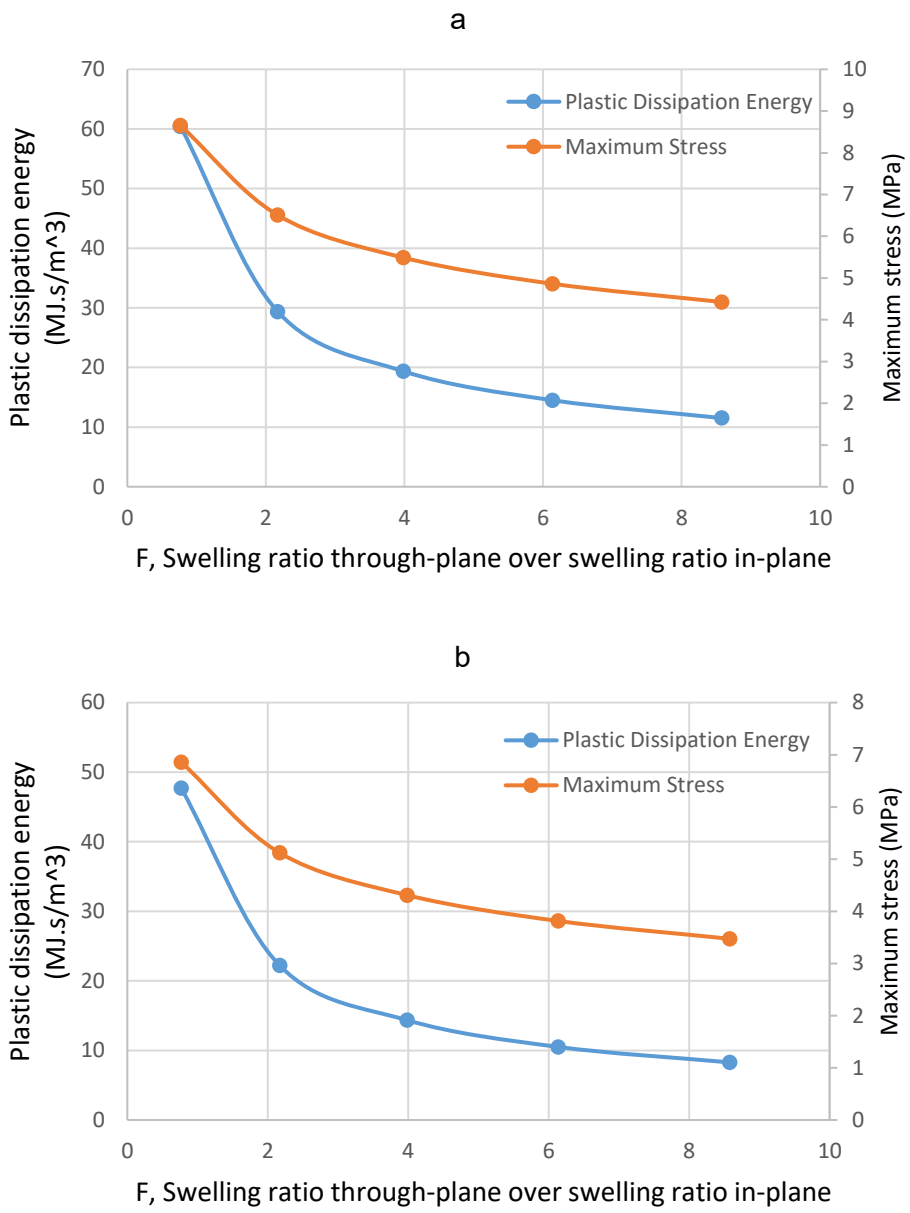

Figure 57 How plastic dissipation energy and maximum stress change with F at a) 60 °C, b) 90 °C

In Figure 57, at both 60 °C and 90 °C, when F is equal to 1—indicating a higher isotropic condition where the swelling ratio is the same in all main directions, as in non-reinforced membranes—the plastic dissipation energy is 5-6 times greater than when F is 8.75. Similarly, the maximum in-plane stress at the center of the membrane, under the channel during the driest time, is 2 times greater than when F=8.75.

By assuming a constant CAPDE, it can be concluded that the fatigue lifetime will be reduced to one-sixth. It can be inferred that, for the reinforced membrane type used in this project, the membrane with the greater through-plane swelling ratio will have a longer fatigue lifetime under in-situ fuel cell conditions if they have the same CAPDEs in ΔP-AMST tests due to less plastic dissipation energy in every RH cycle (Figure 55).

One crucial factor in stress distribution in membranes is clamping pressure type as a boundary condition in FEM analysis. In both our ΔP-AMST tests and modeling, as well as in the complete fuel cell model, a constant pressure of approximately 1.5 MPa has been applied to the plate on the anode side, mirroring the pneumatic pressure mentioned in the introduction section. Simultaneously, the plate on the cathode side is fixed. Consequently, the plate on the anode side can move due to membrane expansions and contractions. This state was simulated on the experimented cell in the fuel cell test bench by a bladder pressure valve and its gauge. All the above-mentioned tests and modelling are based on this clamping condition. The reinforced membrane, as mentioned before, has around 50% fluctuation in its thickness due to wet and dry phases, but because the plate can keep its pressure while it moves, membranes under land will always experience compressive stress.

However, in different stack designs, other types of mechanisms are used to create clamping pressure. In some designs, a mechanical mechanism applies clamping pressure to the cell. This type of clamping pressure can be modelled by applying a constant displacement to the anode plate while the cathode plate is fixed. In this condition, due to the high rate of dimensional fluctuations in the thickness of the membrane due to humidity changes, the membrane under land can experience a different stress distribution in both the thickness and the plane. Because just a 2-3 μm displacement in the anode plate and considering both GDL and CL as rigid layers with mentioned properties in Table 6, can apply 1-1.5 MPa of compressive pressure to the membrane prior to fuel cell operation, this sort of clamping mechanism causes the membrane beneath the land to experience tensile stress. Because all the components are tied to one another under land, when a fuel cell operates and reaches the dry phase, the anode has only moved 2-3 μm while the membrane wants to squeeze 6.7 μm, causing tensile stress in the membrane. In Figure 58, when that displacement on the anode plate is 1.5, 3, 4.5, 6, and 7.5 μm, the stress distribution in though-plane direction (y) at 90 °C in the driest phase; 135 s (RH 30%), in both through-plane and in-plane has been illustrated. According to Figure 58, the

likelihood of failure under land will rise when this mechanism, which involves constant displacement of the anode plate, is used in clamping pressure designs. Additionally, since tensile stress is generated in this type of clamping mechanism both in-plane and through-plane under land, the algorithm to estimate fatigue lifespan should employ their equivalent von-mises stress.

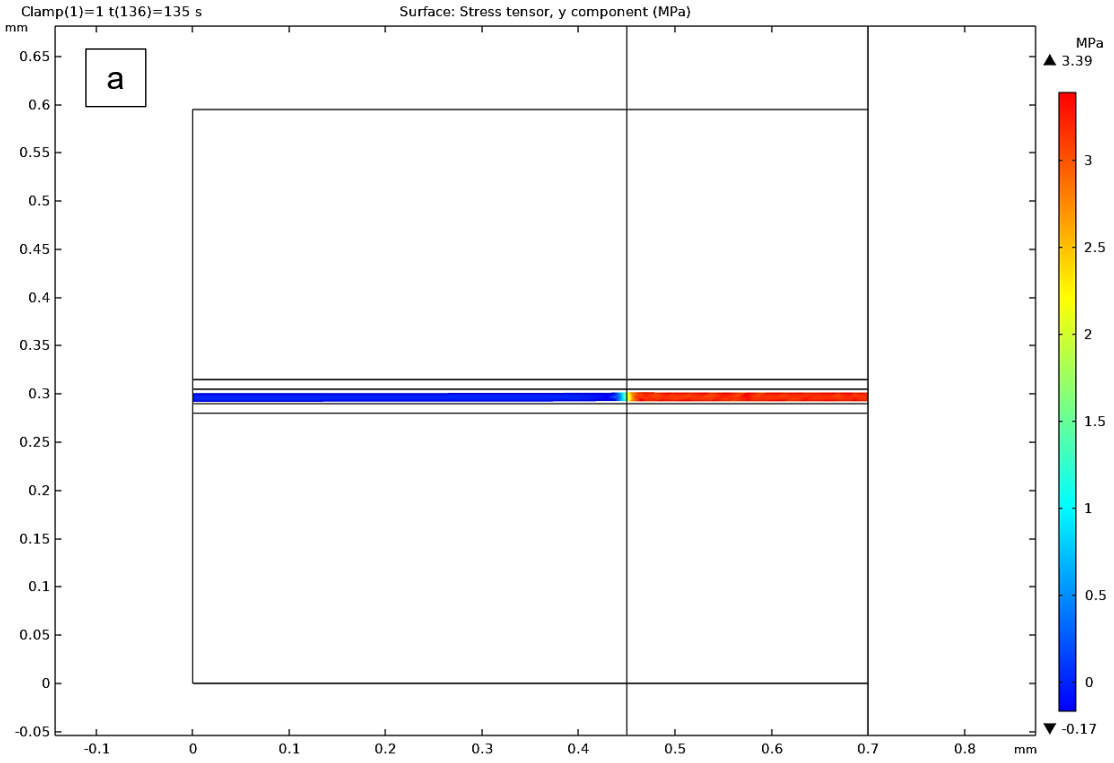

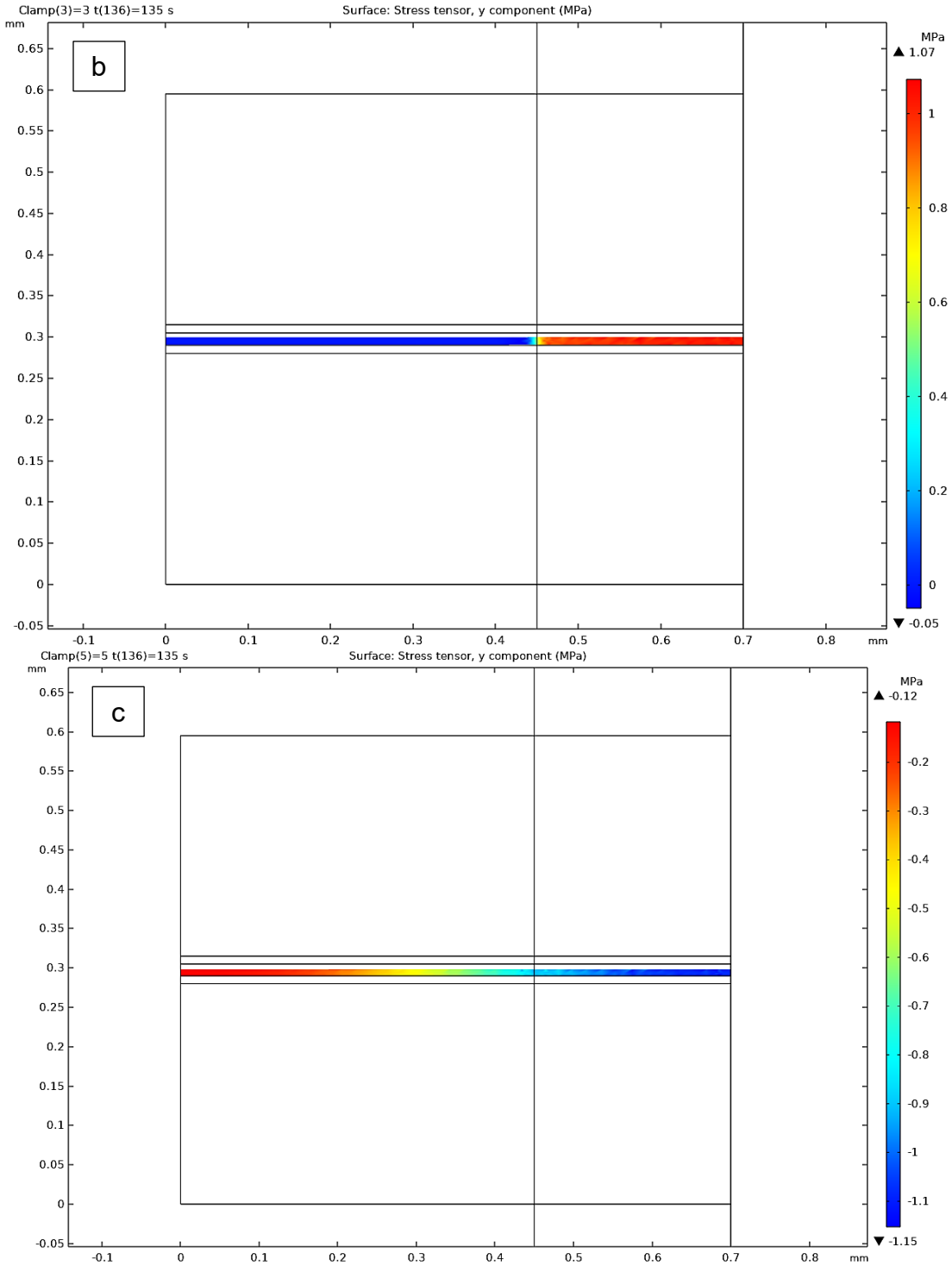

Figure 58 How stress in the y direction changes with different applied displacements on the anode plate, a) 1.5, b) 4.5, and c) 7.5 µm displacement, respectively. T=90 °C.

In Figure 59, the change in stress distribution for x direction that represents in-plane stress has been shown. When comparing Figure 57 with Figure 46, where clamping

pressure is applied by a constant pressure rather than a constant displacement, the maximum in-plane tensile stress, which is the origin of crack initiation, is in the center of the channel. In contrast, in the current scenario, the maximum in-plane tensile stress on the membrane is situated beneath the land. Furthermore, this comparison illustrates that when clamping pressure is kept constant and is around 1 MPa pressure on membrane under land, the tensile stress levels are approximately 20% lower, suggesting a potential increase in fatigue lifetime. But in high clamping displacements like figure 57-c, the tensile stress distribution is more similar to the pressure constant scenario, and the maximum tensile stress also happens again in the center of the membrane under the channel and so both clamping scenarios have a same result.

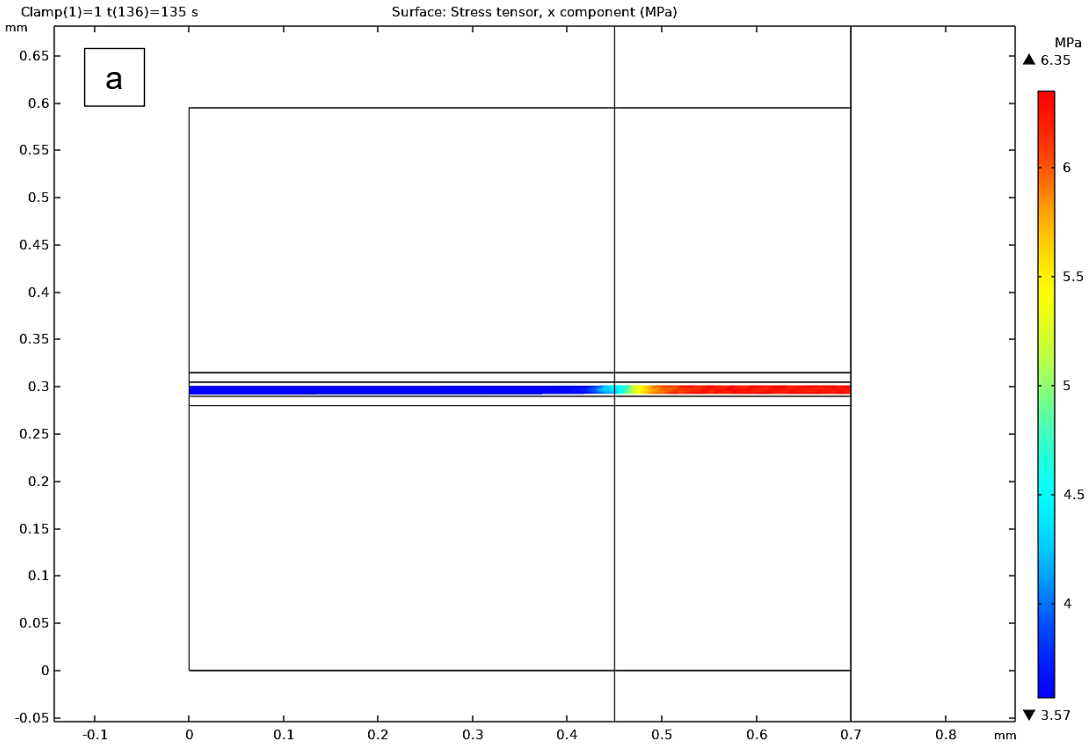

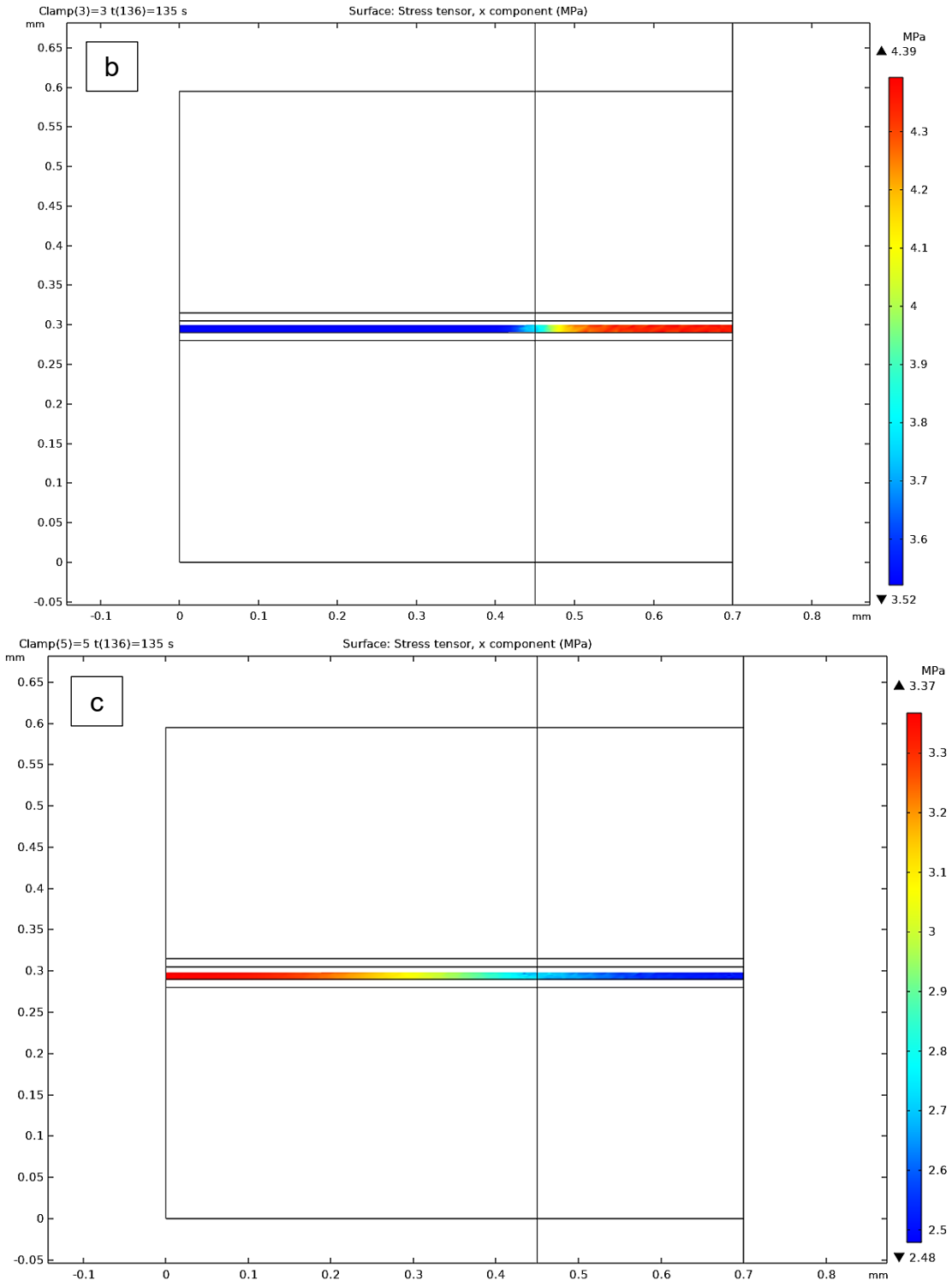

Figure 59 **How stress in the x direction changes with different applied displacements on the anode plate, a) 1.5, b) 4.5, and c) 7.5 µm displacement, respectively. T=90 °C.**

Figure 60 depicts how the membrane's stress is affected by the GDL and CL Young's moduli. Based on the original model where GDL and CL have properties similar to Table 6, this figure shows the changes in stress in the membrane's center under the channel during an RH cycle. When we increase or decrease both GDL and CL's Young's modulus, the stresses in the plane only change by a small amount, about 2-3%, whereas the stresses through the plane change by around 30-50%. However, because there is little through-plane stress and in-plane stress is where crack initiations occur, the membrane's fatigue behavior will not alter. Additionally, it demonstrates that the membrane's own expansions and contractions are its primary source of fatigue.

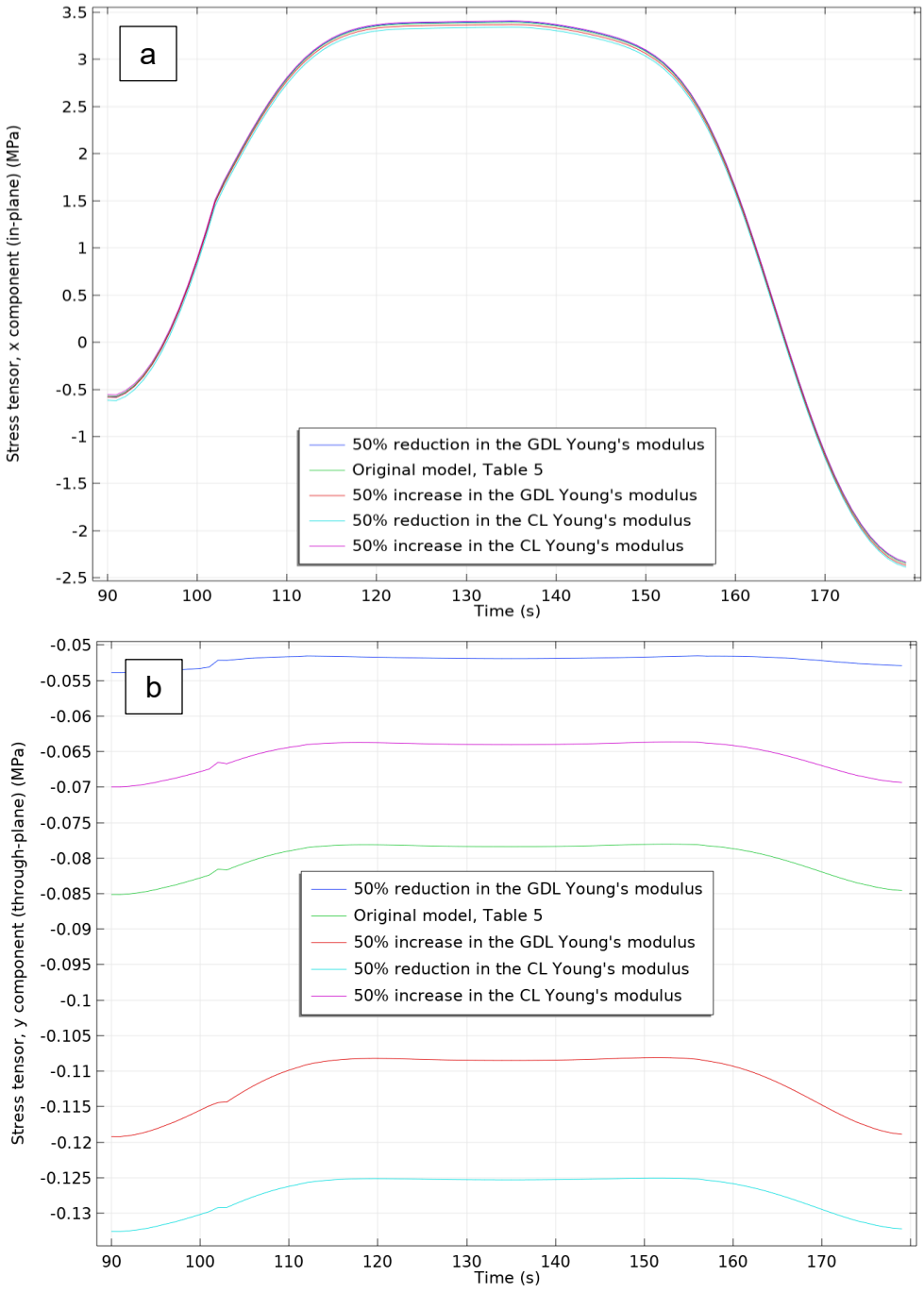

Figure 60 **Stress fluctuations in the center of the membrane under channel when GDL and CL properties have been changed: a) stress in-plane, b) stress through-plane.**

In Figure 61, the effects of increasing the channel width on the membrane's fatigue lifetime are depicted. Here, "L" represents the membrane's width beneath the channel over the land. When the membrane's width under the channel increases by 100% (L = 2)

compared to the case when L = 1, where the membrane's width under the channel equals that under the land, the maximum stress within the plane increases by 30%. Conversely, when L = 0.4, signifying a 60% reduction in the membrane's width under the channel, the maximum stress within the plane decreases by 20%. As a result, an increase in the membrane's width under the channel leads to a reduction in the fatigue lifetime of the membrane.

According to the presented algorithm for predicting fatigue lifetime (Figure 54), for L values of 0.5, 1, and 2, the predicted fatigue lifetimes would be 10462, 10403, and 9834, respectively. The observed difference in predicted fatigue lifetimes does not align with their maximum stress proportions. In fatigue analysis, the modified amplitude stress holds importance, with values of 2.798 MPa, 2.807 MPa, and 2.894 MPa for L values of 0.5, 1, and 2, respectively. These values are relatively close to each other, suggesting that their proportions are more indicative of their fatigue lifetimes.

It is worth noting that no literature data is available to validate these predictions. Additionally, as land and channel width and length itself might play a role in fatigue lifetime [124], conducting more experiments is necessary to achieve more accurate predictions.

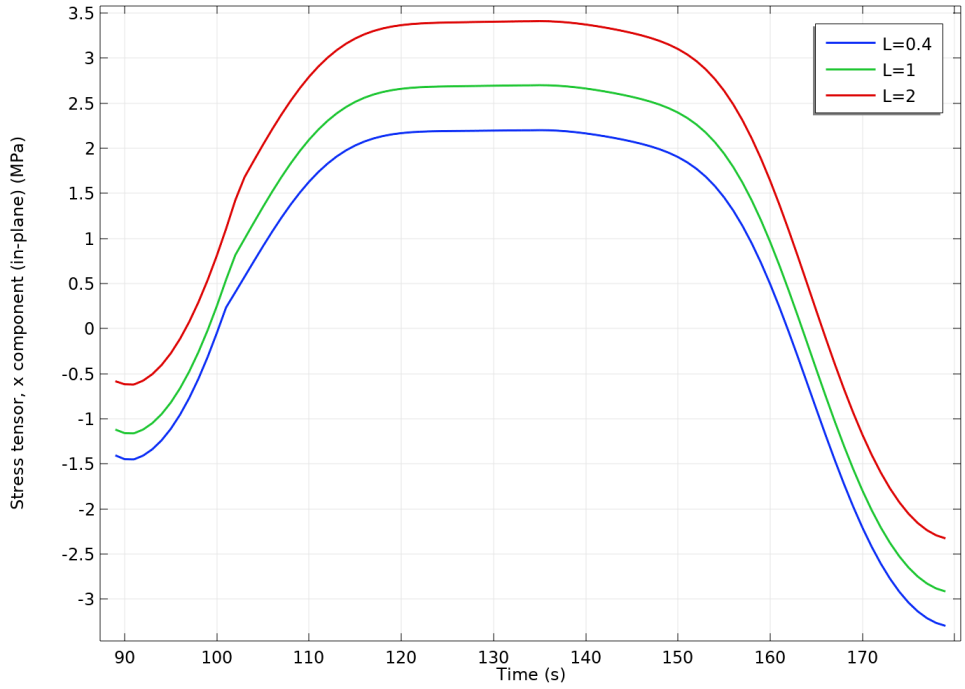

Figure 61 **The impacts of the channel/land width ratio; L on the membrane's stress in-plane and in the center of the channel**

5.2 Integrating chemical degradation into mechanical fatigue modeling of a reinforced membrane and calculating fatigue lifetime

The goal of this section is to integrate chemical degradation into a mechanical fatigue model to predict the ultimate fatigue life of a reinforced membrane. The first step involves performing a series of pressure-differential accelerated mechanical tests (∆P-AMST), building a FEM model for ∆P-AMST based on the developed constitutive model for tensile tests, and extracting its S-N curve. Next, a FEM model for a complete fuel cell is created, and the mechanical fatigue life is estimated by dividing the CAPDE in ∆P-AMST by the plastic dissipation energy in one cycle of the modeled complete fuel cell.

In the last step, the model includes the two main effects of chemical degradation, which are reflected in the thickness of the reinforced membrane and CAPDE. The increased brittleness resulting from chemical degradation [100] is reflected in the updated CAPDE. Figure 62-a, which is from Ref [100], shows the specific work of fracture that is equal to the CAPDE in this study. This is the energy used to create new crack surfaces in the inner fracture process zone that is decreasing due to chemical degradation, which causes a reduction in the CAPDE on the non-reinforced membrane. To obtain this reduction for the reinforced membrane, the amount of thinning caused by chemical degradation is extracted for a reinforced membrane at 60 °C and 50% RH from [127], resulting in a 15% reduction in membrane thickness after 15000 cycles, with each cycle having 30 seconds of wet and 60 seconds of dry periods. In order to generalize the percent of membrane thinning in its real operational condition, x% has been considered a thinning factor due to chemical degradation in-situ conditions.

Based on this thinning (x%), the amount of accumulated fluoride loss for a non-reinforced membrane is extracted from [34], which is around 50 ($\mu mol.cm^{-2}$) in a cyclic open circuit voltage accelerated stress test. For the reinforced membrane, the FRR is approximately half that of a non-reinforced membrane, resulting in 25 ($\mu mol.cm^{-2}$) [128, 129]. According to [100], this amount of fluoride loss is equivalent to 72 hours in the Fenton test (Figure 62). Furthermore, the FRR in the Fenton test for the reinforced membrane (Nafion XL) is around one-third that of a non-reinforced membrane (Nafion 212) [130], resulting in around a one-third reduction in its accumulated plastic energy due to less fluoride being released and fewer chemical decompositions occurring. The reduction in

CAPDE (y%) is updated for the reinforced membrane based on [100], and by dividing this CAPDE by the plastic dissipation energy of one RH cycle in the updated FEM model that includes the membrane's thickness reduction due to chemical degradation, the final fatigue life is estimated. It is important to note that using ex-situ FRR data to predict a decrease in CAPDE may not be highly precise when applied to in-situ conditions. However, due to the absence of data in the literature regarding how CAPDE changes under chemical degradation in actual fuel cell operating environments, we opted to rely on the ex-situ FRR data from existing studies. In Figure 63, the entire methodology for this integrated mechanical-chemical fatigue lifetime modeling is depicted.

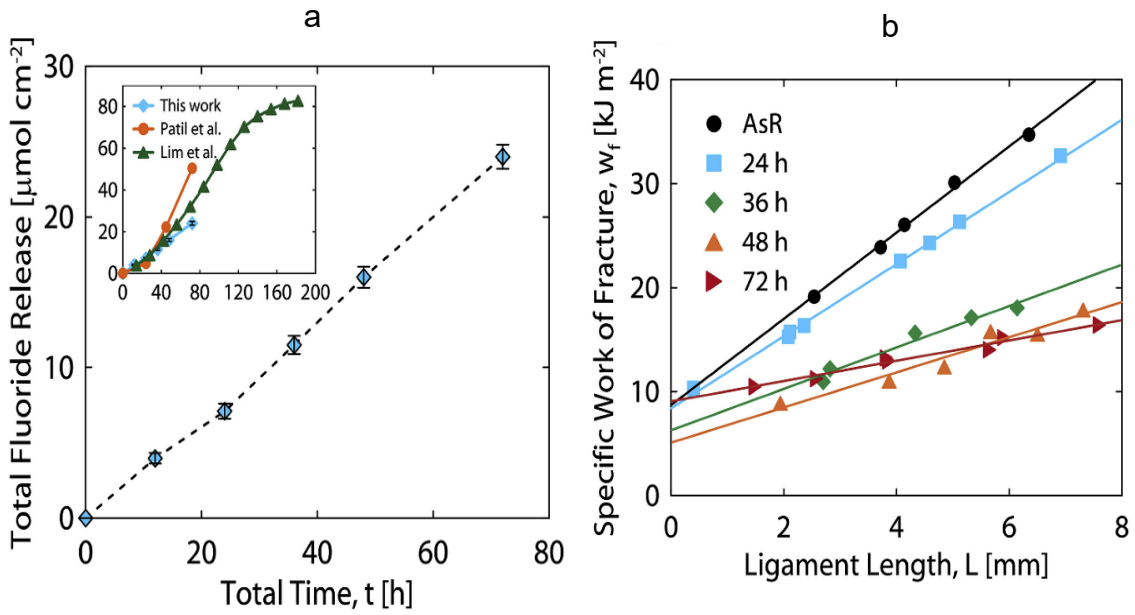

Figure 62 **a) Total FFR based on Fenton test time, b) Specific work of fracture (equal to CAPDE) as a function of ligament lengths for different degraded membranes (samples were employed with the length and width of 30 mm and 10 mm), Reprinted from [100] with permission from Elsevier**

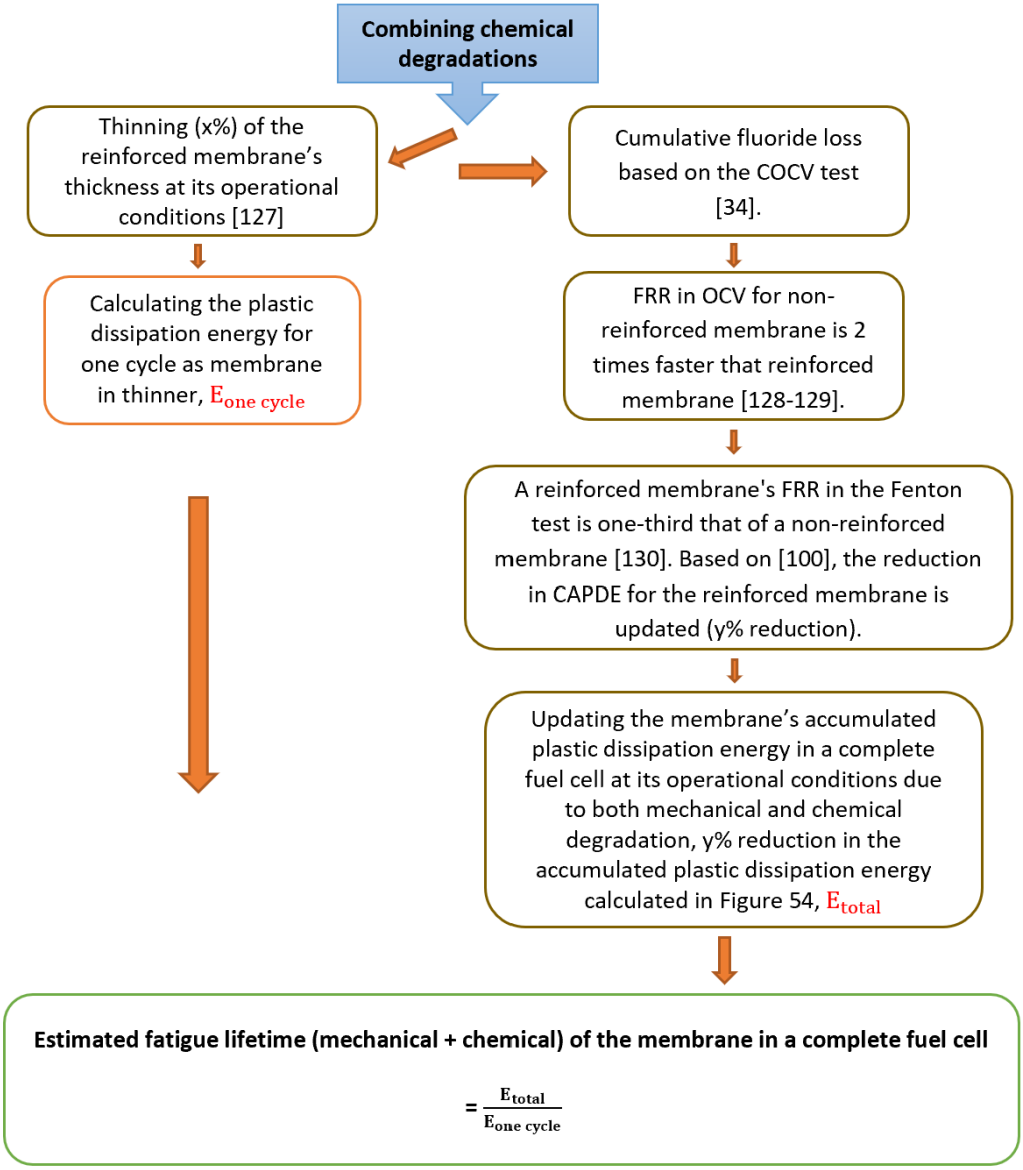

Figure 63 The developed approach for combining chemical degradation into mechanical fatigue modeling

By following the algorithm presented in Figure 63, the predicted fatigue lifetime for a case based on the references mentioned in Figure 63 has been brought into Table 8.

Table 8 The fatigue lifetime by considering chemical degradation, 60 °C and 30-100% RH.

Fatigue	Swelling Strain rate	Plastic dissipation energy in one cycle of a complete fuel cell (MJ.s/m^3)	Accumulated plastic dissipation energy (MJ.s/m^3)	Estimated fatigue lifetime of the membrane in a complete fuel cell (N)
By combining chemical degradation	4.4	11.15	178333	**15994**
Only mechanical fatigue	4.4	11.14	296978	**26658**

In this case, a reduction of around 20% in membrane thickness is applied at 60 °C and 50% RH conditions due to chemical degradation [127] at the beginning of the simulation, and the plastic dissipation energy for one RH cycle is calculated. According to Table 8, the fatigue lifetime has decreased by approximately 40% due to the integration of chemical degradation into mechanical fatigue. It is worth noting that CAPDE gradually decays during fuel cell operation. Therefore, assuming that CAPDE follows a linear trend, as shown in Figure 62, this 40% reduction occurs toward the end of the fuel cell's lifetime. Consequently, at the halfway point in terms of fatigue life, considering chemical degradation, the fatigue lifetime is further reduced by an additional 20%. In Figure 64, the changes in plastic dissipation energy during one cycle in the dry phase with different membrane thicknesses are displayed. The differences are slight, so the first branch in Figure 63 can be ignored, and CAPDE takes on the primary role.

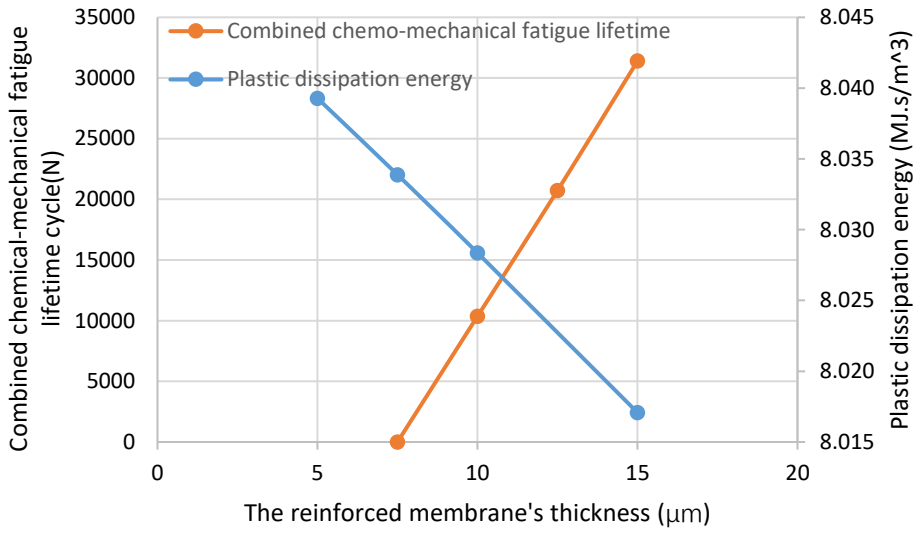

Figure 64 How combined chemical degradation affects mechanical fatigue lifetime and how plastic dissipation energy changes with membrane thickness, 60 °C and 30-100% RH.

In summary, in our initial approach to considering chemical degradation in our fatigue modeling, during a full in-situ test, a reinforced membrane experiences concurrent mechanical and chemical degradation under in-situ conditions. This process initiates with thinning, and the decay in CAPDE follows a linear pattern, as indicated in reference [100]. It demonstrates that an around 20% reduction in membrane thickness due to chemical degradation, occurring simultaneously with mechanical degradation, leads to a 40% reduction in the CAPDE. Consequently, the chemical effects further decrease the fatigue lifetime of the membrane by an additional 40%. As referenced in [34, 131], a linear correlation exists between the reduction in membrane thickness and fatigue lifetime when both chemical and mechanical degradation occur in real fuel cell conditions. Specifically, chemical degradation causes less than a 30% reduction in thickness, and after 30%, the H_2 leakage is 2-3 times more.

As part of the overall verification process for the presented algorithm on combining chemical degradation, Mukundan et al.'s [27] study has been examined. In one of their tests, Nafion XL with a thickness of 27.5 μm underwent OCV+RH cycles (45 sec dry/30 sec wet at 90 °C). When the H_2 crossover sharply increased, it indicated membrane failure. The membrane thinning is approximately 3% after 440 hours, equivalent to 21,000 RH cycles. Based on the aforementioned explanations, we assume a linear correlation

between membrane thinning and its fatigue lifetime due to chemical degradation. If a 20% reduction in the previous study leads to a 40% reduction in CAPDE, then this 3% reduction would result in a 6% reduction in CAPDE. According to Figure 55, the mechanical fatigue lifetime in the 45 sec dry/30 sec wet condition would be around 18000 cycles. After a 6% reduction due to CAPDE, the chemo-mechanical fatigue lifetime would be around 17000 cycles. The difference between our estimation and the experimental result from Mukundan's study is around 19%, which may be attributed to slight differences between our modeling boundary conditions and Mukundan's experiments and also limited available data for ΔP-AMST on Nafion XL [132]. It is worth mentioning that the use of a radical scavenger to mitigate chemical degradation in Nafion XL, as studied by Mukundan [27], is the reason for the minor thinning (3%) in membrane thickness.

The second approach to calculating the decline in CAPDE is to just consider this decline for non-reinforced membranes and extend its proportion for reinforced membranes. It is just based on tensile tests' chemically degraded membranes. As Ref [127] mentions, in chemical degradation at the fuel cell's in-situ conditions, the reinforced membrane thickness thins by around 20% after 26658 in Table 8. According to Bhattacharya et al. [133], in an isolated chemical degradation, after 140 hours of steady-state open circuit voltage (SOCV) during accelerated stress tests (ASTs), this thinning (approximately 20%) happens for the membrane. If we assume that CAPDE for a membrane due to fatigue has a proportion to its plastic dissipation energy in its tensile test, we can use the plots in the tensile tests' results of chemically degraded membranes in Figure 65 to extend how chemical degradation can reduce CAPDE. If we calculated the area under the curve of stress-strain for beginning of life (BOL) and for the 140-hour test of SOCV, the area has decreased around 75%, and therefore, it is logical to extend this proportion for declining at CAPDE due to chemical degradation. As a result, the fatigue lifetime of 31396 cycles is decreased to 7849 when chemical degradation is considered. Consequently, the impact of chemical degradation on the fatigue lifetime of a reinforced membrane in a complete fuel cell condition is around 75% by the second approach, which can be added to the mechanical fatigue degradation model.

In an overall assessment of the second presented algorithm for combining chemical degradation, Mukundan et al. [27] observed a 20% reduction in the thickness of Nafion XL after 200 hours of OCV testing at 90 °C and 30% RH, indicating a sharp increase in H_2 crossover. This suggests that chemical degradation during OCV testing is

more severe, occurring approximately two times faster than under OCV + RH cycling conditions. Therefore, if a 40% reduction in mechanical fatigue lifetime due to chemical degradation is reported in the first method, it is logical to expect a 75% decrease in mechanical fatigue lifetime when OCV phenomena dominate in fuel cell operation. These findings suggest that the extent of chemical degradation during OCV + RH is notably lower than that observed in the OCV test at a constant 30% RH. The decrease in chemical stress is attributed to the hydration component of the cycle. As the MEA undergoes humidification, sulfonic acid end groups in the PFSA become fully ionized and exist in the inert proton form ($–SO_3^-$), making them resistant to hydrogen abstraction by the hydroxyl radical. This prevention of hydrogen abstraction prevents irreversible degradation of the side chain, ultimately avoiding complete chemical decomposition of both the main chain and the side chains associated with that PFSA molecule [86, 134]. Therefore, the recommendation is to use the first method for combining chemical degradation when a fuel cell operates in RH fluctuation conditions. Conversely, when the fuel cell primarily functions in OCV conditions, it is more advisable to employ the second approach.

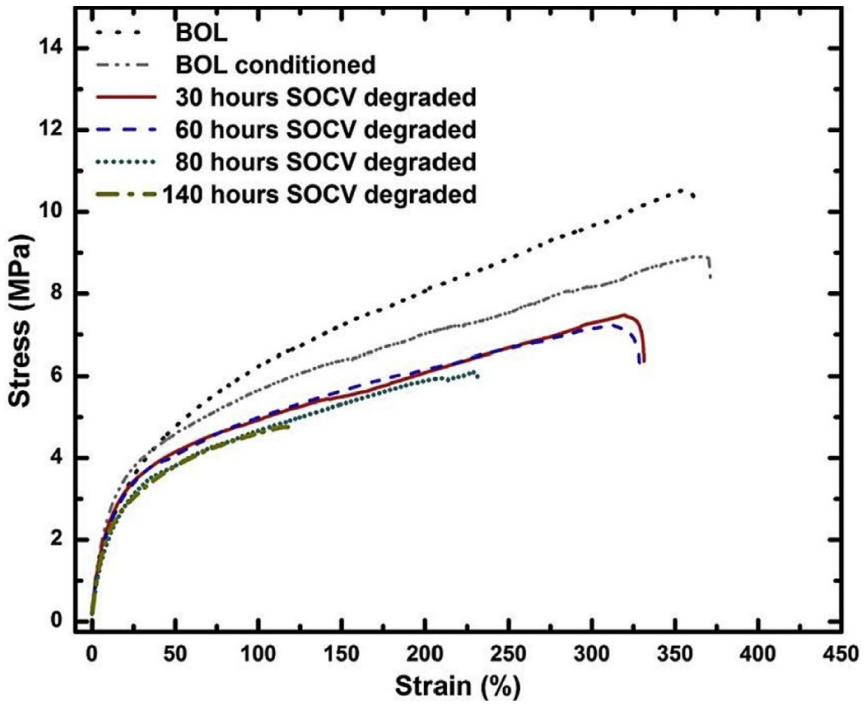

Figure 65 **Stress-strain curves of the SOCV accelerated stress test in the degraded CCMs obtained at 70 °C 90% RH, Reprinted from [133] with permission from Elsevier**

This difference between these two methods for updating the CAPDE (one predicts around a 40% reduction and the second predicts a 75% reduction in CAPDE) to consider chemical degradation impacts shows that more experiments need to be designed and implemented to measure this reduction. SOCV is a harsher chemical degradation process compared to the Fenton and COCV tests. It is likely that after approximately 140 hours of OCV operation, a huge reduction in CAPDE would be expected. The Fenton test is easier to conduct, but it is performed ex-situ. In contrast, the SOCV test is more similar to the start-up and shut-down phases of a fuel cell. However, it may not fully represent the conditions of a fuel cell in real operational conditions. It appears that OCV+RH closely mirrors real fuel cell operating conditions.

6 Conclusions

The fatigue behavior of membranes in PEFC due to hygrothermal cycles is a critical factor that affects fuel cell durability and lifetime. To have a comprehensive study on the mechanical fatigue of the reinforced membrane, both ex-situ and in-situ conditions have been considered. For ex-situ testing, we have tensile tests in four critical ambient conditions. Based on these experiments, the optimized material parameters for the developed G'Sell-Jonas model were extracted, and its FEM model was built. In contrast to complex viscoelastic-plastic models that only consider temperature effects on material strength and humidity effects just on swelling, the developed G'Sell-Jonas theory factors in both temperature and humidity impacts on material strength itself apart from their contraction and expansion effects. Additionally, through a constitutive approach, the model includes the effects of volume changes due to temperature, humidity and strain rate impacts that shows itself in wet and dry phases durations.

Another ex-situ test is the fatigue test by DMA, whose results verified that membranes at lower temperatures (25 °C) and humidity are stronger. It also showed that at lower strain rates, the membrane fatigue lifetime increases while, based on previous studies for in-situ conditions in literature review, it should decrease. Therefore, DMA ex-situ tests are acceptable for comparing the fatigue lifetime of different membranes, but it is not possible to project their results to a membrane in complete fuel cell conditions and predict its mechanical fatigue lifetime. It is a significant point that because ex-situ fatigue tests in DMA are so much faster and cheaper, most studies and companies just use this type of fatigue test to assess their reinforced membrane, while their results are not extendable to the membrane's behavior in real fuel cell conditions. For in-situ studies, the current AMST protocols are time-consuming and costly, especially for reinforced membranes; however, by adding a pressure difference between the anode and cathode sides in AMST tests, ΔP-AMST, significant residual stresses are created, leading to membrane fatigue in less than 5000 dry-wet cycles. Therefore, developing a constitutive FEM model that covers critical factors like humidity, temperature, and strain rate to simulate this ΔP-AMST can help better understand this novel accelerated fatigue test and extend it for complete fuel cell modeling. The developed G'Sell-Jonas model was used to extract a S-N curve to evaluate fatigue responses in ΔP-AMST. The ΔP-AMST tests used in this study are four times faster than those used in previous studies, and the developed

model accounts for the effects of dry-wet cycle frequency in ΔP-AMST tests via the strain rate term. One observed phenomenon in this study was the type of fatigue failure at low ΔP in which cracks were initiated from several points near the center of the membrane, while at higher ΔP, just one hole was created due to crack propagation and final rupture. This observation can be extended to real fuel cell conditions where crack initiation can occur simultaneously in various places near the highest stress concentration area due to low ΔP between the anode and cathode sides.

This research suggests an innovative approach for determining the fatigue lifetime of a membrane in a complete fuel cell condition by projecting the lifetime from ΔP-AMST. To achieve this, the mechanical characteristics of the reinforced membrane are extracted by conducting tensile tests under different environmental conditions and strain rates, and then a constitutive model (the generalized G'Sell-Jonas model) is created that can also consider compressive stresses due to clamping, fuel, and air pressure in a complete fuel cell condition. The model is then applied to ΔP-AMST, and critical thresholds for fatigue failure are determined, that is, CAPDE. Meanwhile, a FEM model of the membrane in a fuel cell is constructed based on the constitutive model, and plastic dissipation for each temperature in a single RH cycle is computed. Using this concept that cracks are initiated when the accumulated plastic energy reaches the critical threshold, the number of cycles needed for the membrane to reach this point is determined by dividing the CAPDE in ΔP-AMST by the plastic dissipation energy in one RH cycle in the complete fuel cell model. For determining in which ΔP in the ΔP-AMST model, the CAPDE should be calculated, the modified amplitude stress in the center of the membrane under the channel in the complete fuel cell model is extracted, and by interpolation or extrapolation, the equivalent ΔP that can generate this modified amplitude stress in the ΔP-AMST model is obtained and put in the ΔP-AMST FEM model and its CAPDE is calculated. The results from this projection algorithm have been validated through comparison with similar work on reinforced membranes. Considering the uncertainties in both experiments and modeling, our estimations may have a maximum deviation of 10%. This novel approach is much faster than the DOE protocol and can predict the fatigue lifetime of any reinforced membrane. In the presented approach, by entering any boundary conditions (temperature, RH cycle) and changing the properties of other components like CL, GDL, and the length ratio of channel to land, the mechanical fatigue lifetime of the membrane is predictable. As an additional work, two approaches to integrating the chemical degradation effects into

this mechanical fatigue model in order to have a more comprehensive model for the membrane's fatigue lifetime were presented, both of which try to consider the impacts of chemical degradation on CAPDE because, due to chemical degradation during fuel cell operation, the identity of the membrane gradually changes, and so its CAPDE as the main criterion for crack initiation is reduced that for COCV and SOSC are around 40% and 75% respectively.

By using the developed roadmap for fatigue lifetime evaluation, just by having some tensile tests and ΔP-AMST, for any reinforced membrane in any fuel cell operational conditions and design, the membrane's fatigue lifetime in its in-situ conditions is predictable in a very short time This comprehensive membrane' fatigue model gives the following hints in order to assess the fatigue lifetime of reinforced membranes:

1. The reinforced membrane is more vulnerable to fatigue failures at higher temperatures.

2. Reducing both the duration and the level of dry phases in RH cycles are effective in extending the fatigue lifetime of the membrane. This is because the membrane spends less time under tensile stress conditions, resulting in a decrease in the dissipated plastic energy during each cycle. Therefore, this model recommends maintaining the membrane in wet phases for as long as possible by controlling the RH of the inputs to the fuel cell.

3. The reinforced membrane with a high swelling ratio through-plane and a low swelling ratio in-plane is more durable against mechanical fatigue failures. The reason is that stress in-plane, which is the source of crack initiation, decreases, resulting in less plastic energy dissipated in each cycle.

4. By increasing Young's modulus of GDL and CL, the membrane's fatigue lifetime doesn't change because the in-plane stress that is the source of crack initiation in the membrane originates from the membrane's swelling strain in-plane. GDL and CL primarily serve to prevent other defects, such as buckling in the membrane, and reduce the effects of bending due to the fuel and air pressure differential.

5. By decreasing the channel-to-land-width ratio membrane's fatigue lifetime increase, However, this reduction also decreases the fuel cell's active area under the channel, leading to decreased efficiency.

6. Using clamping mechanisms that can keep pressure constant instead of constant displacement of anode or cathode plates to apply compressive stress would be better for membranes' fatigue lifetime. In a constant pressure mechanism, some of the membrane swelling

through the plane is compensated for by the displacement of plates, resulting in less tensile stress being applied to the membrane in-plane.

7. Based on the effects of chemical degradation on the membrane, which include thinning and reducing CAPDE, cell potential is the dominant factor in chemical degradation. Therefore, operating the fuel cell at lower voltage levels or implementing gradual start-up and shut-down procedures can significantly reduce chemical degradation. As a result, the dominant form of degradation would be primarily mechanical.

8. Based on the logic behind the presented approach in this research for projecting fatigue lifetime from ΔP-AMST to a full fuel cell condition, this method is extendable to any membrane. However, the repetition of tensile tests, ΔP-AMST, and material optimization for FEM is necessary. For increased certainty, it is recommended to repeat this approach with several membranes in future studies.

7 Future works

When considering membrane fatigue lifetime in fuel cells, it is important to take into account various parameters, including contaminations and the effects of the edge of the GDL and gasket. While the primary factor affecting membrane lifetime is mechanical stress, other factors can also contribute to fatigue and degradation.

Contaminations: Contaminants can have detrimental effects on membrane performance and lifetime. For instance, impurities in the fuel or oxidant streams can cause chemical degradation or blockage of the electrode sites, leading to reduced performance and accelerated membrane degradation. Contaminants such as carbon monoxide (CO), iron, or sulfur compounds are particularly known for their adverse effects on the catalyst and membrane. Their places can be a trigger for crack initiations in the membrane.

Effects of GDL: The gas diffusion layer is positioned between the CL and the bipolar plate in a fuel cell. The GDL serves to transport reactant gases and provide electrical conductivity. Issues at the GDL edge, such as delamination or damage, can affect the flow distribution of reactants and lead to localized stress concentrations. These stress concentrations may result in membrane deformation or cracking, contributing to fatigue failure.

Effects of gasket: Gaskets are used to seal the fuel cell stack and ensure proper gas and fluid management. Poor gasket design, material selection, or degradation over time can lead to uneven compression and sealing pressure, causing non-uniform stress distribution on the membrane. Additionally, gasket degradation may result in leaks or increased contact resistance, leading to localized heating and potential membrane damage.

Another potential work for future studies is to implement a range of tests to evaluate the effects of chemical degradation on CAPDE in in-situ conditions instead of ex-situ approaches like the Fenton test and harsh in-situ methods like OCV tests.

Another recommendation for future research is to replicate all the procedures used in this study using CCM rather than membranes because putting the CL on a membrane can change its properties and affect how long it can last before it becomes fatigued.

A further suggestion for future research is to examine how sub-zero temperatures affect the membrane's mechanical fatigue behavior because water molecule expansion brought on by sub-zero temperatures can result in microcracks that shorten the membrane's fatigue lifetime.

Another recommendation for subsequent studies is to take into account the RH, voltage, and current cycles that the vehicle's acceleration and deceleration will impose on the membrane and how its fatigue lifetime will change.

References

1. Shirley C , Gecan R , and K. J, *Emissions of Carbon Dioxide in the Transportation Sector*. December 2022, https://www.cbo.gov/publication/58566.

2. Lenz, H.P., *32nd international vienna motor symposium.* MTZ worldwide eMagazine, 2011. **72**(9): p. 64-78.

3. Eberle, U., B. Müller, and R. Von Helmolt, *Fuel cell electric vehicles and hydrogen infrastructure: status 2012.* Energy & Environmental Science, 2012. **5**(10): p. 8780-8798.

4. Camacho, M.d.l.N., D. Jurburg, and M. Tanco, *Hydrogen fuel cell heavy-duty trucks: Review of main research topics.* International Journal of Hydrogen Energy, 2022. **47**(68): p. 29505-29525.

5. TEAM, Y. *The difference between gray, blue, and green hydrogen*. 2022; Available from: https://yaleclimateconnections.org/2022/02/the-difference-between-gray-blue-and-green-hydrogen/.

6. *The Future of Hydrogen*. 2019; Available from: https://www.iea.org/reports/the-future-of-hydrogen.

7. Park, S., K. Maeng, and J. Shin, *Efficient subsidy distribution for hydrogen fuel cell vehicles based on demand segmentation.* Technological Forecasting and Social Change, 2023. **186**: p. 122113.

8. Trencher, G., A. Taeihagh, and M. Yarime, *Overcoming barriers to developing and diffusing fuel-cell vehicles: Governance strategies and experiences in Japan.* Energy Policy, 2020. **142**: p. 111533.

9. Mench, M.M., *Fuel cell engines*. 2008: John Wiley & Sons.

10. Elgowainy, A., *Electric, Hybrid, and Fuel Cell Vehicles*. 2021: Springer.

11. Thomas, C.E.S., *Fuel Cell and Battery Electric Vehicles Compared*. 2008.

12. Kaur, G., *PEM fuel cells: fundamentals, advanced technologies, and practical application*. 2021: Elsevier.

13. Ade, N., et al., *Intensifying vehicular proton exchange membrane fuel cells for safer and durable, design and operation.* International Journal of Hydrogen Energy, 2020. **45**(7): p. 5039-5054.

14. Borup, R., et al., *Scientific aspects of polymer electrolyte fuel cell durability and degradation.* Chemical reviews, 2007. **107**(10): p. 3904-3951.

15. Adams, J. *DOE H2 Heavy Duty Truck Targets*. 2020; Available from: https://www.energy.gov/sites/prod/files/2020/02/f71/fcto-compressed-gas-storage-workshop-2020-adams.pdf.

16. DOE, *Multi-Year Research, Development, and demonstration plan, Fuel Cells Section 49.* 2016.

17. Garzon, F., et al., *Micro and nano X-ray tomography of PEM fuel cell membranes after transient operation.* ECS Transactions, 2007. **11**(1): p. 1139.

18. de Bruijn, F.A., V. Dam, and G. Janssen, *Durability and degradation issues of PEM fuel cell components.* Fuel cells, 2008. **8**(1): p. 3-22.

19. Collier, A., et al., *Degradation of polymer electrolyte membranes.* International Journal of Hydrogen Energy, 2006. **31**(13): p. 1838-1854.

20. Thampan, T., et al., *Modeling of conductive transport in proton-exchange membranes for fuel cells.* Journal of the Electrochemical Society, 2000. **147**(9): p. 3242.

21. Coms, F.D., *The chemistry of fuel cell membrane chemical degradation.* Ecs Transactions, 2008. **16**(2): p. 235.

22. Smitha, B., *Sridhar S and Khan AA.* J. Membr. Sci., 2005. **2005**: p. 259.

23. Le Canut, J.-M., R.M. Abouatallah, and D.A. Harrington, *Detection of membrane drying, fuel cell flooding, and anode catalyst poisoning on PEMFC stacks by electrochemical impedance spectroscopy.* Journal of The Electrochemical Society, 2006. **153**(5): p. A857.

24. Peighambardoust, S.J., S. Rowshanzamir, and M. Amjadi, *Review of the proton exchange membranes for fuel cell applications.* International journal of hydrogen energy, 2010. **35**(17): p. 9349-9384.

25. Weber, A.Z. and J. Newman, *Transport in polymer-electrolyte membranes: I. Physical model.* Journal of the Electrochemical Society, 2003. **150**(7): p. A1008.

26. Ueki, T. and M. Watanabe, *Macromolecules in ionic liquids: progress, challenges, and opportunities.* Macromolecules, 2008. **41**(11): p. 3739-3749.

27. Mukundan, R., et al., *Membrane accelerated stress test development for polymer electrolyte fuel cell durability validated using field and drive cycle testing.* Journal of The Electrochemical Society, 2018. **165**(6): p. F3085.

28. Alavijeh, A.S., et al., *Microstructural and mechanical characterization of catalyst coated membranes subjected to in situ hygrothermal fatigue.* Journal of The Electrochemical Society, 2015. **162**(14): p. F1461-F1469.

29. Tavassoli, A., et al., *Effect of catalyst layer defects on local membrane degradation in polymer electrolyte fuel cells.* Journal of Power Sources, 2016. **322**: p. 17-25.

30. Gittleman, C.S., F.D. Coms, and Y.-H. Lai, *Membrane durability: physical and chemical degradation.* Polymer electrolyte fuel cell degradation, 2011. **15**.

31. Rodgers, M.P., et al., *Fuel cell perfluorinated sulfonic acid membrane degradation correlating accelerated stress testing and lifetime.* Chemical reviews, 2012. **112**(11): p. 6075-6103.

32. Ghassemzadeh, L. and S. Holdcroft, *Quantifying the structural changes of perfluorosulfonated acid ionomer upon reaction with hydroxyl radicals.* Journal of the American Chemical Society, 2013. **135**(22): p. 8181-8184.

33. Lim, C., et al., *Membrane degradation during combined chemical and mechanical accelerated stress testing of polymer electrolyte fuel cells.* Journal of Power Sources, 2014. **257**: p. 102-110.

34. Sadeghi Alavijeh, A., et al., *Decay in mechanical properties of catalyst coated membranes subjected to combined chemical and mechanical membrane degradation.* Fuel cells, 2015. **15**(1): p. 204-213.

35. Ghassemzadeh, L., et al., *Selective formation of hydrogen and hydroxyl radicals by electron beam irradiation and their reactivity with perfluorosulfonated acid ionomer.* Journal of the American Chemical Society, 2013. **135**(42): p. 15923-15932.

36. Danilczuk, M., F.D. Coms, and S. Schlick, *Visualizing chemical reactions and crossover processes in a fuel cell inserted in the ESR resonator: detection by spin trapping of oxygen radicals, nafion-derived fragments, and hydrogen and deuterium atoms.* The Journal of Physical Chemistry B, 2009. **113**(23): p. 8031-8042.

37. Stewart, S.M., et al., *Cerium migration through hydrogen fuel cells during accelerated stress testing.* ECS Electrochemistry Letters, 2014. **3**(4): p. F19.

38. Baker, A.M., et al., *Cerium migration during PEM fuel cell accelerated stress testing.* Journal of The Electrochemical Society, 2016. **163**(9): p. F1023.

39. Gubler, L., et al., *Performance and durability of membrane electrode assemblies based on radiation‐grafted FEP‐g‐polystyrene membranes.* Fuel Cells, 2004. **4**(3): p. 196-207.

40. Endoh, E., *Progress of highly durable mea for PEMFC under high temperature and low humidity conditions.* ECS Transactions, 2008. **12**(1): p. 41.

41. Lim, C., et al., *Fuel cell durability enhancement with cerium oxide under combined chemical and mechanical membrane degradation.* ECS Electrochemistry Letters, 2015. **4**(4): p. F29.

42. Zhang, S., et al., *Effects of open-circuit operation on membrane and catalyst layer degradation in proton exchange membrane fuel cells.* Journal of Power Sources, 2010. **195**(4): p. 1142-1148.

43. Kundu, S., et al., *Reversible and irreversible degradation in fuel cells during open circuit voltage durability testing.* Journal of Power Sources, 2008. **182**(1): p. 254-258.

44. Yuan, X.-Z., et al., *A review of polymer electrolyte membrane fuel cell durability test protocols.* Journal of Power Sources, 2011. **196**(22): p. 9107-9116.

45. Zhang, S., et al., *A review of accelerated stress tests of MEA durability in PEM fuel cells.* International journal of hydrogen energy, 2009. **34**(1): p. 388-404.

46. Kusoglu, A. and A.Z. Weber, *New insights into perfluorinated sulfonic-acid ionomers.* Chemical reviews, 2017. **117**(3): p. 987-1104.

47. Pozio, A. and R. Silva, *M. De Francesco, L. Giorgi.* Electrochimica Acta, 2003. **48**: p. 1543.

48. Healy, J., et al., *Aspects of the chemical degradation of PFSA ionomers used in PEM fuel cells.* Fuel cells, 2005. **5**(2): p. 302-308.

49. Kinumoto, T., et al., *Durability of perfluorinated ionomer membrane against hydrogen peroxide.* Journal of power Sources, 2006. **158**(2): p. 1222-1228.

50. Tang, H., et al., *A degradation study of Nafion proton exchange membrane of PEM fuel cells.* Journal of Power Sources, 2007. **170**(1): p. 85-92.

51. Ramani, D., et al., *Evolution of Membrane Degradation in Fuel Cells Observed By X-Ray Computed Tomography.* ECS Meeting Abstracts, 2016. **MA2016-02**(38): p. 2841.

52. Kundu, S., et al., *Degradation analysis and modeling of reinforced catalyst coated membranes operated under OCV conditions.* Journal of Power Sources, 2008. **183**(2): p. 619-628.

53. Kundu, S., L.C. Simon, and M.W. Fowler, *Comparison of two accelerated Nafion™ degradation experiments.* Polymer Degradation and Stability, 2008. **93**(1): p. 214-224.

54. Young, A., et al., *Ionomer degradation in polymer electrolyte membrane fuel cells.* Journal of The Electrochemical Society, 2010. **157**(3): p. B425.

55. Venkatesan, S.V., *Investigation of mesoscopic degradation phenomena in fuel cells.* 2017.

56. Kreitmeier, S., et al., *Local degradation at membrane defects in polymer electrolyte fuel cells.* Journal of The Electrochemical Society, 2013. **160**(4): p. F456.

57. Macauley, N., et al., *Accelerated membrane durability testing of heavy duty fuel cells.* Journal of the Electrochemical Society, 2014. **162**(1): p. F98.

58. Goulet, M.-A., et al., *Mechanical properties of catalyst coated membranes for fuel cells.* Journal of power sources, 2013. **234**: p. 38-47.

59. Lai, Y.-H., et al., *Viscoelastic stress analysis of constrained proton exchange membranes under humidity cycling.* 2009.

60. Lai, Y.-H., et al. *Viscoelastic stress model and mechanical characterization of perfluorosulfonic acid (PFSA) polymer electrolyte membranes*. in *International Conference on Fuel Cell Science, Engineering and Technology*. 2005.

61. Kusoglu, A., et al., *Mechanical response of fuel cell membranes subjected to a hygro-thermal cycle.* Journal of power sources, 2006. **161**(2): p. 987-996.

62. Aindow, T. and J. O'Neill, *Use of mechanical tests to predict durability of polymer fuel cell membranes under humidity cycling.* Journal of Power Sources, 2011. **196**(8): p. 3851-3854.

63. Uchiyama, T., H. Kumei, and T. Yoshida, *Catalyst layer cracks by buckling deformation of membrane electrode assemblies under humidity cycles and mitigation methods.* Journal of power sources, 2013. **238**: p. 403-412.

64. Uchiyama, T., M. Kato, and T. Yoshida, *Buckling deformation of polymer electrolyte membrane and membrane electrode assembly under humidity cycles.* Journal of Power Sources, 2012. **206**: p. 37-46.

65. Uchiyama, T., et al., *Mechanical degradation mechanism of membrane electrode assemblies in buckling test under humidity cycles.* Journal of Fuel Cell Science and Technology, 2012. **9**(6).

66. Zhang, Z., et al., *Exploring the role of reinforcement in controlling fatigue crack propagation behavior of perfluorosulfonic-acid membranes.* International Journal of Hydrogen Energy, 2018. **43**(12): p. 6379-6389.

67. Wallnöfer-Ogris, E., et al., *Main degradation mechanisms of polymer electrolyte membrane fuel cell stacks–Mechanisms, influencing factors, consequences, and mitigation strategies.* International Journal of Hydrogen Energy, 2023.

68. Xing, Y., H. Li, and G. Avgouropoulos, *Research progress of proton exchange membrane failure and mitigation strategies.* Materials, 2021. **14**(10): p. 2591.

69. Thangavelautham, J., *Degradation in PEM fuel cells and mitigation strategies using system design and control.* Proton exchange membrane fuel cell, 2018.

70. Shi, S., A.Z. Weber, and A. Kusoglu, *Structure/property relationship of Nafion XL composite membranes.* Journal of Membrane Science, 2016. **516**: p. 123-134.

71. Pan, M., et al., *A review of membranes in proton exchange membrane fuel cells: Transport phenomena, performance and durability.* Renewable and Sustainable Energy Reviews, 2021. **141**: p. 110771.

72. *DuPont launches Nafion XL MEA.* Fuel Cells Bulletin, 2009. **2009**(7): p. 10.

73. Yu, L., et al., *Structure–property relationship study of Nafion XL membrane for high-rate, long-lifespan, and all-climate vanadium flow batteries.* RSC Advances, 2017. **7**(50): p. 31164-31172.

74. Burlatsky, S., et al., *A mathematical model for predicting the life of polymer electrolyte fuel cell membranes subjected to hydration cycling.* Journal of Power Sources, 2012. **215**: p. 135-144.

75. Hasan, M., et al., *Determining the critical plastically dissipated energy for fatigue crack growth in PEM fuel cell membrane and its environmental sensitivity.* International Journal of Fatigue, 2020: p. 105697.

76. Khorasany, R.M., et al., *Simulation of ionomer membrane fatigue under mechanical and hygrothermal loading conditions.* Journal of Power Sources, 2015. **279**: p. 55-63.

77. Mehrtash, M., I. Tari, and S. Yesilyurt, *Numerical modeling of visco-elasto-plastic hygro-thermal stresses and the effects of operating conditions on the mechanical degradation of PEFC membranes.* Journal of Power Sources, 2018. **396**: p. 164-174.

78. Silberstein, M.N. and M.C. Boyce, *Constitutive modeling of the rate, temperature, and hydration dependent deformation response of Nafion to monotonic and cyclic loading.* Journal of Power Sources, 2010. **195**(17): p. 5692-5706.

79. Khattra, N.S., et al., *Effect of time-dependent material properties on the mechanical behavior of PFSA membranes subjected to humidity cycling.* Journal of Power Sources, 2012. **214**: p. 365-376.

80. Kusoglu, A., et al., *Numerical investigation of mechanical durability in polymer electrolyte membrane fuel cells.* Journal of the Electrochemical Society, 2010. **157**(5): p. B705.

81. Singh, Y., et al., *Ex situ measurement and modelling of crack propagation in fuel cell membranes under mechanical fatigue loading.* International Journal of Hydrogen Energy, 2017. **42**(30): p. 19257-19271.

82. Ding, G., et al., *Numerical evaluation of crack growth in polymer electrolyte fuel cell membranes based on plastically dissipated energy.* Journal of Power Sources, 2016. **316**: p. 114-123.

83. Theiler, A. and L. Karpenko-Jereb, *Modelling of the mechanical durability of constrained Nafion membrane under humidity cycling.* international journal of hydrogen energy, 2015. **40**(31): p. 9773-9782.

84. Alavijeh, A.S., et al., *Effect of hygral swelling and shrinkage on mechanical durability of fuel cell membranes.* Journal of Power Sources, 2019. **427**: p. 207-214.

85. Kusoglu, A., M.H. Santare, and A.M. Karlsson, *Aspects of fatigue failure mechanisms in polymer fuel cell membranes.* Journal of Polymer Science Part B: Polymer Physics, 2011. **49**(21): p. 1506-1517.

86. Rodgers, M.P., et al., *Perfluorinated Sulfonic Acid Membrane and Membrane Electrode Assembly Degradation Correlating Accelerated Stress Testing and Lifetime Testing.* ECS Transactions, 2013. **58**(1): p. 129.

87. Ramani, D., et al., *4D in situ visualization of mechanical degradation evolution in reinforced fuel cell membranes.* International Journal of Hydrogen Energy, 2020.

88. Lai, Y.-H., et al., *Viscoelastic stress analysis of constrained proton exchange membranes under humidity cycling.* Journal of Fuel Cell Science and Technology, 2009. **6**(2).

89. Chen, J., et al., *Effects of cycle duration and test hardware in relative humidity cycling of a polymer electrolyte membrane.* Journal of Power Sources, 2020. **476**: p. 228576.

90. Rice, J.R., *The mechanics of crack tip deformation and extension by fatigue*. 1966: Division of Engineering, Brown University.

91. Klingbeil, N.W., *A total dissipated energy theory of fatigue crack growth in ductile solids.* International Journal of Fatigue, 2003. **25**(2): p. 117-128.

92. Daily, J.S. and N.W. Klingbeil, *Plastic dissipation in mixed-mode fatigue crack growth along plastically mismatched interfaces.* International Journal of Fatigue, 2006. **28**(12): p. 1725-1738.

93. Ding, G., A.M. Karlsson, and M.H. Santare, *Numerical evaluation of fatigue crack growth in polymers based on plastically dissipated energy.* International Journal of Fatigue, 2017. **94**: p. 89-96.

94. Izumi, Y. and M.E. Fine, *Role of plastic work in fatigue crack propagation in metals.* Engineering Fracture Mechanics, 1979. **11**(4): p. 791-804.

95. Fine, M.E. and D.L. Davidson, *Quantitative measurement of energy associated with a moving fatigue crack.* Fatigue mechanisms: Advances in quantitative measurement of physical damage, ASTM STP, 1983. **811**: p. 350-370.

96. Hasan, M., et al., *Predicting fatigue lifetimes of a reinforced membrane in polymer electrolyte membrane fuel cell using plastic energy.* Journal of Power Sources, 2022. **539**: p. 231597.

97. Sadeghi Alavijeh, A., et al., *A rapid mechanical durability test for reinforced fuel cell membranes.* Journal of Power Sources Advances, 2020. **2**: p. 100010.

98. Zatoń, M., J. Rozière, and D. Jones, *Current understanding of chemical degradation mechanisms of perfluorosulfonic acid membranes and their mitigation strategies: a review.* Sustainable Energy & Fuels, 2017. **1**(3): p. 409-438.

99. Singh, Y., et al., *Mitigation of mechanical membrane degradation in fuel cells by controlling electrode morphology: a 4D in situ structural characterization.* Journal of The Electrochemical Society, 2021. **168**(3): p. 034521.

100. Sun, X., et al., *Embrittlement induced fracture behavior and mechanisms of perfluorosulfonic-acid membranes after chemical degradation.* Journal of Power Sources, 2020. **453**: p. 227893.

101. Chen, Y., et al., *4D imaging of chemo-mechanical membrane degradation in polymer electrolyte fuel cells-Part 2: Unraveling the coupled degradation mechanisms within the active area.* Journal of Power Sources, 2022. **520**: p. 230673.

102. Lim, H.J., G. Kim, and G.J. Yun, *Durability and Performance Analysis of Polymer Electrolyte Membranes for Hydrogen Fuel Cells by a Coupled Chemo-mechanical Constitutive Model and Experimental Validation.* ACS Applied Materials & Interfaces, 2023.

103. Shah, N., B. Bhattacharya, and H. Kanchwala. *Development of a Novel Viscoelastic Nanocomposite and Investigation of Its Damping Capacity for Large Frequency Band*. in *Advances in Structural Vibration: Select Proceedings of ICOVP 2017*. 2021. Springer.

104. Bergstrom, J.S., *Mechanics of solid polymers: theory and computational modeling*. 2015: William Andrew.

105. Spoerl, E., *Stress-strain measurements by strip extensiometry* 2012.

106. Wang, L.-l., *CHAPTER 6 - One-Dimensional Visco-Elastic Waves and Elastic-Visco-Plastic Waves*, in *Foundations of Stress Waves*, L.-l. Wang, Editor. 2007, Elsevier: Oxford. p. 219-264.

107. El-Amin, M., *Viscoelastic and Viscoplastic Materials*. 2016: BoD–Books on Demand.

108. *Abaqus document help.* 2020.

109. Khattra, N.S., et al., *Time-dependent mechanical response of a composite PFSA membrane.* Journal of power sources, 2013. **228**: p. 256-269.

110. Yoon, W. and X. Huang, *A nonlinear viscoelastic–viscoplastic constitutive model for ionomer membranes in polymer electrolyte membrane fuel cells.* Journal of power sources, 2011. **196**(8): p. 3933-3941.

111. G'sell, C., et al. *Creep and Yield Behaviour of Semi-Crystalline Polyethylene in Uniaxial Tension*. in *IUTAM Symposium on Micromechanics of Plasticity and Damage of Multiphase Materials*. 1996. Dordrecht: Springer Netherlands.

112. Kusoglu, A., et al., *Stress-Strain Behavior of Perfluorosulfonic Acid Membranes at Various Temperatures and Humidities: Experiments and Phenomenological Modeling.* Journal of Fuel Cell Science and Technology, 2008. **6**(1).

113. Khattra, N.S., et al., *Residual fatigue life modeling of fuel cell membranes.* Journal of Power Sources, 2020. **477**: p. 228714.

114. G'sell, C. and J. Jonas, *Determination of the plastic behaviour of solid polymers at constant true strain rate.* Journal of materials science, 1979. **14**(3): p. 583-591.

115. Tang, Y., et al., *Mechanical properties of a reinforced composite polymer electrolyte membrane and its simulated performance in PEM fuel cells.* Journal of Power Sources, 2008. **175**(2): p. 817-825.

116. KWANG, S., *Viscoelasticity of Polymers: Theory and Numerical Algorithms*. 2018: Springer.

117. Beer, F. and R. Johnston, *Mechanics of Materials*. Eighth Edition ed. Vol. Stress and Strain—Axial Loading. 2020.

118. Khorasany, R.M., et al., *On the constitutive relations for catalyst coated membrane applied to in-situ fuel cell modeling.* Journal of Power Sources, 2014. **252**: p. 176-188.

119. Nicholas, T. and J.R. Zuiker, *On the use of the Goodman diagram for high cycle fatigue design.* International Journal of Fracture, 1996. **80**(2): p. 219-235.

120. SIEMENS. *Mean Stress Corrections and Stress Ratios*. 2019; Available from: https://community.sw.siemens.com/s/article/the-goodman-haigh-diagram-for-infinite-life.

121. Khorasany, R.M., et al., *Mechanical degradation of fuel cell membranes under fatigue fracture tests.* Journal of Power Sources, 2015. **274**: p. 1208-1216.

122. U.S. Department of Energy, D.C.C.A.S.T. 2010; Available from: https://www1.eere.energy.gov/hydrogenandfuelcells/fuelcells/pdfs/component_durability_profile.pdf.

123. Eikani, M.H., et al., *Design and Fabrication of a 300W PEM Fuel Cell Test Station.* Procedia Engineering, 2012. **42**: p. 368-375.

124. Richard Budynas, J.K.N., *Shigley's Mechanical Engineering Design*. 11 ed. Vol. Endurance Limit Modifying Factors. 2020.

125. Dillard, D.A., et al., *On the Use of Pressure-Loaded Blister Tests to Characterize the Strength and Durability of Proton Exchange Membranes.* Journal of Fuel Cell Science and Technology, 2009. **6**(3).

126. Benjamin, T.G. *Membrane and MEA Accelerated Stress Test Protocols*. 2007; Available from: https://www.energy.gov/sites/prod/files/2014/03/f12/htmwg_benjamin.pdf.

127. Liu, H., et al., *A multi-scale hybrid degradation index for proton exchange membrane fuel cells.* Journal of Power Sources, 2019. **437**: p. 226916.

128. Patil, Y.P., W.L. Jarrett, and K.A. Mauritz, *Deterioration of mechanical properties: a cause for fuel cell membrane failure.* Journal of Membrane Science, 2010. **356**(1-2): p. 7-13.

129. Liu, W. and M. Crum, *Effective testing matrix for studying membrane durability in PEM fuel cells: Part I. Chemical durability.* Ecs Transactions, 2006. **3**(1): p. 531.

130. Shi, S., et al., *Fatigue crack propagation behavior of fuel cell membranes after chemical degradation.* International Journal of Hydrogen Energy, 2020. **45**(51): p. 27653-27664.

131. Ramani, D., et al., *Characterization of membrane degradation growth in fuel cells using X-ray computed tomography.* Journal of The Electrochemical Society, 2018. **165**(6): p. F3200.

132. Garner, S., *Characterization of the Structure and Properties of Reinforced Ionomer Membranes and Effects on Durability in Polymer Electrolyte Membrane Fuel Cells*, in *Sustainable Energy Engineering*. 2022, Simon Fraser University.

133. Bhattacharya, S., et al., *Isolated chemical degradation induced decay of mechanical membrane properties in fuel cells.* Electrochimica Acta, 2020. **352**: p. 136489.

134. Coms, F.D., et al., *Mechanism of Perfluorsulfonic Acid Membrane Chemical Degradation Under Low RH Conditions.* ECS Transactions, 2013. **50**(2): p. 907.

Appendix A.

Repeated pressure-differential accelerated mechanical stress tests (ΔP-AMST)

The following figures are ΔP-AMST at 90 °C that repeated 3 times.

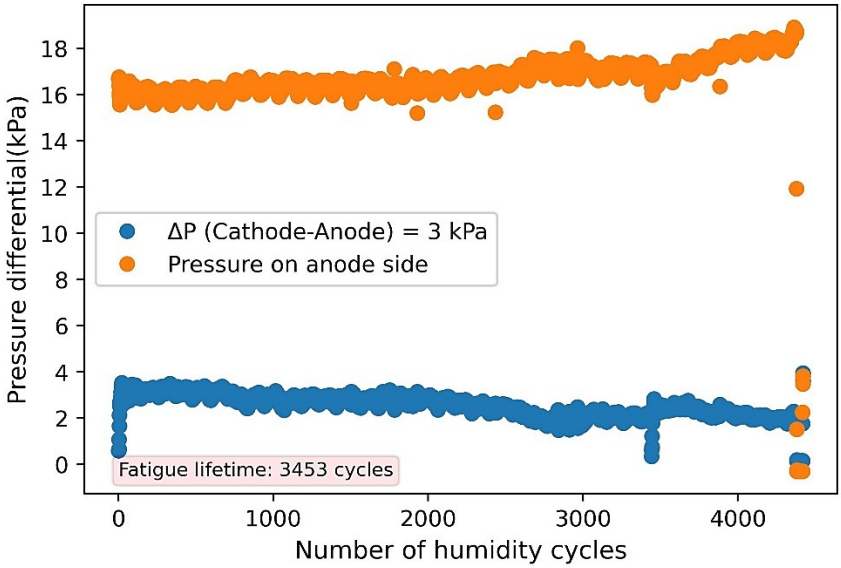

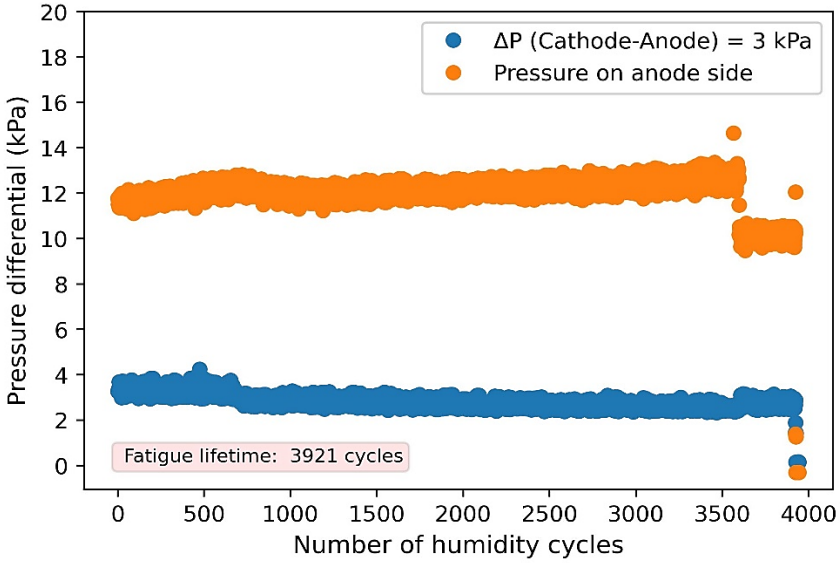

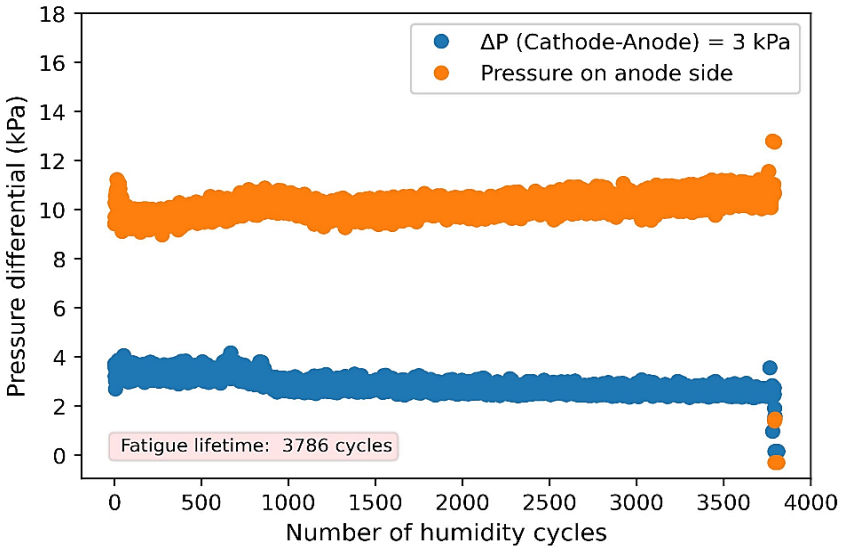

Figure A.1 3 tests of ΔP-AMST at 90 °C with ΔP = 3 kPa

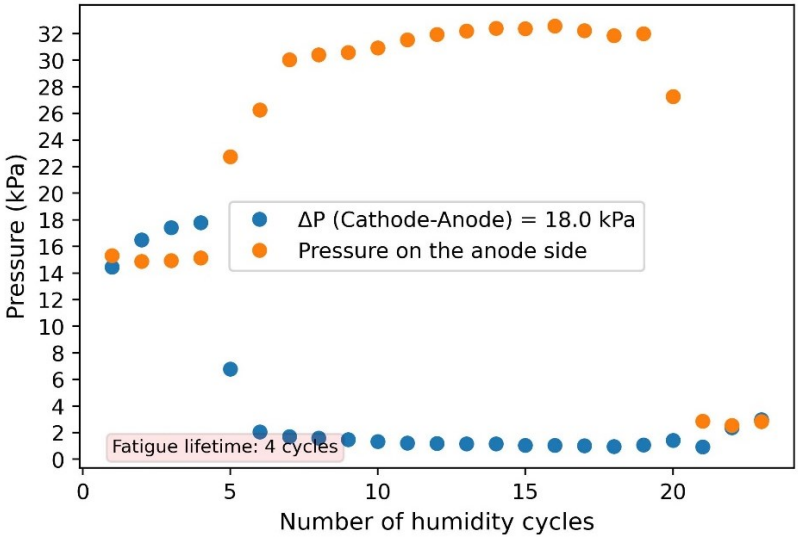

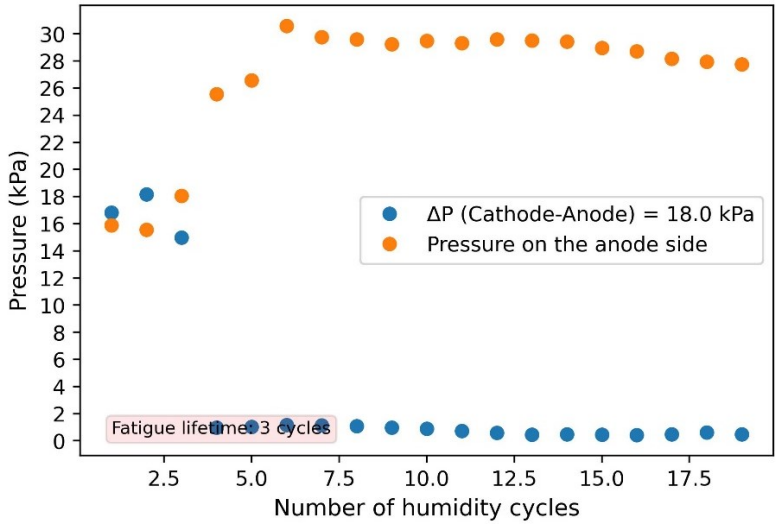

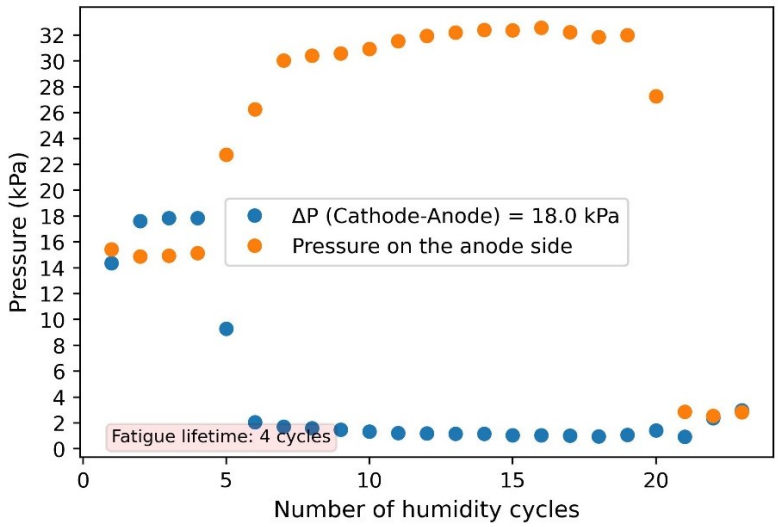

Figure A.2 3 tests of ΔP-AMST at 90 °C with ΔP = 18 kPa

The following figures are ΔP-AMST at 60 °C that repeated 3-4 times.

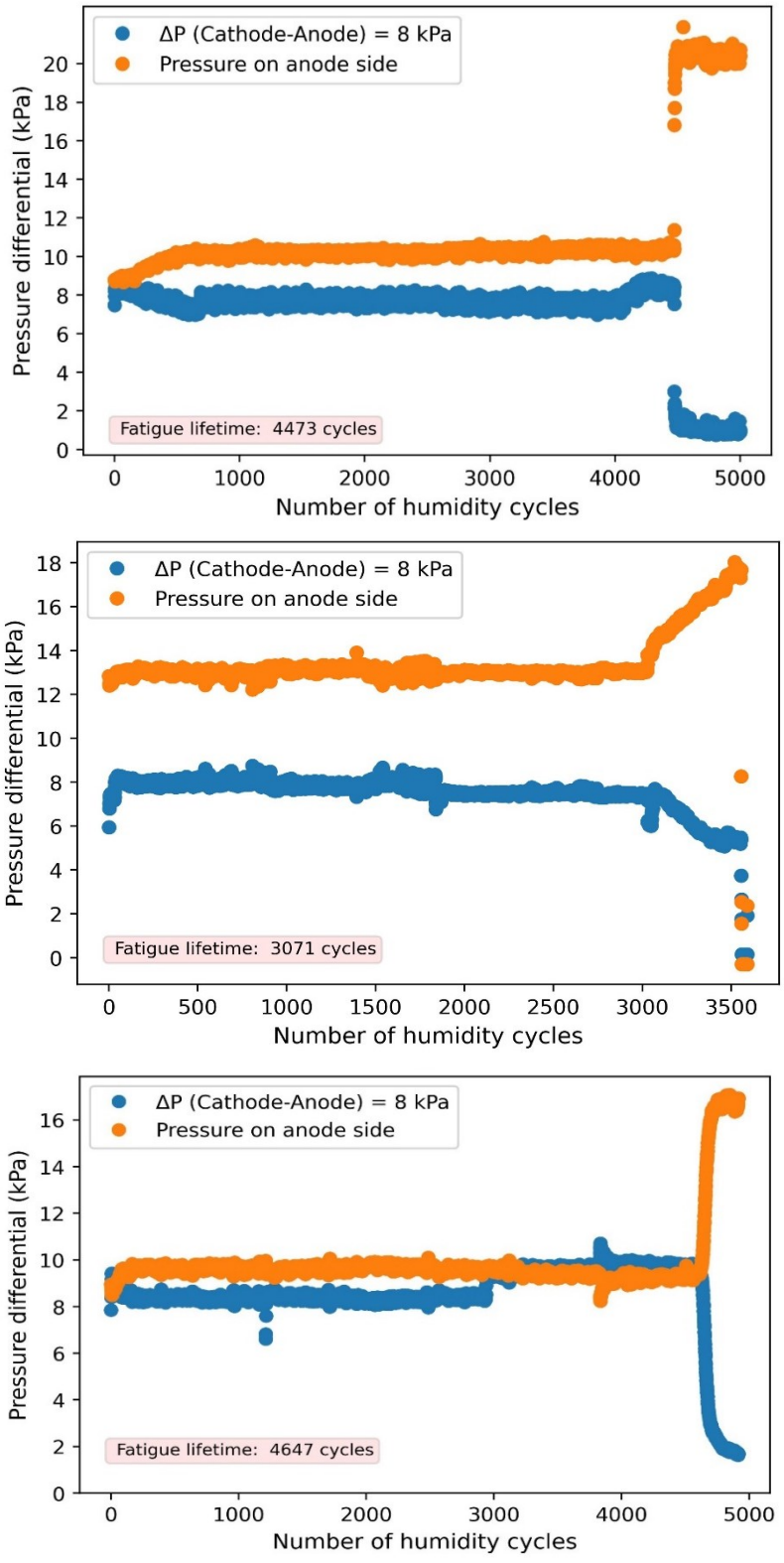

Figure A.3 3 tests of ΔP-AMST at 60 °C with ΔP = 8 kPa

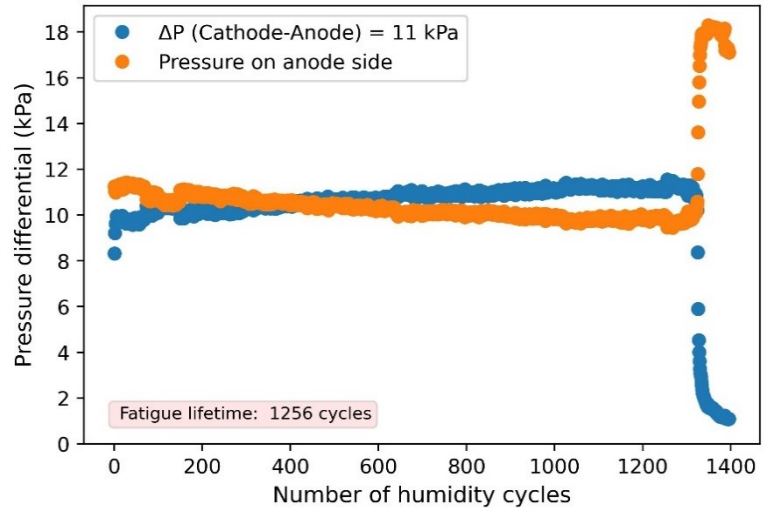
ΔP (Cathode-Anode) = 11 kPa
Pressure on anode side
Pressure differential (kPa)
Fatigue lifetime: 1256 cycles
Number of humidity cycles

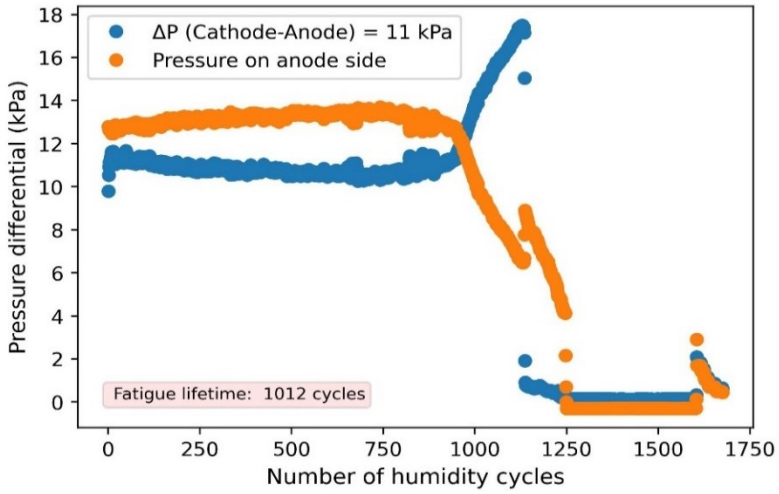
ΔP (Cathode-Anode) = 11 kPa
Pressure on anode side
Pressure differential (kPa)
Fatigue lifetime: 1012 cycles
Number of humidity cycles

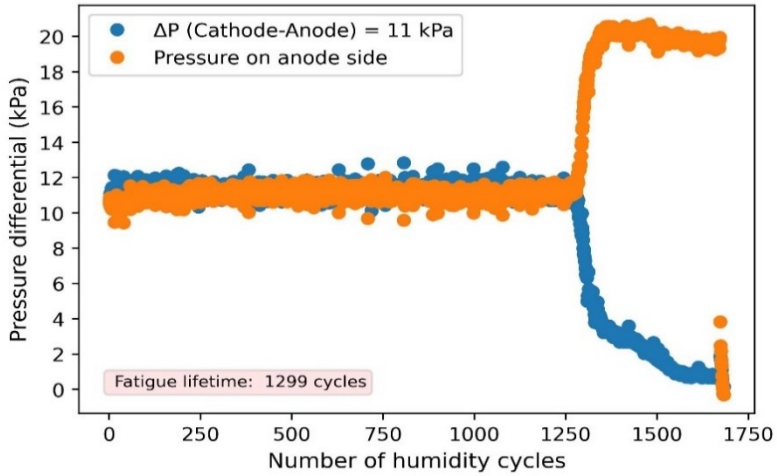
ΔP (Cathode-Anode) = 11 kPa
Pressure on anode side
Pressure differential (kPa)
Fatigue lifetime: 1299 cycles
Number of humidity cycles

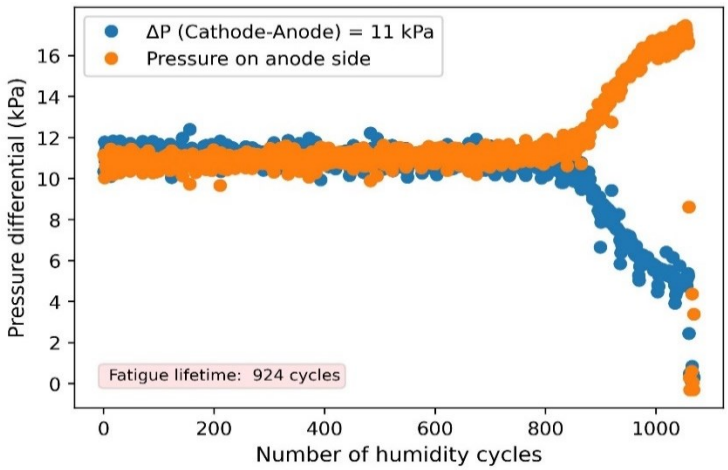

Figure A.4 3 tests of ΔP-AMST at 60 °C with ΔP = 11 kPa

Appendix B.

A list of written papers

- Mohsen Mazrouei Sebdani, Heather Baroody, and Erik Kjeang, “Modeling and Simulation of the Mechanical Properties of Reinforced Fuel Cell Membranes”, 241th Meeting of the Electrochemical Society, Vancouver, Canada, 2022

- Mohsen Mazrouei Sebdani, Erik Kjeang, “In-situ Pressure-Differential Accelerated Mechanical Fatigue Testing and Modeling of a Reinforced Fuel Cell Membrane”, Under review.

- Mohsen Mazrouei Sebdani, Heather Baroody, and Erik Kjeang, “Estimating the In-Situ Fatigue Lifetime of a Reinforced Membrane Using Pressure-Differential Accelerated Mechanical Stress Tests”, Under review.

- Mohammad Shojayian, Mohsen Mazrouei Sebdani, Erik Kjeang, “Simulation of Fuel Cell Membrane Durability under Vehicle Operation –A statistical model”, Under review

- Mohsen Mazrouei Sebdani, Heather Baroody, and Erik Kjeang, “In-Situ Fatigue Lifetime Modeling of a Reinforced Membrane by Projecting Critical Accumulated Plastic Dissipation Energy from Pressure-Differential Accelerated Mechanical Stress Tests”, 244th Meeting of the Electrochemical Society, Gothenburg, Sweden, 2023

- Mohammad Shojayian, Mohsen Mazrouei Sebdani, Erik Kjeang, “Simulation of Proton Exchange Membrane Durability under Fuel Cell Vehicle Operation – a Fundamental Study”, 244th Meeting of the Electrochemical Society, Gothenburg, Sweden, 2023